Co_2MnSi Heusler alloy thin films

Laura Jane Singh

Peterhouse

Cambridge

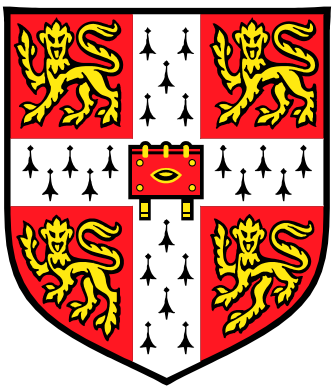

A dissertation submitted for the degree of Doctor of Philosophy at the University of Cambridge

March 2005

Abstract

This thesis investigates the growth of intermetallic compounds by co-sputtering from single elemental targets. The preliminary work involved constructing a sputtering set-up to grow a binary alloy (Sm-Co) and investigating how to control the composition spread that was obtained. Having achieved this, a larger sputtering flange was built up to grow the ternary Heusler alloy, Co_2MnSi.

Co_2MnSi has been predicted to be a half-metallic ferromagnet, which means that there is an energy gap in the minority spin band at the Fermi energy. This leads to 100 % spin polarised conduction electrons, which would enable ideal spin-device performance to be obtained. Co_2MnSi is particularly promising because it is predicted to have a large energy gap in the minority band of ~0.4 eV and has the highest Curie temperature among the known Heuslers of 985 K.

Initially, Co_2MnSi was grown on a-plane sapphire and stoichiometric films were single phase and highly (110) textured, without the use of a seed layer. They exhibited the bulk value of the saturation magnetisation, M_s and films grown at the highest deposition temperature (715 K) showed the lowest resistivity (47 μΩcm at 4.2 K) and the lowest room temperature coercivity (18 Oe). The spin polarisation of the transport current, P_t of a 400 nm film grown at this deposition temperature was 54 %, consistent with measurements on bulk single crystals. M_s decreased with decreasing film thickness indicating a graded disorder. By growing on GaAs (001), which has a similar lattice parameter to Co_2MnSi it was expected that this disordered region would be confined to the first few atomic layers. However, this was not the case because interfacial reactions resulted in the formation of an epitaxial Mn-As region, and a thin interfacial layer that was Co-Ga rich. This prevented the lattice matching of the Co_2MnSi to the GaAs(001) hence hindering epitaxial growth of the Heusler. The reaction zone also meant that films exhibited a M_s slightly below the bulk value. The expected fourfold anisotropy was not obtained for this cubic material, which is most likely due to the anisotropy of the reconstructed GaAs surface. In spite of this anomalous behaviour, P_t was 55 %, similar to the result obtained on sapphire, indicating that either P_t is independent of orientation or that the Heusler surface reconstructs in the same way. Films showed some improved properties to films grown on a-plane sapphire, indicating the potential of growing on this technologically important substrate. With this in mind, pseudo spin valves involving Co_2MnSi as one of the ferromagnetic electrodes were fabricated in both the CIP and CPP configurations. Clear low-field spin-valve contributions were observed at 15 K but the MR values are much lower than that expected from a PSV with a predicted 100 % spin polarised electrode.

Preface

This dissertation is the result of my own work and includes nothing which is the outcome of work done in collaboration except where specifically indicated in the text. No part of this dissertation has been or is being submitted for any other qualification at this or any other University. This dissertation does not exceed 60,000 words.

Some of the work in this dissertation has been published or submitted for publication as detailed below.

Publications

- Structural, magnetic and transport properties of thin films of the Heusler alloy Co_2MnSi.
  L. J. Singh, Z. H. Barber, Y. Miyoshi, Y. Bugoslavsky, W. R. Branford, and L. F. Cohen.
  Appl. Phys. Lett. **84**, 2367 (2004).

- Structural and transport studies of stoichiometric and off-stoichiometric thin films of the full Heusler alloy Co_2MnSi.
  L. J. Singh, Z. H. Barber, Y. Miyoshi, W. R. Branford, and L. F. Cohen.
  J. Appl. Phys. **95**, 7231 (2004).

- Interface effects of highly oriented films of the Heusler alloy Co_2MnSi on GaAs(001).
  L. J. Singh, Z. H. Barber, A. Kohn, A. K. Petford-Long, Y. Miyoshi, Y. Bugoslavsky and L. F. Cohen.
  Submitted to J. Appl. Phys. (2005).

- Magnetoresistance of spin valve structures based on the full Heusler alloy Co_2MnSi.
  L. J. Singh, C. W. Leung, C. Bell, J. L. Prieto and Z. H. Barber.
  Submitted to J. Appl. Phys. (2005).

Laura Singh
Device Materials Group, Department of Materials Science, University of Cambridge
March 2005.

"Surrounded by the right sounds, we all can be invigorated, energized, and balanced."

Dr. John Diamond.

Acknowledgements

Firstly, I would like to thank my supervisor Dr Zoe Barber for her support and guidance throughout my PhD. I am very grateful for the freedom I was given during the project and the constant encouragement when I felt it was all going wrong! I would also like to express my thanks to Prof Mark Blamire, Prof Jan Evetts and the entirety of the Device Materials Group, there are so many of you I could not possibly thank you all individually. Many thanks to our wonderful technical staff: Dr Nadia Stelmashenko for initially training me on the sputtering systems, Dave Nicols and David Vowles for their superb running of the SEM facilities, and Mary Vickers and Andrew Moss for their amazing wealth of knowledge concerning any aspect of XRD.

Many thanks to the sys-admin crew for preventing the whole lab from crashing and for managing to keep so much equipment alive and well! Special thanks to Chris 'Bello' Bell, 'mio Tio' José Prieto, Willemientje Eerenstein, Luis Hueso, Veni 'the eternal enthusiast' Madhav and Mr VSM himself Dennis Leung for all your help and advice. My office mates have provided me with much needed entertainment over the years: a million thanks to Debbie Morecroft for being such a good friend, Brian Pang for his interesting Buddha outlook on life and introducing me to cinnamon bagels, the elusive Ugi with the not so elusive surname, Simon the window opener and Shelly for trying to instil some sanity to the office…I know it was a never ending battle. I am 'filled with gratitude' to my desk partner, Alex 'Baron Mañana' Mischenko for going to APS during the last two weeks of writing, I managed to get sooooo much work done!! I am indebted to my writing up partner in crime, Sibe Mennema for helping me get through many painful late nights in the lab, I will never forget the musical interludes! Thanks to the lunch crew for keeping my meal times regular: Edgarino 'my grandfather once said…' Patino for his many theories, Diana 'chiquitina' Sánchez and Rainer Schmidt. Thanks to the parental figures of the lab, Vassilka Tsaneva and Rumen Tomov, what a lot of children you have.

Outside of the lab, I really value the kindness and amazing wisdom of the two Ros', Ade, Grace and Awak, you've always been inspirational friends. Last, but by no means least I thank my parents for their never ending love and support and my incredible cats, Aria, Octavia and Lucky!

I acknowledge the Engineering and Physical Sciences Research Council for three years of funding and am also very grateful for additional funding and travel money from the Cambridge Philosophical Society and Peterhouse, Cambridge.

For my parents

"Imagination is more important than knowledge."

Albert Einstein.

Contents

Symbols

$\boldsymbol{B}$	Magnetic induction
d	Target-substrate distance
E_a	Anisotropy energy
E_F	Fermi energy
E_m	Magnetostatic energy
$\boldsymbol{F}$	Force
G	Gibbs free energy
$\boldsymbol{H}$	Magnetic field strength
H_c	Coercivity
$\boldsymbol{H}_d$	Demagnetising field
$\boldsymbol{K}_u$	Uniaxial magnetocrytalline anisotropy
$\boldsymbol{m}$	Magnetic moment
$\boldsymbol{M}$	Magnetisation
M_r	Remanence
M_s	Saturation magnetisation
N_d	Demagnetising factor
p	Pole strength
P	Spin polarisation
R	Electrical resistance
S	Sputter yield
T_c	Curie temperature
T_{sub}	Substrate temperature
Z	Effective tunnel barrier height
β	Integral breadth
η	Mixing parameter
ρ	Electrical resistivity

Abbreviations

AFM	Atomic force microscope
AMR	Anisotropic magnetoresistance
CIP	Current in plane
CPP	Current perpendicular to plane
DC	Direct current
DOS	Density of states
DMS	Dilute magnetic semiconductor
EDS	Energy dispersive X-ray spectroscopy
FCC	Face centred cubic
FEG-SEM	Field emission gun scanning electron microscope
FFT	Fast Fourier transform
FIB	Focussed ion beam
FWHM	Full width at half maximum
GMR	Giant magnetoresistance
HMF	Half metallic ferromagnet
LED	Light emitting diode
MBE	Molecular beam epitaxy
MOKE	Magneto-optical Kerr effect
MR	Magnetoresistance
MTJ	Magnetic tunnel junction
OMR	Ordinary magnetoresistance
PSV	Pseudo spin valve
PVD	Physical vapour deposition
RE	Rare earth
RF	Radio frequency
RR	Resistivity ratio
SEM	Scanning electron microscope
TEM	Transmission electron microscope
TM	Transition metal
TMR	Tunnelling magnetoresistance
UHV	Ultra high vacuum

VSM	Vibrating sample magnetometer
XRD	X-ray diffraction

"...man will occasionally stumble over the truth, but usually manages to pick himself up, walk over or around it, and carry on."
Winston Churchill.

Chapter 1

Introduction

1.1 Magnetic thin films for recording media

The market for magnetic materials is huge and there are a large variety of applications, some of which are outlined in the following sections. Magnetic recording is by far the largest technological application of magnetism. In a recent review of magnetic recording[1] the magnetic recording industry in 2000 was said to exceed $50B. Magnetic thin films have been in general use as the medium of choice in hard-disk drives for about twenty years but continual demands for more data storage at lower prices means that research in this area is thriving, resulting in a fast-moving technology.

However, the areal density growth rate of magnetic hard disc drives has been slowing down recently from over 100 % per year to less than 40 % per year. This is because there is the problem of reaching the superparamagnetic limit. This occurs in the case of particles whose anisotropy energy is sufficiently below the thermal energy that energy fluctuations may spontaneously reverse the direction of magnetisation, even in the absence of an applied field. Current products use longitudinal recording with areal densities of around 70 Gbit/in^2 and the highest areal density demonstrations are only somewhat higher than 100 Gbit/in^2.

There are currently three possibilities that would push the superparamagnetic barrier to higher recording densities. The first involves developing materials with a higher anisotropy constant and a higher coercivity, H_c.[2] Prominent candidates are rare-earth transition metals, such as $SmCo_5$ (investigated in the first part of this thesis) and tetragonal intermetallic compounds such as the $L1_0$ phases FePt, which have 20-40 times higher uniaxial magnetocrystalline anisotropy, K_u than today's hexagonal Co-alloy based media. However, this places large demands on the write head material because it would need to have a larger saturation magnetisation, M_s in order to write on the higher coercivity medium. This could be solved by temperature-assisted write schemes, but a different recording technology would need to be implemented. The second possibility is patterned media.[3] This would involve the fabrication (by lithography) of an array of magnetic single domains equalling the bit size. Once again, this would force a major change in the fabrication of thin-film media. The final possibility is perpendicular recording,[4] and a lot of work has been carried out in this area.[5,6,7] A transition to perpendicular magnetic recording is expected somewhere above 100 Gbit/in^2 and perpendicular magnetic recording systems with areal densities as high as 1 Tbit/in^2 have been designed.[8] However, there is a disadvantage in the writability owing to the close alignment of the uniaxial anisotropy axis and the recording field. Tilted media[9] and composite perpendicular recording media[10] can be used to address this problem.

1.2 Spintronics

Recently a technology has emerged called spintronics, in which it is not the electron charge but the electron spin which carries the information. This opens the pathway for a new generation of devices combining standard microelectronics with spin-dependent effects that arise from the interaction between the carrier and the magnetic properties of the material. Adding the spin degree of freedom to conventional semiconductor charge-based electronics will offer many advantages: nonvolatility, increased data processing speed, decreased electric power consumption, and increased integration densities. However, this field is still in its infancy and it is not clear what kind of device configuration will eventually be viable. It is envisioned that the merging of electronics, photonics, and magnetics will ultimately lead to new spin-based multifunctional devices such as spin-FET (field effect transistor), spin-LED (light-emitting diode), spin RTD (resonant tunnelling device), encoders, decoders, and quantum bits for quantum computation and communication. It is debatable whether both the spin and charge degrees of freedom will be fully utilised, enabling qubit operation, as is required for quantum computing. A qubit (quantum bit) is the fundamental particle of spin-based computing and its quantum mechanical spin state carries the information. The qubit has to maintain a well-defined spin state long enough for a digital operation to be carried out.

One of the major technical barriers that needs to be overcome to realise the practical implementation of semiconductor-based spintronic devices is the development of suitable spin-polarised carriers to be injected, transported and manipulated in semiconductor heterostructures. The search for materials combining properties of the ferromagnet and the semiconductor has been challenging because of differences in crystal structure and chemical bonding.[11,12] Ferromagnetic semiconductors could provide the solution, enabling versatility in doping and fabrication of various structures and simple integration with the dominant semiconductor technology. The challenge will be finding a ferromagnetic semiconductor with a Curie temperature, T_c above room temperature. The discovery of T_c as high as 110 K in III-V-based dilute magnetic semiconductors (DMS) has attracted much attention.[13] Another approach is to search for new materials that exhibit large carrier spin polarisation (P). Candidates include ferromagnetic oxides and Heusler alloys, some of which are predicted to be half metallic ferromagnets (HMF).[14] This means that there is an energy gap in the minority spin band at the Fermi energy (E_F), resulting in 100 % spin polarised conduction electrons. It is the latter family of alloys, that forms the focus of this thesis.

1.3 Outline of thesis

This thesis investigates the growth of thin films of magnetic intermetallic compounds by dc magnetron co-sputtering from single elemental targets. Preliminary investigations begin on the binary intermetallic system, Sm-Co and the bulk of the thesis is on the more complicated ternary intermetallic, the Heusler alloy Co_2MnSi.

In chapter 2 a brief background is provided on the main areas addressed in this thesis: Sm-Co and Heusler alloys, sputtering, magnetic and transport properties.

Chapter 3 provides a description of the experimental procedures used to fabricate and characterise the thin films: dc magnetron sputtering, scanning electron microscopy (SEM), X-ray diffraction (XRD), vibrating sample magnetometry (VSM).

A review of the literature for the Sm-Co system is given in chapter 4, focussing on progress made in the growth and optimisation of $SmCo_5$.

Chapter 5 investigates the growth and magnetic properties of thin films of Sm-Co. A wide composition range is investigated by means of creating a composition spread by co-sputtering from two elemental targets onto an array of substrates.

A review of the literature for the family of ternary intermetallic alloys, Heusler alloys is provided in chapter 6.

Chapter 7 discusses the growth of highly oriented (110) thin films of the Heusler alloy Co_2MnSi on a-plane sapphire whereas chapter 8 investigates the growth of highly oriented (001) films of Co_2MnSi on the technologically important substrate GaAs(001).

Chapter 9 investigates the feasibility of using Co_2MnSi as an electrode in magnetic tunnel junctions (MTJ) and pseudo spin valves (PSV).

Finally, the conclusions are presented in chapter 10 and areas of further work are discussed.

References

[1] R. M. White, J. Magn. Magn. Mater. **226**, 2042 (2001).

[2] D. Weller, A. Moser, L. Folks, M. E. Best, W. Lee, M. F. Toney, M. Schwickert, J. U. Thiele, and M. F. Doerner, IEEE Trans. Magn. **36**, 10 (2000).

[3] R. L. White, R. M. H. New, and R. F. W. Pease, IEEE Trans. Magn. **33**, 990 (1997).

[4] H. N. Bertram and M. Williams, IEEE Trans. Magn. **36**, 4 (2000).

[5] S. Iwasaki, K. Ouchi, and N. Honda, IEEE Trans. Magn. **32**, 3795 (1996).

[6] M. Futamoto, Y. Hirayama, N. Inaba, Y. Honda, K. Ito, A. Kikugawa, and A. Takeuchi, IEEE Trans. Magn. **35**, 2802 (1999).

[7] K. Ouchi and N. Honda, IEEE Trans. Magn. **36**, 16 (2000).

[8] R. Wood, IEEE Trans. Magn. **36**, 36 (2000).

[9] J. P. Wang, Nat. Mater. **4**, 191 (2005).

[10] R. H. Victora and X. Shen, IEEE Trans. Magn. **41**, 537 (2005).

[11] M. Tanaka, J. Cryst. Growth **202**, 660 (1999).

[12] G. Prinz and K. Hathaway, Phys. Today **48**, 24 (1995).

[13] H. Ohno, A. Shen, F. Matsukura, A. Oiwa, A. Endo, S. Katsumoto, and Y. Iye, Appl. Phys. Lett. **69**, 363 (1996).

[14] R. A. de Groot, F. M. Mueller, P. G. Vanengen, and K. H. J. Buschow, Phys. Rev. Lett. **50**, 2024 (1983).

"The voyage of discovery is not in seeking new landscapes but in having new eyes."
Marcel Proust.

Chapter 2

Intermetallic magnetic thin films

In this chapter a brief background is given to the areas addressed in this thesis.

2.1 Intermetallic Compounds

This thesis deals with two families of intermetallic compounds: The rare-earth transition metal (RE-TM) family and the Heusler alloy family. These two families will be introduced in the following sections.

2.1.1 What is an intermetallic?

These are usually stoichiometric compounds (i.e. has a formula A_xB_y where x and y are integers) with a very narrow stability range. Small deviations in composition result in a rapid rise in the Gibbs free energy, *G* (Fig. 2.1a). In other structures these variations in composition can be tolerated by some atoms occupying 'wrong' positions or by atom sites being left vacant, and this would result in a free energy curve with a much smaller curvature (Fig. 2.1b).

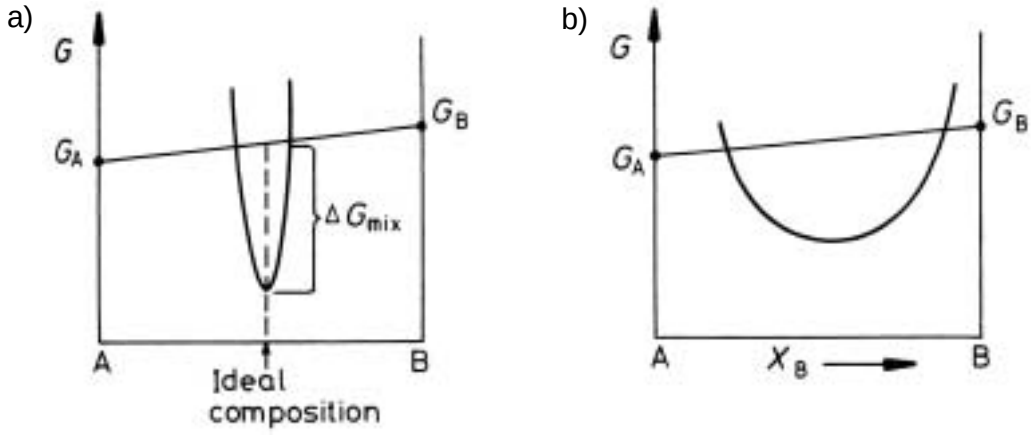

Fig. 2.1 Free energy curves for intermediate phases: a) for an intermetallic compound with a very narrow stability range, b) for an intermediate phase with a wide stability range.[1]

2.1.2 RE-TM Compounds

In the case of the RE-TM family, the rare earth elements have very different atomic radii from the transition elements and so there is very little solid solubility in RE-TM systems. Therefore, when one rare-earth is mixed with one transition metal, they tend to form a range of stoichiometric compounds, rather than solid solutions. In these binary systems the number of intermetallic compounds generally increases with increasing atomic number of the rare earth atom (decreasing radius of the rare earth atom). For a given rare earth, the number of compounds tends to increase with the number of 3d electrons of the alloying element. The rare-earth elements form a transition group which is similar to the transition metals. They have a stable core of 54 electrons and 2

electrons in the outermost 6s shell. The inner 4f shell has different numbers of electrons from element to element and these electrons determine the magnetic behaviour. In this work, the Sm-Co system is studied. There are seven intermetallic compounds, but the ones of interest are $SmCo_5$ and Sm_2Co_{17}, which are used to make permanent magnets. The magnetic moments of the light rare earth elements such as Sm couple ferromagnetically with Co. The crystal structure of $SmCo_5$ is shown in figure 2.2. It has the hexagonal space group, p6/mmm. This compound has a very high uniaxial magnetocrystalline anisotropy energy.

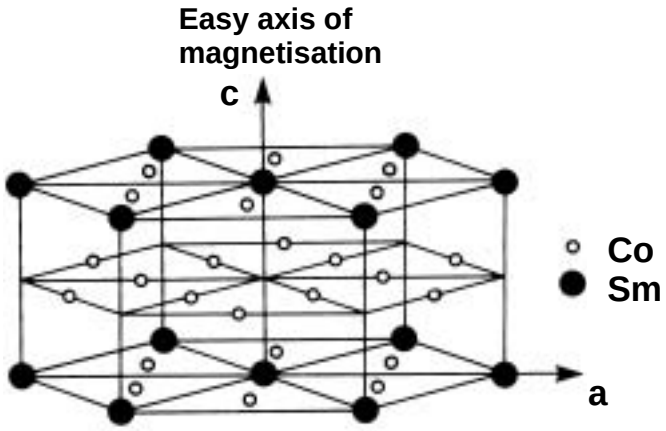

Fig. 2.2 Crystal structure of $SmCo_5$ (adapted from [2]).

2.1.3 Heusler Alloys

Another interesting family of intermetallic compounds is the Heusler alloys. These were first considered by Heusler[3] and his interest focused on the result that some of these alloys were strongly ferromagnetic but were made by combining elements which at the time were considered to be nonmagnetic. There are two families of Heusler alloys: the full Heusler alloys and the half Heusler alloys (Fig. 2.3). The first Heusler alloys studied were the full Heusler alloys, which have the form X_2YZ, where element X is typically a first-row transition or noble metal such as Co, Ni, Cu, Y is normally Mn and Z is usually a group-IIIB or –IVB element such as Al, In, Si, or Ge. They possess the $L2_1$ crystal structure which consists of four interpenetrating face-centred-cubic (fcc) sublattices: two occupied by atoms of element X, one occupied by Mn atoms, and one occupied by Z atoms. It was later discovered that it is possible to leave one of the four sublattices unoccupied, resulting in the half Heusler alloys, which have the form XYZ and have the $C1_b$ structure.

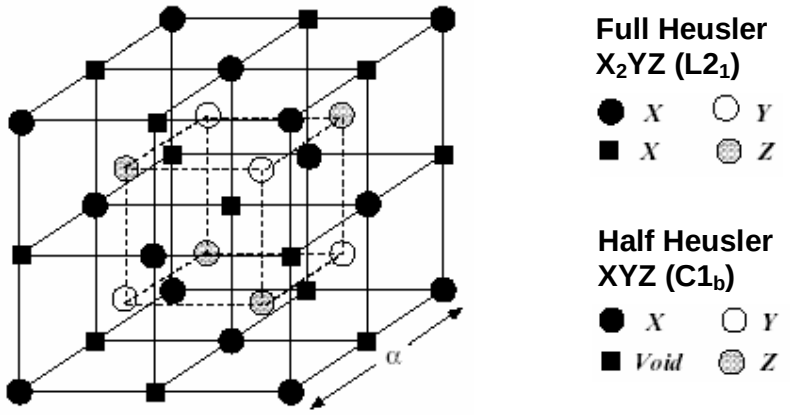

Fig. 2.3. $L2_1$ and $C1_b$ structure of the full and half Heusler alloys. The lattice consists of 4 interpenetrating fcc sublattices. The unit cell is an fcc lattice with 4 atoms as the basis: X1 (000), X2 (½½½), Y (¼¼¼) and Z (¾¾¾). In the case of the half Heusler alloy site X2 is vacant. If all the atoms were identical the lattice would simply be bcc (adapted from [4]).

Interest was renewed in these alloys in 1983 when de Groot *et al.*[5] showed by using first-principles electronic structure calculations that the half Heusler alloy NiMnSb is a half-metallic ferromagnet (HMF). This class of materials possess two spin bands that exhibit completely different behaviour (see schematic Fig. 2.4). The majority spin band (in this case the spin-up band) shows typical metallic behaviour whereas the minority band (in this case the spin-down band) shows semiconducting behaviour with a gap at E_F, leading to 100 % P at E_F. Therefore these HMFs can be considered as hybrids between metals and semiconductors.

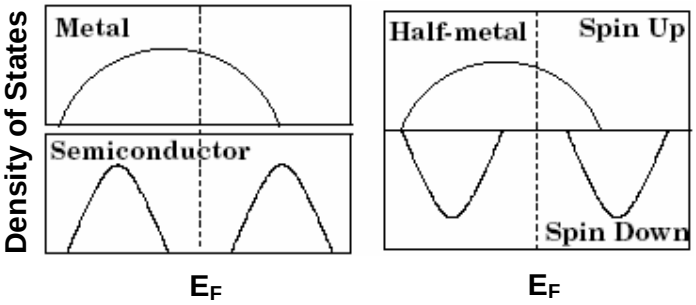

Fig. 2.4. Schematic representation of the density of states for a HMF with respect to normal metals and semiconductors (adapted from [4]).

One of the full Heusler alloys that has been predicted to be a HMF is Co_2MnSi,[6] which is the Heusler alloy investigated in this thesis. Figure 2.5 shows the energy dispersion curve for the minority band of Co_2MnSi and also the effect of adding Al, creating a series of non-stoichiometric compounds of the form $Co_2MnAl_{1-x}Si_x$. It is expected that by changing the number of electrons per formula unit, new HMFs can be found. E_F rises with increasing x and is located in the energy gap for a certain range of x. However, neutron diffraction studies carried out by Brown *et al.*[7]

found that there is a finite density of states (DOS) in the minority spin d band of Mn and so these compounds cannot be classified as HMF, but still have a high polarisation.

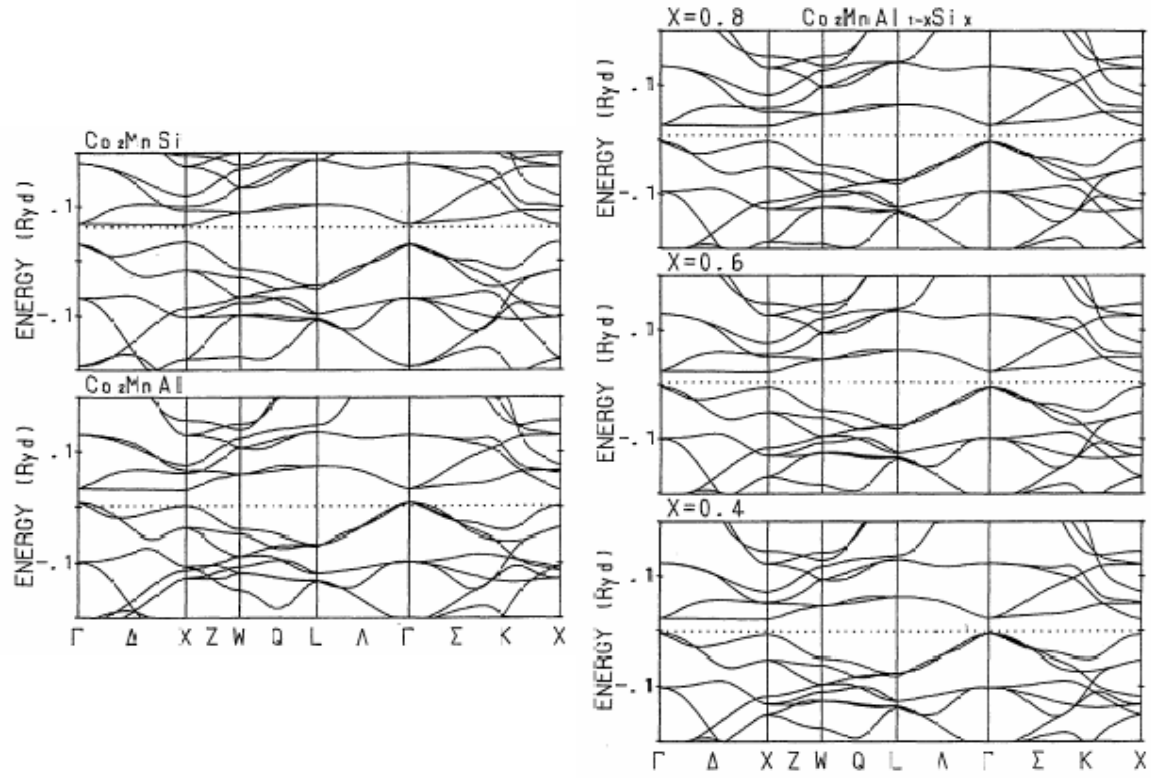

Fig. 2.5. Energy dispersion curves of the down-spin state near the Fermi level for Co_2MnZ (Z=Al, Si) and $Co_2MnAl_{1-x}Si_x$ for several compositions.[6]

The full Heusler alloy systems of the form Co_2MnZ have high values of the saturation magnetisation (M_s) and Curie temperature (T_c). The strong magnetism exhibited is mainly due to the local moments of well-separated Mn atoms. The total magnetic moment of Co_2MnZ is typically in the range 4-5 μ_B per formula unit and consists of 3 μ_B per Mn atom and less than 1 μ_B per Co atom.[8]

2.2 Sputter deposition

Sputter deposition, along with evaporation is categorised as Physical Vapour Deposition (PVD). PVD involves the generation of a vapour source and transport of the vapour species to a substrate. In the case of evaporation, the vapour source is produced by thermal means, whereas in sputtering atoms are removed from the source through impact of energetic ions.

Sputtering was first discovered in 1852 by Grove[9] and was developed as a thin-film deposition technique in the 1920's by Langmuir.[10] Since then it has become a widely used technique in both industry and research. It is a very versatile technique, since a range of materials can be deposited from either single element, composite, alloy or compound targets in many different geometries. The process can be easily automated or scaled up and the equipment cost is relatively low. Films used for magnetic and microelectronic applications often require stoichiometric alloys, which must conformally cover and adhere well to the substrates. These requirements have made sputtering (as well as chemical vapour deposition (CVD)) the technique of choice for most silicon-based technologies.

2.2.1 Mechanism of sputter deposition

A schematic diagram of a sputtering system is shown in figure 2.6. The target consists of a plate of the material to be deposited and is connected to the negative terminal of the power supply so it acts as the cathode. The substrates are generally earthed and act as the anode. Once the chamber is evacuated, a low-pressure sputtering gas (normally argon) is introduced which will initiate and sustain the discharge. A large enough voltage is applied between the cathode and anode so that the breakdown field of the gas is exceeded, creating a large number of ions and electrons.

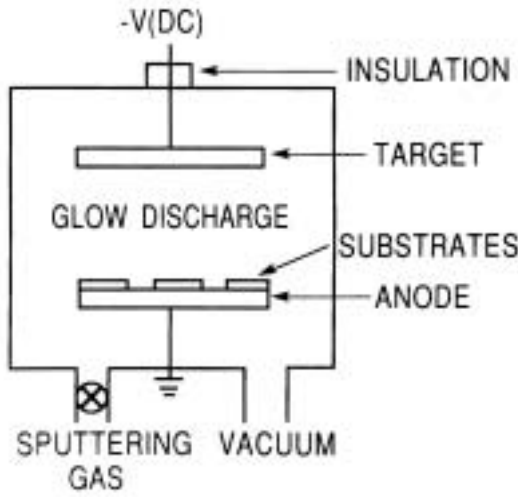

Fig. 2.6. Schematic diagram of a dc sputtering system.[11]

The positive ions in the discharge are accelerated towards the cathode and bombard the target (Fig. 2.7). This results in momentum transfer to surface atoms and a chain of collision events occurs, resulting in the ejection of target atoms, secondary electrons and reflected neutrals (neutralised argon ions). The sputtered flux is scattered by the sputtering gas and so species arrive at the

substrates at a range of angles, so good step coverage is achieved. The degree of scattering will depend on the pressure of the gas and so sputtering unlike evaporation is not a line of sight technique. The sputtered atoms escape with energies of typically 10 to 50 eV, which is about 100 times the energy of evaporated atoms. This results in energetic bombardment of the growing film and various processes can therefore occur. Resputtering of impurities or atomic species that have only been physically adsorbed is quite common and this is an effective cleaning process as the film grows. Forward sputtering can occur, where an atom collides with an atom on the film surface and knocks it into a different site, which enables more conformal coverage. The film can be compacted, implantation can occur (a problem if reflected neutrals are incorporated) and defects can form. One important effect is that energy is imparted to surface species, leading to enhanced mobility so that atoms can find their equilibrium positions before the next layer is deposited. The secondary electrons that are ejected from the target are accelerated away from the cathode and those that have sufficient energy will ionise neutral gas atoms, hence sustaining the plasma. This region is known as the "negative glow". In between this region and the cathode is the Crookes dark space where nearly all of the applied voltage is dropped.

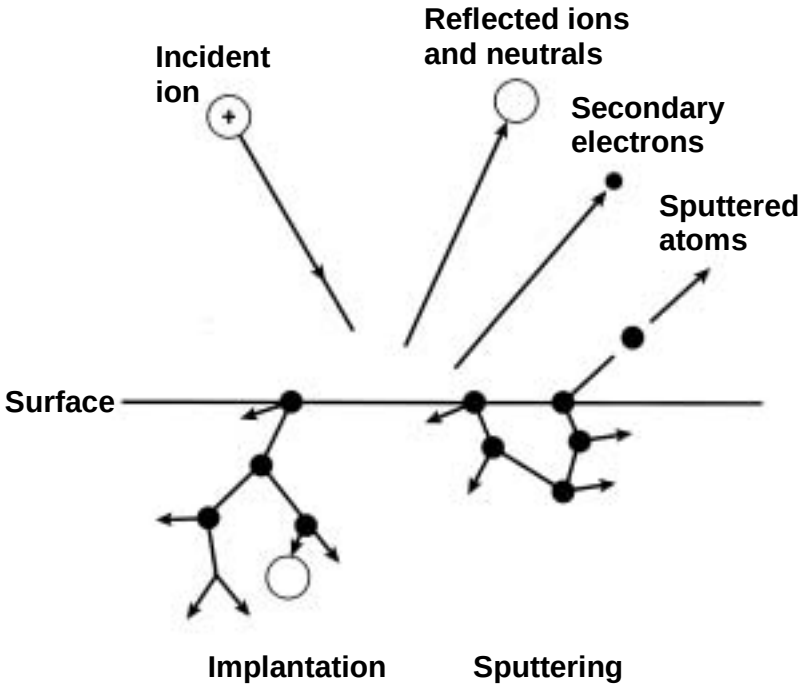

Fig. 2.7. Interaction of incident ion with the sputtering target (adapted from [12]).

The sputter yield, *S* is an important parameter in sputtering and is defined as the number of ejected particles per incident ion. It is a measure of the efficiency of sputtering and so for an incoming ion of incident energy, E_1<1keV,

$$S = \frac{3\alpha}{4\pi^2}\frac{E_t E_1}{U} \tag{2.1}$$

where E_t is the energy transfer function (derived from the theory of elastic binary collisions), *U* is the sublimation energy of the target material and α is a measure of the efficiency of momentum transfer in collisions. To obtain a quick estimate of *S*, the following approximation is often used

$$S \tilde{\propto} \frac{M_t}{T_m} \tag{2.2}$$

where M_t is the mass of the target atom and T_m is the melting point of the target material.

2.2.2 Sputtering of alloys and compounds

Compounds can be deposited from a compound target, but the deposition rate is low, because of high bond energies. Another method is reactive sputtering, where a metallic target is sputtered in the presence of a reactive gas which is usually mixed with the inert working gas.

There are three main ways in which alloys can be sputtered. Firstly, two or more single element targets can be used and the correct stoichiometry can be estimated by determining *S* for each element as described above. The ratio of the sputtering yields provides an initial estimate of what the ratio of the power applied to each target should be. However, normally a few trial runs are required before the desired alloy is obtained. Secondly, a composite target can be used and once again, the ratio of the sputter yields will tell you what percentage of the target should be element A, and so on. Finally, and indeed the most popular method is to use an alloy target. Unlike evaporation, where the different vapour pressures of the alloy components mean that the film is not of the same stoichiometry as the target, sputtered films in principle have the same stoichiometry as the target. Components do have different sputter yields, but the difference between sputter yields is much less than vapour pressures. However, the main reason is that since the target stays cool there is minimal solid state diffusion, so a steady state target surface composition is maintained. One problem is that the lighter atomic species will be scattered more by the sputtering gas, which may upset the stoichiometry.

In this thesis, in which for the Sm-Co system we were interested in investigating a range of film compositions and in the case of the Heusler alloy, Co_2MnSi it was important that stoichiometric

films were obtained, films were grown from separate, elemental targets. This leads us on to thinking about the combinatorial approach to materials research.

2.2.3 Combinatorial Growth

In this approach a large number of samples with different compositions are synthesised in one deposition sequence and characterised rapidly in order to dramatically increase the rate of materials discovery and optimisation. This method has been used in the search for advanced functional materials including superconductors,[13] dielectric[14] and magnetoresistance[15] materials. Composition variation across substrates has been achieved in a number of ways: spatially selective shadow deposition techniques[13-15] and co-deposition (sputtering or evaporation).[16,17,18] Recently the use of natural composition spreads created by co-sputtering of multiple target sources has been used to investigate a series of Ga-containing ternary Heusler alloy systems.[17]

2.2.4 Types of sputtering

2.2.4.1 Direct Current (DC) Sputtering

The mechanism of sputtering described above was based on a dc sputtering system. The deposition rate is one of the most important parameters and sputtering is often used because of the high deposition rates attainable. The deposition rate is affected by the sputtering gas pressure, the target power and the target-substrate distance, *d* (i.e. the distance between the electrodes). If the pressure is too low, then ions are produced far from the target and so it is likely that the ions will be lost to the chamber walls before reaching the target. Since the mean free path (mfp) of the electrons is large, the ionisation rate of the argon gas will be low so the plasma cannot be sustained at a low pressure. However, if the pressure is too high, the sputtered atoms will undergo many collisions and many of them will not reach the substrate. Therefore, there is a trade-off and the optimum sputtering parameters have to be determined. The voltage is limited by the output impedance of the power supply. A large proportion of the incident energy is lost in the target in the form of heat, so the target must be water cooled during sputtering. In general it is found that

$$\text{Deposition rate} = \frac{kW}{d^2} \qquad (2.3)$$

where *W* is the power and k is a constant. Therefore simple dc-glow discharge sputtering is a fairly inefficient process because it is dependent on the rate of argon ions bombarding the target and the rate of ejected target atoms reaching the substrate. There are various ways to improve the efficiency, and one of the most commonly employed techniques is magnetron sputtering.

2.2.4.2 Magnetron sputtering

We will just consider a planar magnetron, although there are different configurations (e.g. toroidal, toroidal-conical and cylindrical) depending on the sputtering geometry required. The magnetron basically consists of an iron block with a cavity in the centre in which there is a copper/aluminium spacer and a very strong permanent magnet such as $SmCo_5$. The iron block is attached to a copper backing plate and there is a water inlet and outlet to cool the magnetron.

The magnetic field lines are initially normal to the target, then bend with a component parallel to the target surface (this is the magnetron component) and return into the target, completing the magnetic circuit. During sputtering, there is an electric field ***E*** acting perpendicular to the target surface and a magnetic field oriented parallel to the target surface, as shown in figure 2.8. The Lorentz force describes how an electron would behave in crossed magnetic and electric fields.

$$\mathbf{F} = m\frac{dv}{dt} = -q(\mathbf{E} + \mathbf{v}\times\mathbf{B}) \qquad (2.4)$$

where *q*, *m* and *v* are the electron charge, mass and velocity, respectively.
An electron emitted from the cathode would be accelerated towards the anode but on experiencing the region of the parallel magnetic field is bent back towards the target. It therefore executes a cycloidal motion, which means that electrons are trapped near the target surface, increasing the collision probability with a gas atom. This leads to larger currents and increased deposition rates. The plasma can be sustained at a lower pressure, typically 10^{-5} to 10^{-3} Torr so there is a larger pressure range in which sputtering can occur.

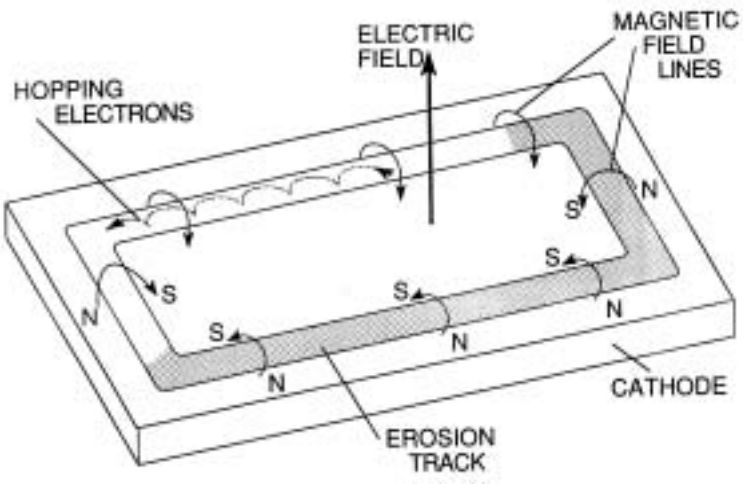

Fig. 2.8. Plan view of a planar magnetron.[11]

Magnetron sputtering is the most popular sputtering method because of the high deposition rates attainable (e.g. up to 1 μm/min). This is about an order of magnitude higher than conventional sputtering techniques.

2.2.4.3 Radio frequency (RF) sputtering

This was developed to deposit insulating films. A high frequency ac power supply is employed. RF frequencies in the range of 5 to 30 MHz are used although 13.56 MHz is the most common. The target develops a negative potential because electrons are more mobile than ions and once this has occurred it resembles a dc target. Oscillating electrons acquire enough energy to ionise the argon molecules, so we are no longer reliant on secondary electrons to sustain the discharge. Therefore, the discharge can be maintained at lower pressures and for this reason RF sputtering is sometimes used for conducting targets. RF voltages can be coupled through any impedance so insulating targets are possible. Oxides and even polymers can be sputtered in this way.

2.2.5 Growth processes and structures

Three growth modes have been described, as illustrated in figure 2.9. Island (or Volmer-Weber) growth occurs when atoms/molecules are more strongly bound to each other than to the substrate. Layer (or Frank-van der Merwe) growth results when atoms are more strongly bound to the substrate. Finally there can be a combination of the above growth processes, known as layer and island (or Stranski-Krastanov) growth. This happens if there is a change in energy with successive layers, for example strain energy or lattice mismatch.

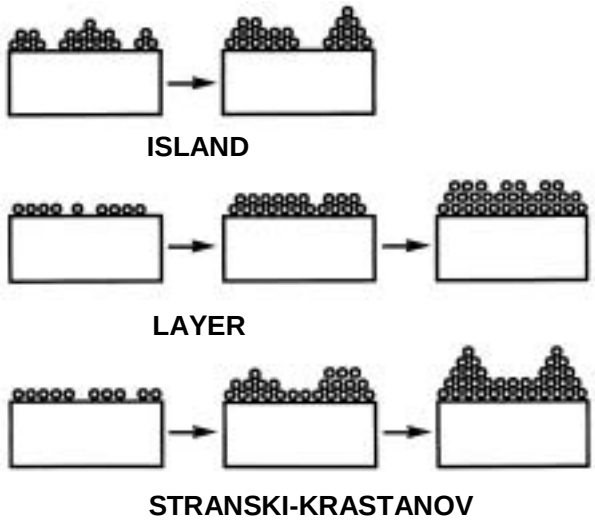

Fig. 2.9. Growth modes in a thin film (adapted from [11]).

These growth modes describe the early stages of film growth. We will now consider, Thornton's zone model,[19] which describes the grain structure of thick polycrystalline films as a function of substrate temperature, T_{sub} and inert gas pressure (Fig. 2.10). The zone 1 structure exists when there is very low mobility. This is the case at low deposition temperatures T_{sub} and high sputtering gas pressures. The film consists of fine-scale crystallites with domed tops and voided boundaries. The internal crystal structure is poorly defined and there is a high dislocation density. The Zone T, or "transition zone" structure is denser (atoms have a higher mobility), resulting in a relatively smooth surface. The zone 2 structure consists of columnar grains which extend through the film thickness ending in faceted surfaces. The columnar microstructure consists of parallel rod-shaped columns of high density surrounded by regions of lower density material. This microstructure is very common in thin films as it is observed when the mobility of atoms is limited, which is a frequent occurrence in sputtered thin films. Columnar grains have been observed in high-melting-point materials (e.g. Cr, Si, Ge), in compounds of high binding energy (e.g. TiC, TiN) and in non-noble metals evaporated in the presence of oxygen (e.g. Fe). Amorphous films of rare earth-transition metal alloys, such as Sm-Co, which naturally require low adatom mobility, are often columnar if deposited at a low enough temperature.

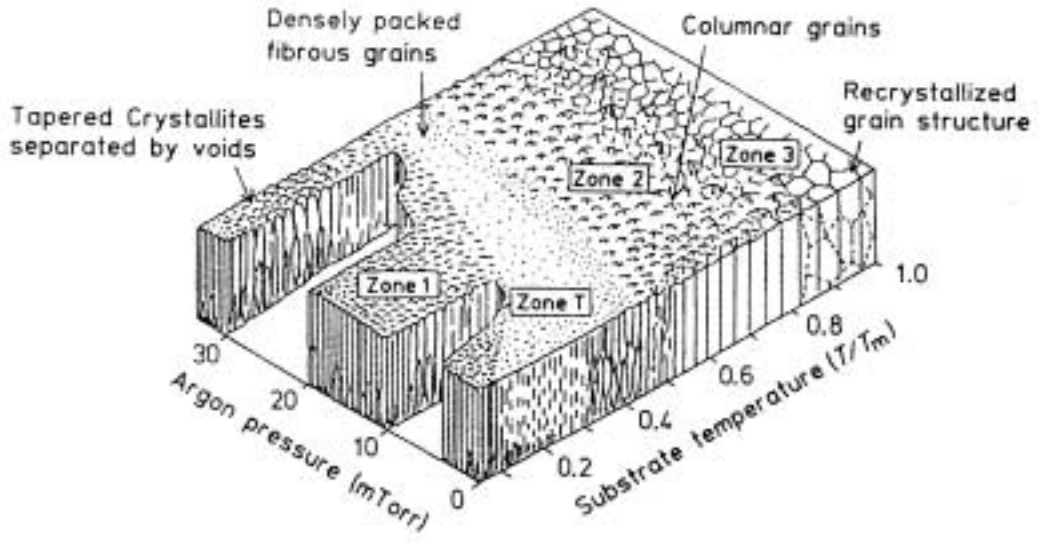

Fig. 2.10. Thornton's zone model.[19]

Finally, the zone 3 structure exists at high T_{sub}. Broad, squat grains are formed with smooth surfaces and grooved boundaries. Columnar structures may exist, even at very high T_{sub}. Thornton's zone model has illustrated the effects of pressure and T_{sub} on the film structure, but the deposition rate will also affect the structure. A high deposition rate means that there will be a high

nucleation rate, so a fine grained, even amorphous structure might be obtained. The film will be continuous but of low crystalline quality, since not all the adatoms will have found their equilibrium sites before the next layer is deposited. The film quality could be improved by increasing T_{sub}. A low deposition rate would lead to fewer nuclei and the film would consist of coarse grains and a discontinuous structure for low film thickness.

2.2.5.1 Epitaxial growth

Epitaxy refers to extended single-crystal film formation on top of a crystalline substrate. The low lattice mismatch between Heusler alloys and semiconductors, means that epitaxial growth should be possible and desirable since it is thought that single crystal films should have superior properties to polycrystalline ones.[20] There are two main types of epitaxy: homoepitaxy, where the film and substrate are the same material and heteroepitaxy, where the film and substrate are composed of different materials. This is illustrated schematically in Fig. 2.11. The fundamental criterion for epitaxy is defined by the lattice mismatch, f

$$f = \frac{a_s - a_f}{a_s} \tag{2.5}$$

where a_s and a_f are the lattice parameters of the substrate and film respectively. Ideally, for high quality epitaxial growth, the lattice mismatch should be as small as possible (generally less than 10 %).[21]

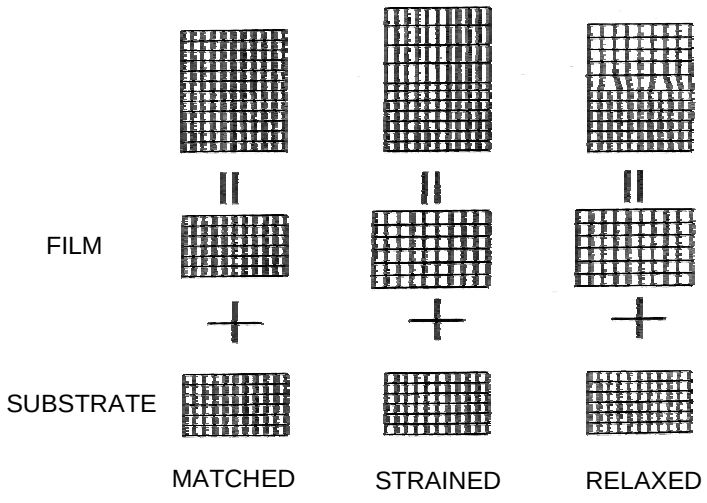

Fig. 2.11. Schematic illustration of lattice-matched, strained, and relaxed heteroepitaxial structures (adapted from [11]).

If the lattice mismatch is very small, lattice-matched heteroepitaxy tends to occur (case 1 in Fig. 2.11) which is structurally very similar to homoepitaxy. If the mismatch is larger, then either dislocation defects form at the interface, or the two lattices strain to accommodate their crystallographic differences (pseudomorphic growth). The former case often happens anyway during the later stages of film growth irrespective of crystal structure or lattice parameter differences. The formation of dislocations can be detrimental to the performance of semiconductors.

2.3 Magnetic properties

All the materials investigated in this thesis are ferromagnetic. Ferromagnetic materials possess a spontaneous magnetisation below the Curie temperature, T_c i.e. a magnetisation in the absence of an applied field. This is the result of the Heisenberg exchange interaction for which the magnetic energy is lower if the ionic magnetic moments are parallel and cooperatively aligned. If these materials are heated above T_c, the spontaneous magnetisation disappears and the materials become paramagnetic with effectively randomly oriented ionic magnetic moments. The physics of ferromagnetism is very involved and could not possibly be discussed in its entirety here. However, the terminology used in this work will be explained in this section. For a more detailed discussion of ferromagnetism I strongly recommend a book by Chikazumi.[22]

2.3.1 Definitions and units

There are many terms in magnetism, which are given different names and symbols by different authors, so I have provided a list of symbols and abbreviations at the beginning of this work and the main terms used in this work are defined here (in cgs units, see table 2.1).

Consider the force of attraction and repulsion between two magnets. This can be described by assuming that there are 'free' magnetic poles on the ends of each magnet, which exert forces on one another. Consider two magnetic poles of strengths p_1 and p_2 separated by a distance d (cm). Then the force, $\boldsymbol{F}$ (dyne) exerted on one pole by the other is given by

$$\mathbf{F} = \frac{p_1 p_2}{d^2} \qquad (2.6)$$

where the proportionality constant has been put equal to 1.

A ***magnetic field*** is a region of space in which a magnetic pole of strength, p experiences an applied force.

The ***magnetic field strength***, $\boldsymbol{H}$ (Oe (Oersted)), can be thought of as,

$$\mathbf{H} = \frac{p}{d^2} \tag{2.7}$$

where d is the distance from the pole.

Consider a magnet with poles of strength *p* located near each end and separated by a distance *l*. If the magnet is placed at 90° to a uniform field, ***H*** of magnitude 1 Oe, then the ***magnetic moment, m*** (emu) of the magnet is

$$\mathbf{m} = p\mathbf{l} \tag{2.8}$$

p and *l* are indeterminate, uncertain quantities but the magnetic moment, ***m*** can be precisely measured.

The ***magnetisation***, ***M*** **(**emu/cc) is simply the magnetic moment per unit volume.

The ***magnetic induction, B*** (G (gauss)) is given by

$$\mathbf{B} = \mathbf{H} + 4\pi\mathbf{M} \tag{2.9}$$

There are two main systems of units in widespread use in magnetism: SI (or MKS) and Gaussian (or CGS). Each of these unit systems have certain advantages and disadvantages. The SI system takes an electrodynamic approach to magnetism based on electric currents whereas the CGS system is based on magnetostatics and the concept of the 'magnetic pole'. In this thesis, where we mainly discuss saturation magnetisation, M_s and coercivity, H_c, cgs units are used (with the exception of chapter 9 where for the convenience of the measurement system used, ***H*** is in SI units). Some of the common magnetic quantities, their units and some conversions are provided in table 2.1.

Quantity	cgs units	SI units
Field equation	$\boldsymbol{B}=\boldsymbol{H}+4\pi\boldsymbol{M}$	$\boldsymbol{B}=\mu_0(\boldsymbol{H}+\boldsymbol{M})$
Induction	***B*** in gauss (G)	***B*** in tesla (T)
Field	***H*** in oersteds (Oe)	***H*** in amperes/metre (A/m)
Magnetisation	***M*** in emu/cc	***M*** in amperes/metre (A/m)
Conversions	cgs to SI	SI to cgs
	B: 1 G = 10^{-4} T	1 T = 10^4 G
	H: 1 Oe = $(10^3/4\pi)$ A/m	1 A/m = $4\pi\times10^{-3}$ Oe
	M: 1 emu/cc = 10^3 A/m	1 A/m = 10^{-3} emu/cc

Table 2.1. Table of common magnetic quantities and their units and some conversions.

2.3.2 Magnetisation of ferromagnetic materials and demagnetising fields

Ferromagnetic materials can be highly magnetised by a magnetic field, retaining their magnetisation even when the field is removed. Figure 2.12 shows a hysteresis loop of the magnetisation of a ferromagnet as a function of applied field. Starting from a demagnetised state denoted by the letter O ($\boldsymbol{M}$=$\boldsymbol{H}$=0), $\boldsymbol{M}$ increases with increasing $\boldsymbol{H}$ along the curve OABC until the saturation magnetisation, M_s (C) is reached. The process of magnetisation is almost reversible in section OA (the magnetisation would return to zero upon removal of the applied field) but beyond this the processes of magnetisation are irreversible (discussed further in section 2.3.5.2). If the magnetic field is decreased from the saturated state C, the magnetisation gradually decreases along CD (not along CBAO) and at $\boldsymbol{H}$=0 it reaches the non-zero value M_r (D), which is the remanence. Increase of the magnetic field in the negative sense results in a continued decrease in the magnetisation, which falls to zero at the point E, known as the coercive field H_c. Section DE of the curve is often referred to as the demagnetising curve. Further increase of $\boldsymbol{H}$ in a negative sense results in an increase in the magnetisation in a negative sense, and the negative saturation magnetisation is reached at point F. If the field is then reduced to zero and then increased in the positive sense, the magnetisation increases along FGC. The closed loop CDEFGC is called a hysteresis loop.

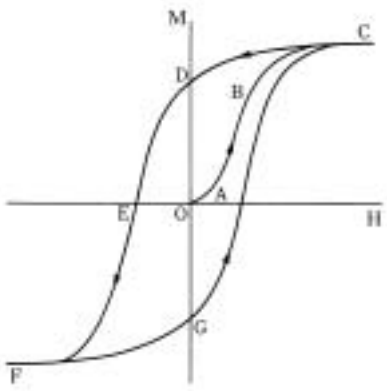

Fig. 2.12. Hysteresis loop (adapted from [22]).

The apparent magnetisation curve of a material is dependent on the shape of the specimen, and so we need to consider the demagnetising field. Consider the bar in Fig. 2.13 is magnetised by a field applied from left to right, and the field is then removed. A north pole is formed at the right end and a south pole at the other end. The lines of $\boldsymbol{H}$ radiate out from the north pole and end at the south pole. The field inside the magnet acts from north to south and tends to demagnetise the magnet. This demagnetising field $\boldsymbol{H_d}$ acts in the opposite direction to $\boldsymbol{M}$, which creates it. Figure 2.13a) shows $\boldsymbol{H}$ inside and outside the bar. $\boldsymbol{H_d}$ is the only field acting, and from the relationship

$\boldsymbol{B} = \boldsymbol{H} + 4\pi\boldsymbol{M}$, we find that $\boldsymbol{B} = -\boldsymbol{H_d} + 4\pi\boldsymbol{M}$. The induction inside the magnet is less than $4\pi\boldsymbol{M}$ but in the same direction, since $\boldsymbol{H}_d$ can never exceed $4\pi\boldsymbol{M}$ in magnitude. The vectors are shown in Fig. 2.13b) and the $\boldsymbol{B}$ field of the magnet is also illustrated. The lines of $\boldsymbol{B}$ are continuous and inside

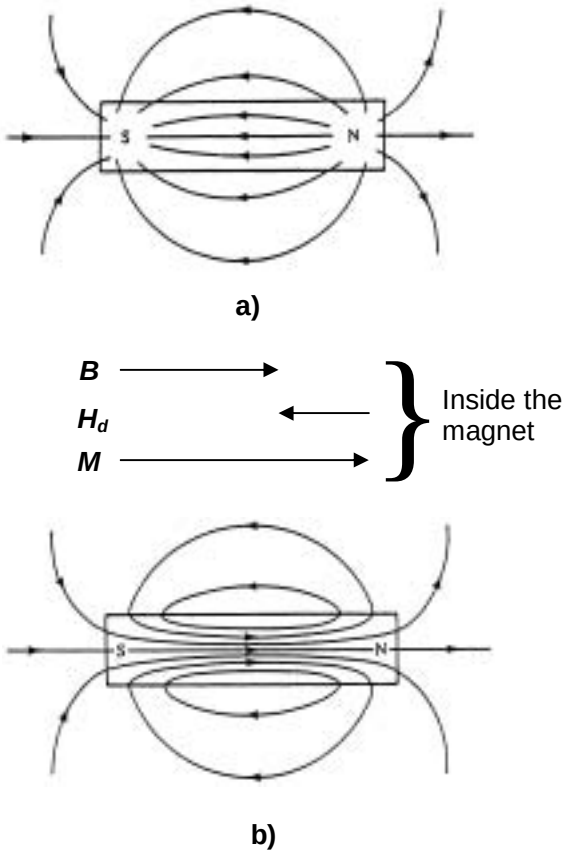

Fig. 2.13. a) $\boldsymbol{H}$ inside and outside a bar magnet, b) $\boldsymbol{B}$ inside and outside a bar magnet (adapted from [23]).

the magnet they are directed from S to N. The field lines $\boldsymbol{H}$ around the bar magnet are the same as the flux lines $\boldsymbol{B}$ outside the material since $\boldsymbol{B} = \mu_0\boldsymbol{H}$ in free space. However, inside the material they are different and $\boldsymbol{B}$ and $\boldsymbol{H}$ point in different directions because of the magnetisation $\boldsymbol{M}$ of the material. The magnetisation vector, $\boldsymbol{M}$ inside a magnetised ferromagnet points from S to N as this is the convention adopted for the definition of the magnetic moment for a magnetic dipole. The magnetic field $\boldsymbol{H}$ always points from a 'north pole' to a 'south pole'. Fig. 2.13b) illustrates that the magnetisation of the bar magnet is not uniform and this results from the fact that $\boldsymbol{H}_d$ is stronger near the poles. The demagnetising field, $\boldsymbol{H}_d$ is always present whenever magnetic poles are created in a material. This field depends on two factors: the magnetisation of the material (i.e. the pole strength) and the shape of the specimen (i.e. the pole separation which is determined by the sample geometry). $\boldsymbol{H}_d$ is proportional to $\boldsymbol{M}$ and is given by the expression

$$\mathbf{H}_d = N_d \mathbf{M} \qquad (2.10)$$

where, N_d is the demagnetising factor which is calculated from the sample geometry. N_d approaches zero for an elongated thin specimen, which is magnetised along its long axis whereas it is large for a thick and short specimen. The demagnetisation factor also depends on the direction of the magnetisation. Consider the semi-infinite plate shown in Fig. 2.14. This can be seen as the geometry of the thin films that are measured in this work. If the plate is magnetised perpendicular to its surface, $N_d = -4\pi$ and so $\boldsymbol{H}_d = -4\pi\boldsymbol{M}$. If the plate is magnetised parallel to its surface then the effect of the free poles is negligible, so N=0 and so $\boldsymbol{H}_d = 0$.

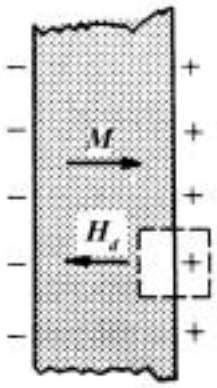

Fig. 2.14. Demagnetising field produced by magnetisation perpendicular to the surface of a magnetic plate (adapted from [22]).

Therefore, if $\boldsymbol{H}$ is perpendicular to the plane of the thin film $\boldsymbol{H_d}$ is large and the shape of the magnetisation curve is sheared compared to the true magnetisation curve (Fig. 2.15).

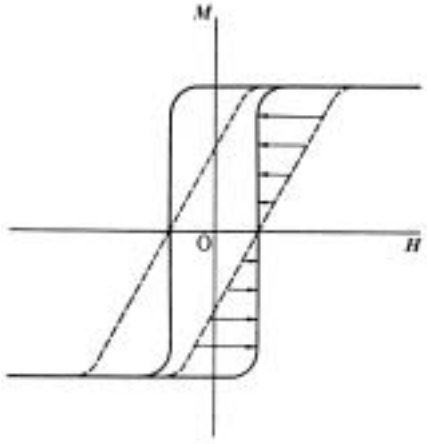

Fig. 2.15. Shearing correction of a magnetisation curve (adapted from [22]).

2.3.3 Energetics of ferromagnetic films

The total energy of a ferromagnetic material of a finite size in an applied magnetic field is given by the sum of the Zeeman energy, exchange energy, anisotropy energies and magnetostatic energy as shown in equation 2.11.

$$E_{tot} = \int (E_{Zee} + E_{ex} + E_a + E_m) dV \qquad (2.11)$$

The first term, the Zeeman energy results from the interaction of $\boldsymbol{H}$ and $\boldsymbol{M}$, and is given by

$$E_{Zee} = -\mathbf{H} \cdot \mathbf{M} \qquad (2.12)$$

The second term, the exchange energy, is the energy between the atomic magnetic moments and tends to align them parallel for a ferromagnetic material and antiparallel for an antiferromagnetic material. This is described by Heisenberg's expression,

$$E_{ex} = -2\sum_{ij} J_{ij} \mathbf{S}_i \cdot \mathbf{S}_j \qquad (2.13)$$

where J_{ij} is the exchange constant between two atomic spins $\boldsymbol{S_i}$ and $\boldsymbol{S_j}$. The sign convention of J_{ij} is such that positive J_{ij} implies a parallel alignment of spins is preferred, which is the case for a ferromagnet.

The crystalline anisotropy energy is due to spin-orbit coupling and depends on the direction of magnetisation relative to the crystal axes. Magnetic anisotropy is discussed in the following section.

The final term, the magnetostatic energy arises from the self-energy created by free magnetic poles and is dependent on the shape and size of the sample and thus leads to an additional anisotropy.

There are two main reasons for hysteresis in ferromagnetic materials. The first is imperfections in the material such as dislocations and impurities, which increase the energy lost during the magnetisation process in the form of a kind of internal friction. The second mechanism is magnetocrystalline anisotropy (in the easy direction). Ferromagnetic materials with a larger anisotropy exhibit greater hysteresis in the easy direction.

2.3.4 Magnetic anisotropy

There are five main types of anisotropy: magnetocrystalline anisotropy (also known as crystal anisotropy), shape anisotropy, stress anisotropy, anisotropy induced by magnetic annealing and exchange anisotropy. Only magnetocrystalline anisotropy is intrinsic to the material and this will be discussed in the following section along with shape anisotropy.

2.3.4.1 Magnetocrystalline anisotropy

The term magnetic anisotropy is used to describe the dependence of the internal energy on the direction of spontaneous magnetisation. Generally, the magnetic anisotropy energy term has the same symmetry as the crystal structure of the material, and so it is called magnetocrystalline anisotropy. Therefore, when a field is applied to a ferromagnetic material, the observed magnetisation depends on both the magnitude of the field and the crystallographic direction along which it is applied.

In a sufficiently large field, the magnetisation will reach the saturation value, which is the same for all the crystallographic directions. The crystallographic direction for which the magnetisation reaches saturation in the lowest applied field is known as the easy axis of magnetisation. This is the axis along which the magnetisation vectors of the domains lie in the absence of an applied field. The simplest case to consider is uniaxial magnetic anisotropy, which occurs in hcp materials such as cobalt. There is only one easy axis of magnetisation and this corresponds to the axis of hexagonal symmetry, [0001]. Therefore, the stable direction of spontaneous magnetisation at room temperature is parallel to the c-axis of the crystal. As the magnetisation rotates away from the easy axis, the anisotropy energy increases with angle and reaches a maximum value at $\theta=90^\circ$. This is known as the hard axis. The energy then decreases to its original value at $\theta=180^\circ$. The anisotropy energy is a minimum when the magnetisation points in either the + or – direction along the c-axis. This energy can be expressed by expanding it in a series of powers of $\sin^2\theta$:

$$E_a = K_0 + K_1 \sin^2\theta + K_2 \sin^4\theta + K_3 \sin^6\theta + K_4 \sin^6\theta\cos 6\varphi + \ldots\ldots \quad (2.14)$$

The coefficients are called anisotropy constants. The higher order terms are small so we can approximate the above as

$$E_a = K_0 + K_1 \sin^2\theta \quad (2.15)$$

For cobalt we find that,

$$E_a = K_0 \qquad \text{for } \boldsymbol{M} \text{ parallel to the easy axis}$$

$$E_a = K_0 + K_1 \quad \text{for } \boldsymbol{M} \text{ perpendicular to the easy axis}$$

Therefore, the difference in the energy of magnetisation per unit volume of material is simply K_1 (Jm^{-3}) by subtracting the above equations. The magnetisation curves for cobalt in the easy and hard directions are shown in Fig. 2.16. So far, we have considered single crystals. In a polycrystalline sample, where the grains are randomly oriented, the anisotropy of the grains will average out and the body on the whole will exhibit no magnetocrystalline anisotropy. However, this is rare and samples are often textured so the polycrystalline aggregate will have an anisotropy dictated by that of the individual crystals.

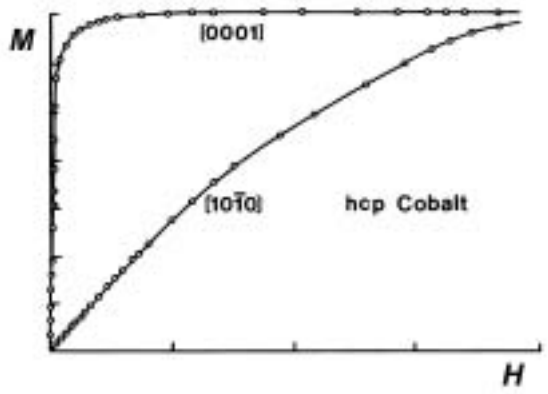

Fig. 2.16. Magnetisation curves along the easy and hard axes for cobalt (adapted from [2]).

2.3.4.2 Shape anisotropy

An applied field will magnetise a spherical sample to the same extent in any direction. A non-spherical sample will be easier to magnetise along a long axis as opposed to a short axis due to demagnetising effects, as discussed in section 2.3.2.

2.3.5 Domain processes

Although ferromagnetic materials are spontaneously magnetised, they may show no macroscopically observable magnetisation. This is because of the presence of magnetic domains, which are spontaneously magnetised regions of material separated by domain walls. The magnetisation vectors of the domains are arranged in such a way that their vector sum is zero, so that there are closed magnetic flux paths within the material and no net observable magnetisation.

Domains exist in order to minimise energy. A single domain specimen, shown in Fig. 2.17(A) has a large magnetostatic energy E_m associated with the leakage of magnetic flux into the surrounding

air space. The magnetostatic energy (or self-energy) is basically the energy associated with the demagnetising field of the specimen. E_m (ergs/cc) of a single-domain particle is given by

$$E_m = \frac{1}{2} N_d \mathbf{M}^2 \qquad (2.16)$$

The leakage of flux can be reduced if the material is divided into domains and in the final closed loop structure (E) there is no flux leakage at all (assuming the specimen is sufficiently large). These are closure domains and they are nucleated by defects including the boundary of the material. They are usually the last domains to be swept out at higher fields. The division into domains will cease once the energy expended in forming a domain wall is greater than the reduction in magnetostatic energy.

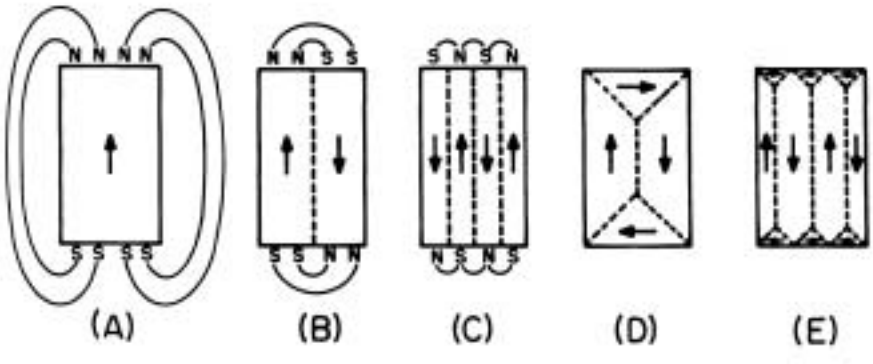

Fig. 2.17. Emergence of domains as a saturated sample is demagnetised.[23]

2.3.5.1 Bloch Walls and Néel Walls

In Fig. 2.17, we observed 180° Bloch walls (B) and 90° Bloch walls (D). Bloch walls are basically transition layers in which the magnetic moments undergo a reorientation. The domain wall energy can be most simply defined as the difference in energy of the magnetic moments when they are part of the wall and when they are within the main body of the domain. The domain wall width in a ferromagnet can be determined by minimising the energy of the wall with respect to its width. The width of a 180° domain wall, δ is given by

$$\delta = \pi \left(\frac{kT_c}{aK_1} \right)^{1/2} \qquad (2.17)$$

where, k is Boltzmann's constant, a is the lattice spacing and K_1 is the magnetocrystalline anisotropy coefficient.

For a thin film specimen, the ferromagnetic domains can extend across the whole width of the specimen. In the case of the Bloch wall (Fig. 2.18), the magnetisation would be normal to the plane of the film, which causes a large magnetostatic energy. In the case of the Néel wall (Fig. 2.18), the moments rotate in the plane of the film, resulting in a lower energy. Therefore, in thin films the magnetisation is generally in plane because the magnetostatic energy is much lower. Néel walls do not occur in bulk specimens because they generate a rather high magnetostatic energy within the volume of the domain wall.

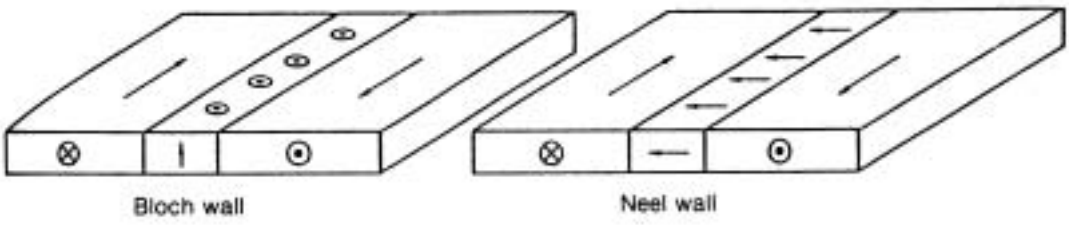

Fig. 2.18. A Bloch wall and a Néel wall in a thin film of a ferromagnetic material.[23]

2.3.5.2 Domain Processes

We will now consider what happens when a magnetic field is applied to a demagnetised ferromagnetic material. At low fields, domains which are aligned favourably with respect to the applied field grow at the expense of domains which are aligned in directions opposing the field. At intermediate field strengths, a second mechanism becomes significant; this is domain rotation in which the atomic magnetic moments within an unfavourably aligned domain overcome the anisotropy energy and suddenly rotate from their original direction of magnetisation into one of the crystallographic easy axes, which is nearest to the field direction. At high fields, coherent rotation occurs, where magnetic moments which are all aligned along an easy axis nearest to the field direction are gradually rotated into the field direction as the magnitude of the field is increased. This results in a single-domain sample. The two domain mechanisms discussed so far have been domain wall motion and domain rotation. Both of these processes can be reversible and irreversible and we can use these concepts to gain a better understanding of magnetic hysteresis.

Domain wall motion consists of domain wall bowing and domain wall translation. Domain wall bowing is a reversible process at low-field amplitudes. On application of a magnetic field, the domain wall expands like an elastic membrane and returns to its original position on removal of the field. However, the process becomes irreversible once the domain is sufficiently deformed that the expansion continues without further increase of field. The process can also become irreversible if the wall encounters pinning sites, which prevent it relaxing on removal of the field.

The translation of domain walls is usually an irreversible process unless the material is free from defects. A magnetic domain wall will see a magnetic energy potential as a function of distance because of short-range variations in strain due to dislocations and microstructural inhomogeneities such as the presence of particles of a second phase within the matrix material. These second-phase materials are known as magnetic inclusions and they reduce the energy of domain walls when the domain walls intersect them. They attract domain walls and effectively impede domain wall motion.

At low field amplitudes, domain rotation is reversible. The direction of alignment of the magnetic moments is displaced slightly from the easy axis towards the field direction. At intermediate to high-field amplitudes, the moments rotate from their original easy axis to the easy axis closest to the field direction. This occurs when the field energy has overcome the anisotropy energy and is an irreversible process. At high fields there is then a reversible rotation of the moments into the field direction. Finally, at very high fields there is another reversible change in which the magnetic moments within the single domain specimen are aligned more closely with the field direction.

2.4 Transport properties

2.4.1 Magnetoresistance (MR)

Magnetoresistance refers to the change in electrical resistance, ΔR of a material when a magnetic field is applied. The MR ratio is defined as the ratio of the change in resistance when the field is applied to the resistance at zero field,

$$MR = \frac{R_H - R_0}{R_0} = \frac{\Delta R}{R} \qquad (2.18)$$

A material that has a larger resistance in the presence of a field than in the absence of a field is defined to have a positive MR, whereas if the field reduces the resistance, the MR is negative.

Magnetoresistive materials are incorporated in a number of commercially available technologies such as magnetic sensors, magnetic recording heads and magnetic memories. In this section the various types of MR and their applications will be discussed.

2.4.1.1 Ordinary MR (OMR)

This occurs in normal metals due to the Lorentz force. The resistance is larger in the presence of a field than the resistance in the absence of the field. Therefore MR in normal metals is positive but is a small effect and has no technological applications.

2.4.1.2 Anisotropic MR (AMR)

Larger MR effects (of around 2 %) are observed in ferromagnetic materials and their alloys. The sign of the MR changes with the orientation of the applied field with respect to the measuring current. Generally, when the current is parallel to the applied field, the MR is positive (MR increases with increasing field) and the contrary is the case when the current is orthogonal to the applied field. The origin of AMR lies in the spin-orbit coupling and was first explained by Kondo.[24] AMR materials have been used as the read elements in recording heads.

2.4.1.3 Giant MR (GMR)

This effect is observed in multilayers consisting of alternating layers of ferromagnetic and nonmagnetic metals. The resistance is largest when the magnetic moments in the alternating layers are oppositely aligned (spin up electrons are scattered by regions of spin down magnetisation and vice versa) and smallest when they are aligned parallel (conduction electrons of compatible spin type can move through the heterostructure with minimal scattering). These two cases are schematically illustrated in Fig. 2.19. GMR was first observed by Baibich *et al*.[25] in 1988 in multilayers of Fe/Cr and a GMR as large as 50 % was observed at 4.2 K. Both GMR and AMR tend to be observed in a given device but GMR can be a much larger effect. In contrast to AMR, GMR is only dependent on the relative orientation of the magnetic moments of the layers. The devices can be made such that the current is parallel to the interfaces (CIP) as shown in Fig. 2.19, or perpendicular to the interfaces (CPP). The CPP geometry yields larger effects because there is no shunting of the current through normal metal layers. All the current must undergo spin scattering at every interface to traverse the layered structure.

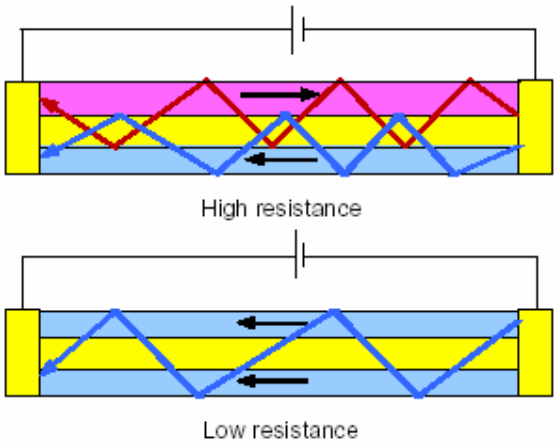

Fig. 2.19. Schematic representation of transport in a GMR device structure when the magnetic moments are aligned anti-parallel (high resistance state) and parallel (low resistance).[26]

From an application point of view, the GMR is particularly important not only because the effect is substantial but it is an extrinsically engineerable effect. IBM introduced the first GMR read head sensor in 1997, within 10 years of its initial discovery.

2.4.1.4 Tunnelling MR (TMR)

This involves two ferromagnetic layers separated by a very thin insulating layer. Upon applying a small voltage (less than the tunnel barrier height), electrons can quantum mechanically tunnel through the barrier. The tunnelling resistance has the same orientation dependence upon the magnetisations of the electrodes as the GMR effect but has a different physical origin. The magnitude of the effect tends to be larger and was first observed by Jullière[27] in a Fe-Ge-Co magnetic tunnel junction (MTJ) in 1975. However, it was not until 1995 that a large, reproducible TMR of 13.4 % at room temperature (31.6 % at 4.2 K) was reported by Moodera *et al*.[28] using an Al_2O_3 tunnel barrier.

2.4.2 Spin Polarisation (*P*)

The simplest definition of *P* is:

$$P_0 = \frac{N_\uparrow - N_\downarrow}{N_\uparrow + N_\downarrow} \qquad (2.19)$$

where, N is the density of states of majority or minority electrons at E_F.[29]

A more general and useful definition is:

$$P_n = \frac{N_\uparrow v_\uparrow^n - N_\downarrow v_\downarrow^n}{N_\uparrow v_\uparrow^n + N_\downarrow v_\downarrow^n} \tag{2.20}$$

where, v is the Fermi velocity, which weights the ↑ and ↓ electrons differently. Here $n = 0$ for photoemission measurements, $n = 1$ for ballistic transport and $n = 2$ for diffusive transport.[30] If P = 100 % the choice of definition is immaterial, but otherwise it depends on the method of measurement. Values of P range from 0 in normal, nonmagnetic metals (e.g. Cu, Au), to +100 % or –100 % in HMF (theoretically). The determination of P requires either a direct, spin-selective measurement of the DOS or a measurement of spin dependent transport. There are five main methods: Photoemission, MTJ, point contact, Tedrow-Meservey and Andreev reflection. For the case of the MTJ, P can be deduced by assuming that conduction in each spin channel is proportional to the corresponding DOS in each electrode. When the electrodes are identical, this gives the Jullière formula,[27]

$$MR = \frac{2P^2}{1+P^2} \tag{2.21}$$

However, the MR of MTJs depends critically on the electronic states at the interface and the barrier material.[31] Therefore the measured P is not intrinsic to the ferromagnet but to the particular device.

2.4.3 Temperature dependence of the resistivity in magnetic metals

The electrical resistivity, ρ of magnetic metals has three main contributions: scattering of charge carriers at lattice defects (impurity atoms or atomic disorder), lattice vibrations (phonons) and spin disorder. The scattering at lattice defects is generally independent of T. The contribution of phonons increases with increasing temperature and is proportional to T at high temperature. In magnetic metals there is a large contribution to ρ due to spin disorder and ρ increases with increasing T up to the Curie temperature, T_c and remains approximately constant above T_c.[32]

White *et al.*[33] found that the resistivity of the transition elements exhibited an almost linear dependence on T in the range 295 K to about 100 K, with the exception of V, Cr, Mn, and Fe, Ni, Co. Co, which is of particular interest in this thesis, showed linear behaviour below around 280 K, and above this ρ rises faster than linearly with increasing T.

The resistivity of normal ferromagnetic metals at low temperatures usually has a term proportional to T^2, ascribed to one-magnon scattering of conduction electrons (electron undergoes a spin-flip in

an inelastic scattering process involving the creation or annihilation of a magnon).[34,35] However, in a HMF at low temperature all the states at E_F are spin polarised and so spin-flip scattering is not possible. Therefore, for a HMF one expects the absence of a T^2 term in the resistivity. The first available magnetic scattering processes involve two magnons, which give rise to a term in the resistivity varying as $T^{9/2}$ (although this term is difficult to disentangle from regular scattering processes involving phonons).[36] Another feature, which is sometimes observed in HMF is an upturn in ρ at low temperatures (typically < 40 K). This is attributed to weak localisation,[37] which commonly occurs in disordered metallic systems. The conduction electrons have a very short mean free path and so interference between scattered waves may occur. If the electron waves maintain phase coherence along their path, closed loop paths offer the electron two paths of equal phase change (elastic, phononless scattering process). The probability of an electron returning to its starting point is increased and so the material shows an increase in resistivity as the temperature decreases due to this enhanced scattering. However, at higher temperatures, more phonons are excited and so inelastic scattering is more probable and so the probability of back-scattering is reduced, so the resistivity exhibits the expected decrease with decreasing temperature.

References

[1] D.A. Porter and K.E. Easterling, *Phase Transformations in Metals and Alloys*, 2 ed. (Chapman and Hall, 1992).

[2] R.A. McCurrie, *Ferromagnetic Materials: Structure and Properties*. (London: Academic, 1994).

[3] F. Heusler, Verh. Dtsch. Phys. Ges. **5**, 219 (1903).

[4] I. Galanakis and P. H. Dederichs, cond-mat/0408068 (2004).

[5] R. A. de Groot, F. M. Mueller, P. G. Vanengen, and K. H. J. Buschow, Phys. Rev. Lett. **50**, 2024 (1983).

[6] S. Ishida, S. Fujii, S. Kashiwagi, and S. Asano, J. Phys. Soc. Jpn. **64**, 2152 (1995).

[7] P. J. Brown, K. U. Neumann, P. J. Webster, and K. R. A. Ziebeck, J. Phys.:Condens. Matter **12**, 1827 (2000).

[8] S. Fujii, S. Sugimura, S. Ishida, and S. Asano, J. Phys.:Condens. Matter **2**, 8583 (1990).

[9] W.R. Grove, Philos. Trans. Faraday Soc. **87** (1852).

[10] I. Langmuir, General Electric Rev. **26**, 731 (1923).

[11] M. Ohring, *The Materials Science of Thin Films*, (Academic Press, 1992).

[12] S.A. Campbell, *The Science and Engineering of Microelectronic Fabrication*, (Oxford University Press, 2001).

[13] X. D. Xiang, X. D. Sun, G. Briceno, Y. L. Lou, K. A. Wang, H. Y. Chang, W. G. Wallacefreedman, S. W. Chen, and P. G. Schultz, Science **268**, 1738 (1995).

[14] H. Chang, C. Gao, I. Takeuchi, Y. Yoo, J. Wang, P. G. Schultz, X. D. Xiang, R. P. Sharma, M. Downes, and T. Venkatesan, Appl. Phys. Lett. **72**, 2185 (1998).

[15] G. Briceno, H. Y. Chang, X. D. Sun, P. G. Schultz, and X. D. Xiang, Science **270**, 273 (1995).

[16] R. B. van Dover, L. D. Schneemeyer, and R. M. Fleming, Nature **392**, 162 (1998).

[17] I. Takeuchi, O. O. Famodu, J. C. Read, M. A. Aronova, K. S. Chang, C. Craciunescu, S. E. Lofland, M. Wuttig, F. C. Wellstood, L. Knauss, and A. Orozco, Nat. Mater. **2**, 180 (2003).

[18] R. B. van Dover, M. Hong, E.M. Gyorgy, J.F. Dillon Jr., and S.D. Albiston, J. Appl. Phys **57**, 3897 (1985).

[19] J.A. Thornton, Ann. Rev. Mater. Sci. **7**, 239 (1977).

[20] R. D. James and M. Wuttig, Philos. Mag. A **77**, 1273 (1998).

[21] D. W. Pashley, Advan. Phys. **5**, 173 (1956).

[22] S. Chikazumi, *Physics of Ferromagnetism*, 2 ed. (Oxford Science Publications, 1997).

[23] D. Jiles, *Introduction to Magnetism and Magnetic Materials*, 2 ed. (Chapman and Hall, 1998).

[24] J. Kondo, Prog. Theor. Phys. **27**, 772 (1962).

[25] M. N. Baibich, J. M. Broto, A. Fert, F. N. Vandau, F. Petroff, P. Eitenne, G. Creuzet, A. Friederich, and J. Chazelas, Phys. Rev. Lett. **61**, 2472 (1988).

[26] G. A. Prinz, Science **282**, 1660 (1998).

[27] M. Julliere, Phys. Lett. A **54**, 225 (1975).

[28] J. S. Moodera, L. R. Kinder, T. M. Wong, and R. Meservey, Phys. Rev. Lett. **74**, 3273 (1995).

[29] I. I. Mazin, Phys. Rev. Lett. **83**, 1427 (1999).

[30] J. M. D. Coey and S. Sanvito, J. Phys. D-Appl. Phys. **37**, 988 (2004).

[31] J. M. De Teresa, A. Barthelemy, A. Fert, J. P. Contour, F. Montaigne, and P. Seneor, Science **286**, 507 (1999).

[32] P. G. de Gennes and J. Friedel, J. Phys. Chem. Solids **4**, 71 (1958).

[33] G. K. White and S. B. Woods, Philos. Trans. Roy. Soc. A **251**, 273 (1959).

[34] I. Mannari, Prog. Theor. Phys. **22**, 335 (1959).

[35] M. J. Otto, R. A. M. Vanwoerden, P. J. Vandervalk, J. Wijngaard, C. F. Vanbruggen, and C. Haas, J. Phys.:Condens. Matter **1**, 2351 (1989).

[36] K. Kubo and N. Ohata, J. Phys. Soc. Jap. **33**, 21 (1972).

[37] P. A. Lee and T. V. Ramakrishnan, Rev. Mod. Phys. **57**, 287 (1985).

"Measure what is measurable, and make measurable what is not so."
Galileo Galilei.

Chapter 3

Experimental methods

In this chapter the experimental procedures used to fabricate and characterise thin films of Sm-Co and the Heusler alloy Co_2MnSi are described.

3.1 Substrate preparation

Sm-Co films were deposited onto fused quartz substrates (5×5 mm^2, 5×10 mm^2 for XRD work) and some of the Co_2MnSi films were grown on a-plane sapphire substrates (4×4 mm^2, 4×9 mm^2). Wafers of these substrate materials were cut using a dicing saw. These wafers were mounted on a glass disc using wax to prevent movement during cutting. Sapphire is very brittle and so the rotating blade traverses slowly across the wafer in order to prevent substrate chipping. It is crucial that the substrates are cleaned thoroughly after cutting to remove the wax and other contaminants. The substrates were cleaned ultrasonically in a bath of chloroform for 20 mins, followed by acetone for 20 mins and finally isopropanol for 5 mins. They were then dried using an airgun. As described in chapter 8, some of the Co_2MnSi films were grown on GaAs(001) and the dicing saw was unsuitable for cutting the GaAs(001) wafer because the surface is easily scratched and chipped. GaAs(001) cleaves very easily in the <110> directions and so a diamond scribe and anvil were used to cut the wafer into 4×4 mm^2 and 4×9 mm^2 pieces. This produces some dust that can easily be removed with an airgun.

3.2 Film deposition

3.2.1 Deposition of Sm-Co thin films

Thin films of Sm-Co were deposited in an ultra high vacuum (UHV) sputtering system (Cambridge Device Materials MkIII). A schematic of the MkIII is shown in Fig. 3.1. Film growth occurs in the inner chamber, which is isolated from the outer chamber by a valve and there is a liquid nitrogen jacket inbetween. Prior to loading, substrates were cleaned with an acetone jet, followed immediately by a propanol jet and were thoroughly dried with the air gun. They were then placed on the substrate tray, shown schematically in Fig. 3.2 (also depicted in yellow in Fig. 3.1). The tray enables a large number of films to be deposited in one run, each film having a different composition and hence different magnetic properties. The distance of the substrates from the targets (depicted in red) can be varied by changing the number of stainless steel spacers (depicted in grey).

The system was evacuated using the rotary and diffusion pump. The rotary pump is used to produce the minimum vacuum required to operate the diffusion pump, which can attain much lower pressures and therefore provides the necessary UHV conditions. The rotary pump also backs the diffusion pump. The system was left pumping overnight and baked at about 423 K for 5-6 hours to remove water from the system. Water is difficult to remove because it has an intermediate adsorption energy. If outgassing species have a low adsorption energy, such as inert

gases, they desorb from the chamber walls very rapidly so are easily pumped away. Species with a high adsorption energy are unlikely to be desorbed so do not pose a problem.

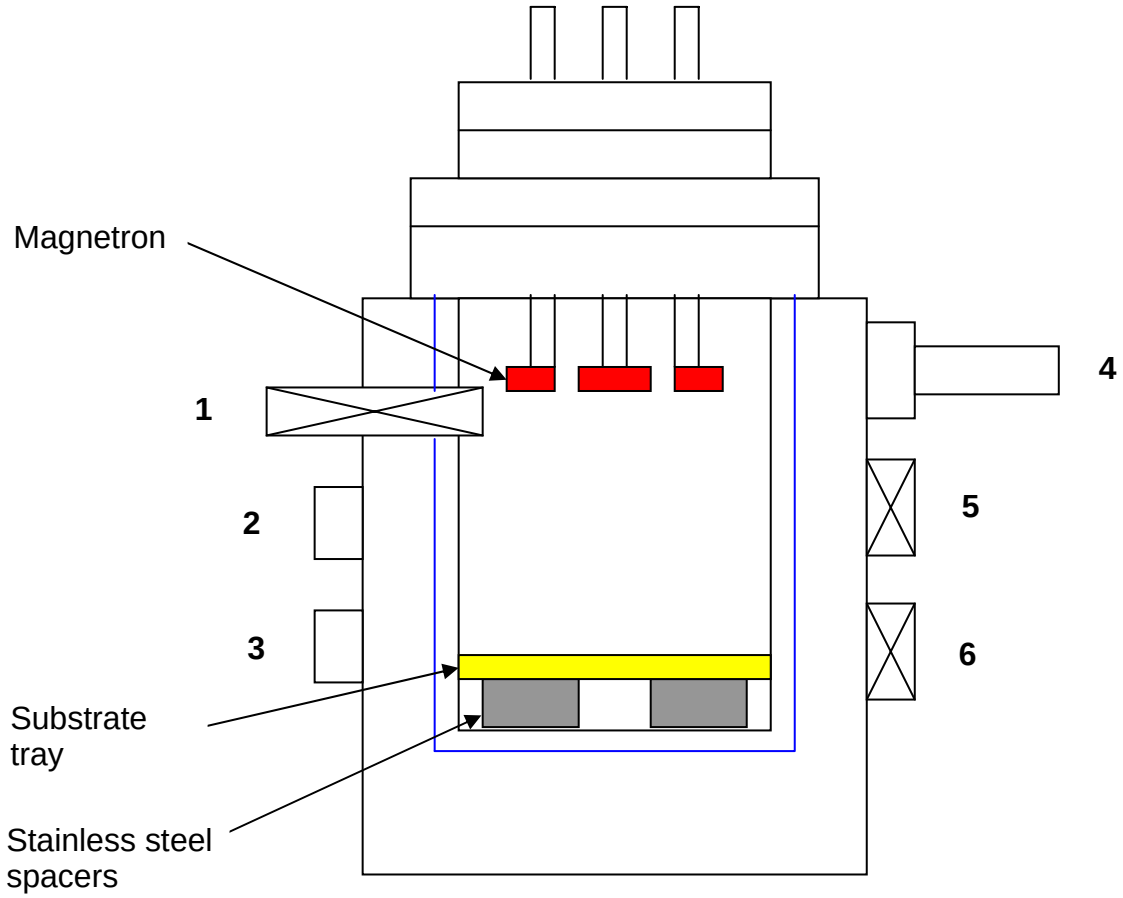

Key

1. Valve that connects inner and outer chamber.
2. Baratron
3. Needle valve
4. Mass spectrometer
5. Gate valve
6. Roughing valve for chamber

Fig. 3.1. Schematic diagram of the MkIII UHV sputtering system.

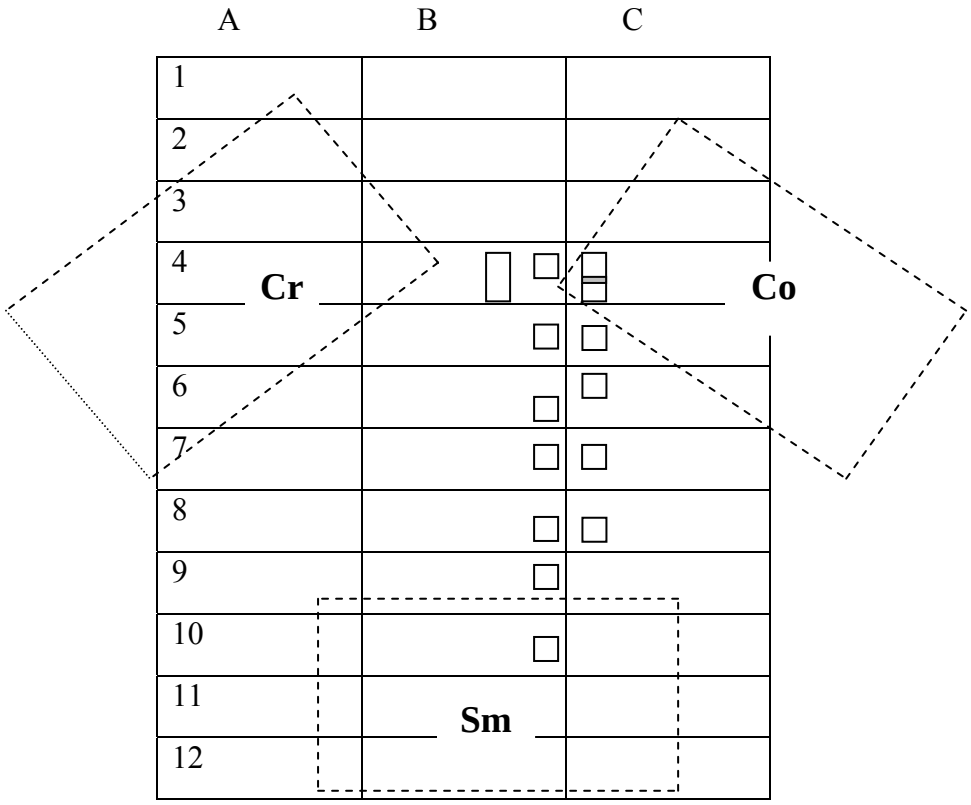

Fig. 3.2. Schematic plan view of the substrate tray, with the position of the sputtering targets relative to the substrate tray represented by dotted lines (targets are normally around 108 mm above the substrates). The Cr target was used to deposit the underlayer, described in section 5.4.

It is important after a bake-out to check that there are no leaks. In order to detect large leaks, the gate valve can be closed and the chamber pressure should be observed using the baratron. If the pressure is steady, there is no leak. If the pressure is rising, then one can determine whether it is gas leakage or outgassing from the chamber walls, by recording the pressure rise with time. Gas leakage causes a linear rise with pressure, whereas outgassing results in a pressure rise that becomes gradually smaller and tends to a limiting value. A typical base pressure obtained after a bake out is 1×10^{-6} Pa. This is determined by means of a mass spectrometer, which also gives the partial pressures of components such as, water, nitrogen and oxygen. Therefore another way to detect an air leak is to check whether the ratio of nitrogen to oxygen is 4:1. The liquid nitrogen jacket is then filled and this reduces the base pressure to around 3×10^{-7} Pa by freezing the gaseous impurities to the chamber walls.

In order to control the admission of sputtering gas (Ar) to the inner chamber during the deposition, a needle valve connects the outer chamber to the gas reservoir. The sputtering gas used is 6 nines pure argon and the reservoir is filled with about 50 kPa of this. A pressure of about 10 Pa is required to start the plasma, and then the pressure is reduced for the presputter. This is when the

target is sputtered (with the shutter in the closed position so the substrates are not coated) in order to remove any surface contaminants (e.g. oxide), equilibrate the target surface and to cover the surrounding area with this material so that impurities from the walls are not sputtered onto the substrates.

3.2.2 Deposition of Co_2MnSi thin films

Having gained experience in depositing a binary alloy, the aim was to design a sputtering flange to deposit the ternary intermetallic compound, Co_2MnSi. This would require three elemental targets and a heater, so a larger flange and hence a larger sputtering system would be needed. The flange size was scaled up from 200 mm in diameter to 250 mm. A schematic of the larger UHV sputtering system (Cambridge Device Materials MkVII) is shown in Fig. 3.3 and a photograph of the system in use with my flange is provided in Fig. 3.4.

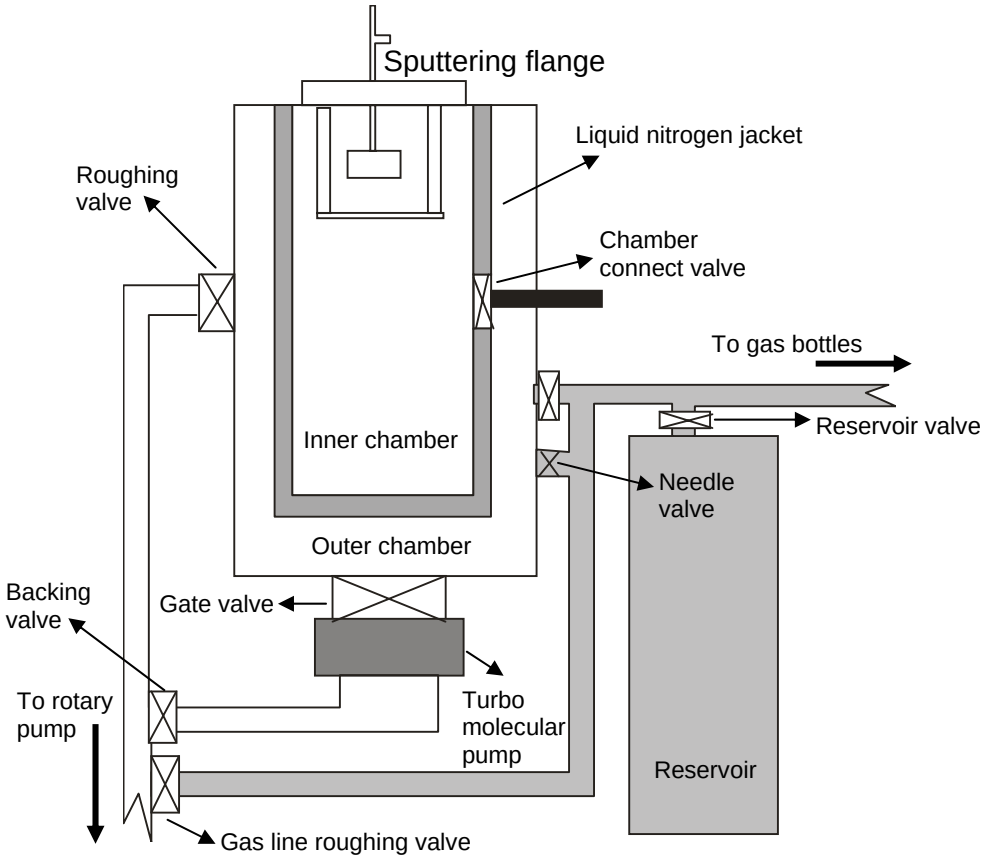

Fig. 3.3. Schematic of the MkVII system sputtering system (courtesy of Dr G. Burnell).

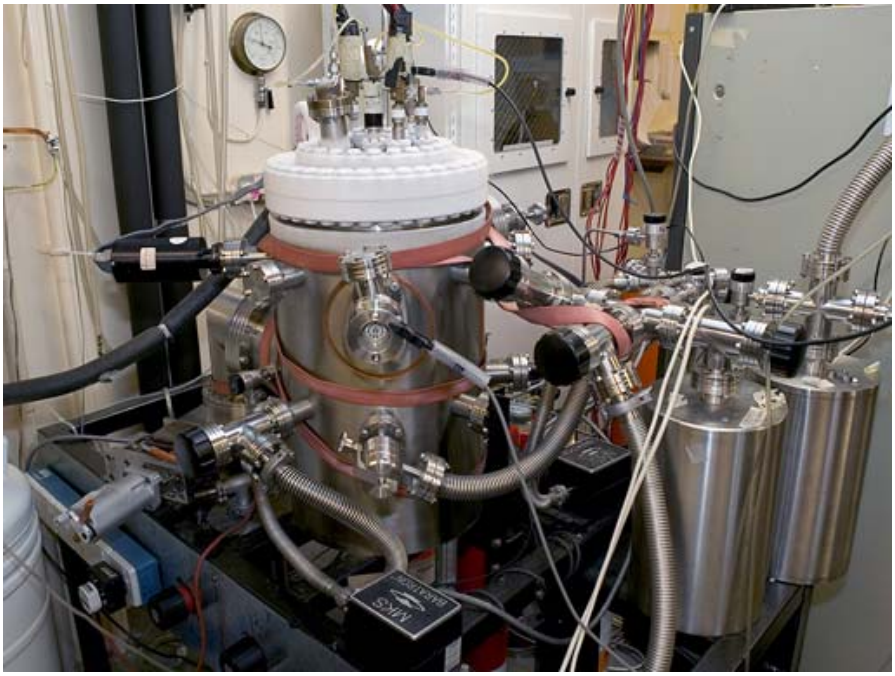

Fig. 3.4. Photograph of the MkVII sputtering system in use with the flange for depositing Co_2MnSi. The system has been cooled with liquid nitrogen for several hours.

Essentially, the MkIII and the MkVII sputtering systems operate in the same way. The MkVII has a turbo-molecular pump (backed by an Edwards 18 rotary pump).

The flange (Fig. 3.5) consists of 4 magnetrons, 3 of which are used to deposit the Heusler alloy and are arranged close together in a triangular geometry (Fig. 3.5b). The fourth magnetron was used to deposit the spacer layer for the spin valve devices and the protective capping layer (Chapter 9). The magnetrons are water cooled to minimise heating of the targets during sputtering. Anode shields are used for the target materials that do not have their own foil to surround the magnetron (Mn and Si). These prevent the target material being contaminated by the iron casing of the magnetron during the sputtering process. Stainless steel shielding is positioned between magnetrons to minimise cross-contamination of the sputter fluxes of the target materials. The heater consists of a uniform strip of Ta foil through which a constant dc current is passed via low resistance copper arms. For depositions on sapphire substrates, the Ta foil was 30 mm in width (18 mm for GaAs substrates to achieve higher temperatures) with corrugations in both directions to act as slots for the substrates (hence substrate dimensions were reduced to 4×4 mm^2 and 4×9 mm^2 to fit comfortably in the slots). The temperature of the heater was measured using an optical pyrometer by matching the colour of the filament with the colour of the heater. By measuring the temperature at the substrate surface, T_{sub} using a K-type thermocouple, it was found that the substrate temperature was about 180° lower than the heater temperature (for the temperature range used in this work).

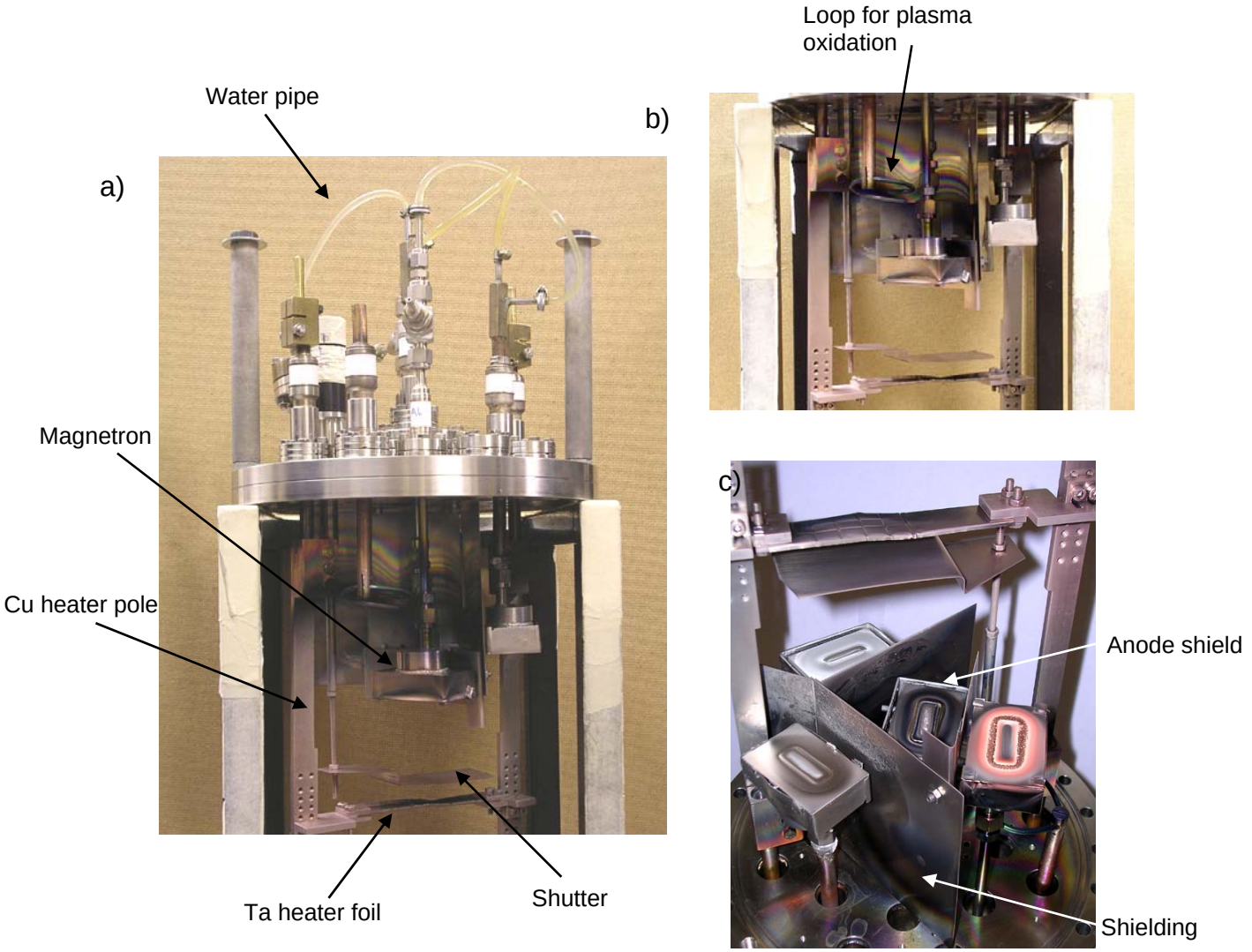

Fig. 3.5. Photographs of the flange for depositing Co_2MnSi. a) Side view of the whole flange, b) side view of the lower part of the flange and c) Plan view of the flange, showing the geometry of the targets relative to the heater.

3.2.3 Film thickness

The substrate shown in sector C4 of the substrate tray in Fig. 3.2 is a thickness monitor. A strip of Al foil (Ta foil is used when the temperature is >823 K since Al melts at 933 K) is placed across the substrate so no film deposition occurs there. A step is therefore formed and this was measured using a Dek-Tak profilometer. This is basically a stylus with a diamond tip that traverses across the step and the vertical downward movement of the tip at the step corresponds to the thickness of the film (accuracy is ±5 nm). In later work (chapter 9) thickness calibrations were carried out by defining a series of parallel lines of resist on the substrate by lithographic techniques prior to deposition (system bake-out could not be carried out in this case because photoresist degrades

above 423 K). Following lift-off the thickness was determined using the atomic force microscope (section 3.3.3). This is a more accurate method and film thickness can be determined to within 1 nm.

3.3 Film characterisation techniques

3.3.1 Scanning electron microscopy (SEM)

A schematic diagram of a SEM is provided in figure 3.6. The electron gun consists of a cathode (a filament made normally of W wire), which is heated to emit electrons by thermionic emission. The electrons are accelerated towards an anode with a potential difference of several tens of kV (the maximum voltage is typically 40 kV). A series of electromagnetic lenses focus the electron beam to a spot on the surface of the specimen. A variety of signals can be emitted as a result of interactions between the electron beam and the specimen. The beam is rastered over the surface of the specimen using electrostatic coils and the amplified signal collected by the chosen detector can be used to form a TV image. The signal from secondary electrons is the one most commonly used for imaging.

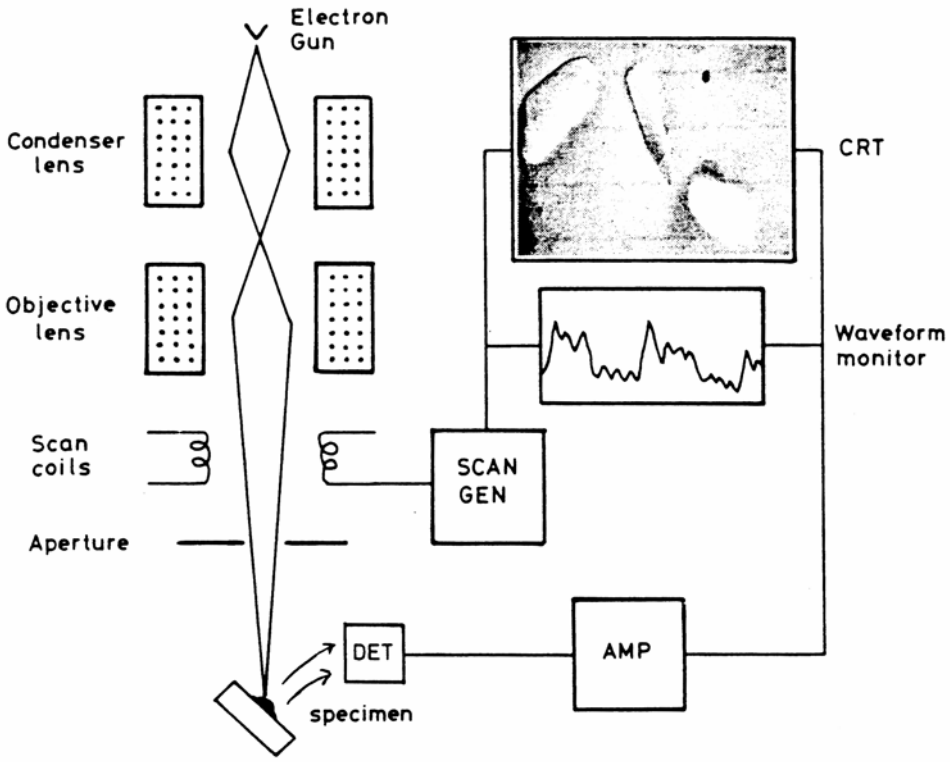

Fig. 3.6. A schematic diagram showing the main components of a SEM.

A field emission gun SEM (FEG-SEM) uses a strong electric field so that electrons tunnel out of the tungsten filament surface. High beam currents can be achieved in a small beam diameter so the resolution is greater than in a standard SEM. Therefore the FEG-SEM can be used to observe features that cannot be resolved by a standard SEM.

3.3.1.1 Energy dispersive x-ray spectroscopy (EDS)

The X-ray signal emitted from the specimen contains characteristic peaks whose energy can be related to an atomic transition and hence to a particular chemical species. There are two electron-beam specimen interactions to consider here. There is core scattering, which results in the emission of a continuous background and inner shell ionisation, which gives the characteristic peaks. We will just concentrate on the latter. The incident electron has sufficient energy to knock an inner shell electron out to the vacuum. An electron from a higher energy level falls down to the partially filled lower energy level and a photon is emitted. The energy of the photon corresponds to the difference between the two energy levels. Transitions are labelled as K, L or M, which is the energy level from which the electron was ejected and they are also given subscripts such as α, β, γ which indicates from which level the electron that fills the hole has come. The x-ray from the most probable transition is designated α. Therefore, a K_α x-ray is formed from a transition from the L shell to the K shell whereas a K_β x-ray results from a transition from the M shell to the K shell.

EDS is the X-ray detector system and is based on a p-i-n junction in silicon. An incoming X-ray generates a photoelectron, which leads to the generation of a number of electron-hole pairs. The number of pairs generated is proportional to the energy of the X-ray. The signal is amplified and is then sorted according to voltage amplitude by a multichannel analyser. Several thousand pulses per second can be processed and so a spectrum can be obtained in a short space of time. The current produced by the X-ray is small compared to the conductivity of the silicon and so the junction is reverse biased. The silicon is doped with Li to increase its resistivity and the detector is cooled to 77 K with liquid nitrogen to keep thermally activated conductivity and electronic noise to a minimum. There is normally a window on the outer surface of the detector, made of a polymer film (or Be) to prevent contamination from condensing on the cold detector. The limitation of this is that the window absorbs low energy X-rays, so low atomic weight elements cannot be detected (hydrogen to neon).[1]

In order to estimate the amount of an element present in a sample, the number of counts obtained in a fixed time interval, N_{spec}, can be compared with those from a standard of known composition, N_{std}. Therefore, the concentration of the element is given by

$$C_{spec} = \frac{N_{spec}}{N_{std}} C_{std} = kC_{std} \qquad (3.1)$$

However, if the specimen is not a pure element then the situation is more complex. Three correction factors must be applied and we will discuss each one in turn now. The atomic number correction (*Z*) accounts for the differences in the efficiency of X-ray generation. This depends on how far the electrons penetrate before they lose too much energy to excite X-rays and how many electrons are backscattered without exciting X-rays. The absorption correction (*A*) accounts for the differences in the mass absorption coefficients of the elements involved. Finally, the fluorescence correction (*F*) is necessary if element Y emits characteristic X-rays of energies greater than the energy for excitation of characteristic X-rays from element Z. It is a very inefficient process but can be significant if elements have a similar atomic mass. These corrections are known as *ZAF* corrections. To determine these factors, the sample-detector geometry must be known accurately and the sample must be flat. If this is the case then errors can be as low as ±3 %. Equation 4.5 can now be modified to include the *ZAF* corrections.

$$C_{spec} = kk_z k_A k_F C_{std} \qquad (3.2)$$

k_z, k_A and k_F require some knowledge of the specimen composition so the process is iterative. Normally, only three or four iterations are needed.

For the quantitative analysis, standardless analysis was used, which is the simplest of the correction procedures and does not rely on obtaining good quality bulk standards. Only the correct beam energy and the elements to be analysed need to be supplied and the analysis total will always be exactly 100 %. There are a few limitations with EDS for measuring thin film samples but once one is aware of these, it can be an accurate method of determining film composition. The first is that the effective probe depth of the incident electrons is about 1 μm. However, the computer program that carries out the analysis assumes that the sample is homogeneous, which is not the case since the thin film is on a substrate. Monte-Carlo simulations were carried out on Co films of different thickness on silicon substrates at different accelerating voltages and a selection of these are shown in Fig. 3.7. These simulations merely model the electron trajectories. The penetration of the electrons in the actual Sm-Co films will be less, since I have neglected the heavier Sm component in the modelling. However, one can see that by depositing a thick film and using a low accelerating voltage, all interactions take place within the film. This was actually tested in practice, by depositing films of different thickness and carrying out composition analyses at different accelerating voltages: similar results were found. However, to confine the interactions to

within the film volume means using lower energy X-ray lines (i.e. L and M) for the composition analysis.

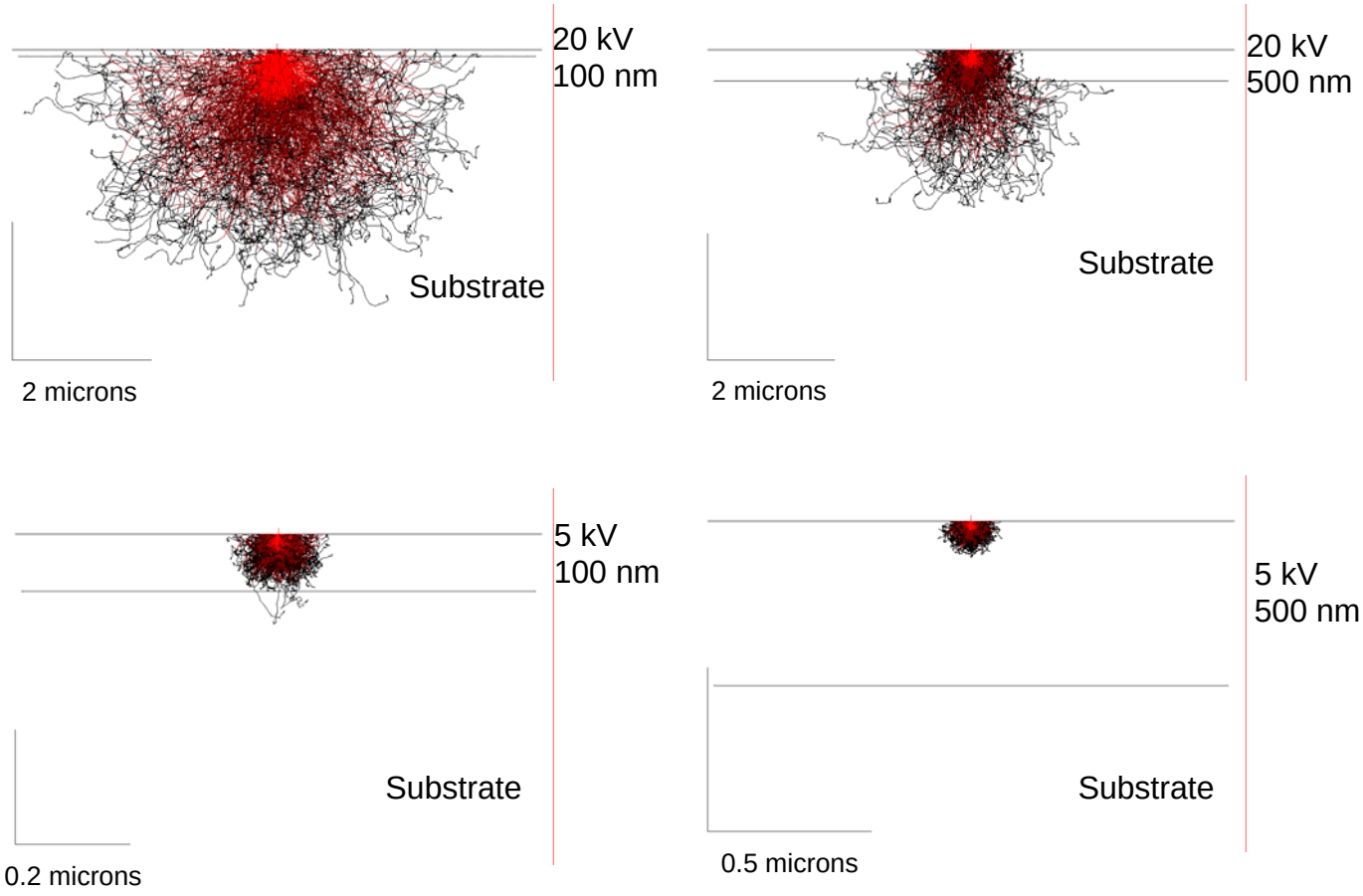

Fig. 3.7. Monte-Carlo simulations for cobalt films on silicon substrates. The red trajectories denote backscattered electrons.

The correction factors in this energy region are not well known and interfamily calculations (e.g. between K and L lines) are particularly difficult. For alloys where it is only possible to analyse lines from different families, it has been found that errors can be as high as 20 % relative, whereas results obtained with *ZAF* correction relative to standards gave errors of 1-2 % relative.[1] Therefore, it is important that the K lines are used for the quantification. Although this means that a large amount of the interaction volume will be within the substrate, in practice it has been found that accurate composition analysis can be attained. The estimated relative error is 1.5 % (includes the error that the software gives for the *ZAF* corrections). For the Heusler alloy, Co_2MnSi the K lines could be used in the analysis and an accelerating voltage of 15 kV was used. However, for the case of Sm-Co, the K line of Sm is too high for electrons to be excited at the accelerating voltages that can be applied in the SEM and so the L line of the Sm and the K line of Co is used

(accelerating voltage is 15 kV). Since we know that interfamily calculations are inaccurate, a bulk standard of $SmCo_5$ was employed as a calibration.

3.3.1.2 Sample preparation

Samples were mounted onto Al stubs (12 mm in diameter) using silver paint. Since the substrates were insulating, it was necessary to apply a small amount of silver paint to connect the film, substrate and stub. By placing two samples on each stub it was possible to analyse twelve samples without breaking vacuum. The paint was left to dry for one hour before placing the stubs in the SEM, as outgassing of the solvent would prevent the required high vacuum condition from being attained.

3.3.2 X-Ray Diffraction (XRD)

This is a very widely used characterisation technique as it provides a lot of information about the structure of the film. One can determine if there is any texturing, the degree of crystallinity, lattice parameters, the size of crystallites, if the expected phases are present etc. It is a non-destructive technique and the sample preparation is minimal. However, the large penetration depth of X-rays means that their path length through the film is too short to produce diffracted beams of sufficient intensity and the substrate tends to dominate the signal. Therefore, long counting times are required and the sample should be as large as possible. For XRD work a thick film would be grown on 10×5 mm substrates where possible. The details of XRD are discussed below.

Figure 3.8 shows the geometry of diffraction from a series of (001) lattice planes. The incident beam penetrates the lattice and scatters from each of the atoms in the 3D lattice. When the angles of the incident and diffracted beams are equal, (as measured from atoms in the (001) planes in this case), the path lengths of rays scattered off any of the atoms in that plane will be the same. These rays constructively interfere resulting in a plane wavefront, which can be considered as having been specularly reflected from the (001) planes. The wave vectors of the incident and 'reflected' beams are denoted by $\mathbf{k}_0$ and $\mathbf{k}_1$ respectively. The distance between successive (001) planes is known as the d-spacing, d. Therefore, by simple trigonometry the path difference between beams 'reflected' from successive planes in the z direction is simply given by $2d\sin\theta$. For constructive interference, the path difference must be an integral multiple of wavelengths, and so we find that

$$2d\sin\theta = n\lambda \qquad (3.3)$$

This is known as the Bragg equation and when this condition is satisfied a diffraction maximum will be observed.

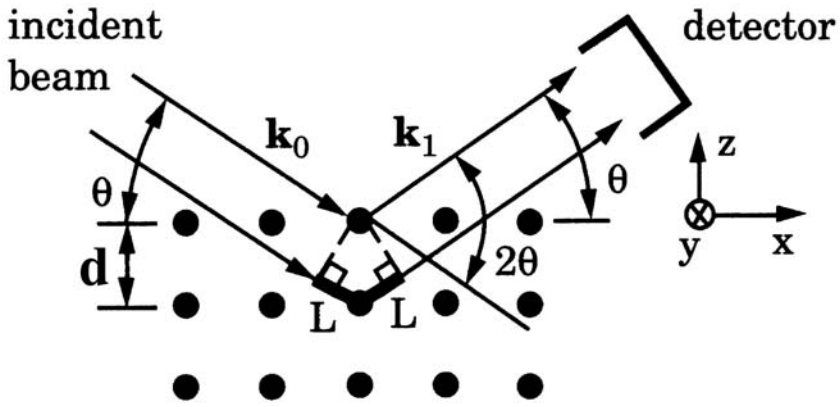

Fig. 3.8. Geometry of X-ray diffraction from a series of (001) planes.

For XRD characterisation of polycrystalline thin films, monochromatic X-rays and a Bragg-Brentano geometry are normally employed. The thin film surface is oriented as shown in Fig. 3.9 so that the film normal bisects the angle made between the source, the centre of the film and the detector. θ is scanned by rotating the sample about the y-axis, whilst the detector is moved through 2θ to keep it at the specular angle with respect to the film surface. At values of 2θ for which the atomic periodicity, *d* perpendicular to the film surface satisfies the Bragg condition for the λ being used, a peak appears. This is how the diffraction pattern is built up and from the relative intensity of the peaks, the degree of texturing can be determined.

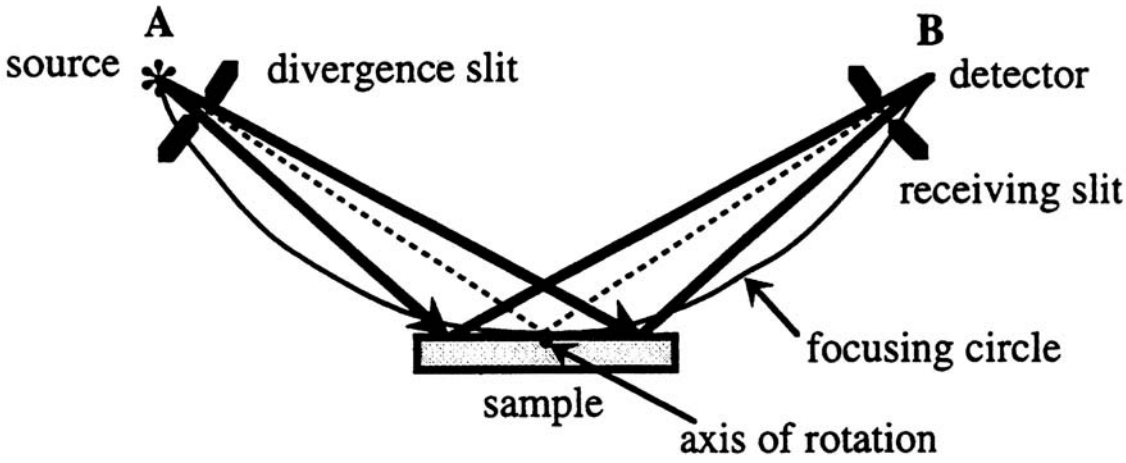

Fig. 3.9. Bragg-Brentano geometry.

The shape of an X-ray diffraction line can contain information about particle size (strictly the size of the coherently diffracting regions in the direction perpendicular to the reflecting planes) and about inhomogeneous variations in interplanar spacing arising from either residual stresses in the material or variations in composition from point to point in the material. In this work, peaks were

fitted using the PROFIT software developed by Langford *et al*.[2] By means of a Pseudo-Voigt function the peaks were deconvoluted into a Gaussian and a Lorentzian part, depending on the ratio of the full width at half maximum (FWHM) to the integral breadth, β.[3] β is similar to the FWHM but is the width of a rectangle that has the same area and height as the observed peak. β must be corrected for instrumental broadening. This can be done by carrying out a scan on a substrate with a sharp peak, such as single crystal silicon. This β_{inst} can then be subtracted from β_{film} but the way in which this subtraction is carried out depends on the profile of the peak. If the peak is Gaussian then,

$$\beta_{corr}^2 = \beta_{film}^2 - \beta_{inst}^2 \tag{3.4}$$

If the peak is Lorentzian then,

$$\beta_{corr} = \beta_{film} - \beta_{inst} \tag{3.5}$$

The size of the particles, t can then be determined using the Scherrer equation,[4]

$$t = \frac{0.9\lambda}{\beta_{corr}\cos\theta} \tag{3.6}$$

and the strain, ε is given by

$$\varepsilon_{rms} = \partial 2\theta = -\frac{\beta_{corr}}{4\tan\theta} \tag{3.7}$$

The size and strain of the crystallites can also be determined by plotting $\beta\cos\theta$ vs $\sin\theta$, known as the Williamson-Hall plot,[2]

$$\beta\cos\theta = \frac{k_1\lambda}{t} + k_2\varepsilon_{rms}\sin\theta \tag{3.8}$$

where k_1 and k_2 are constants, the intercept gives the size and the slope gives the strain.

So far, we have considered wide angle scans, where the sample can be moved through angles such as 15°2θ to 100°2θ. However, a lot of information can also be gained from low angle scans and an example of a low angle scan is shown in Fig. 3.10. θ_c is the critical angle for which total external reflection at the film surface no longer occurs, X-rays penetrate deeper into the film, and the intensity drops off rapidly. The slope of this portion indicates the roughness of the film. At angle greater than θ_c, interference of specular reflections from the substrate/film interface and the

film surface occurs and this results in a fringe pattern known as Kiessig fringes.[5] The closer the fringes, the thicker the film and the film thickness can be calculated from the 2θ values of consecutive peaks,

$$\sin^2\theta_m - \sin^2\theta_{m-1} = \left(\frac{\lambda}{2t}\right)^2 \qquad (3.9)$$

and so from the slope of a plot of ($\sin^2\theta_m$ - $\sin^2\theta_{m-1}$) vs. *m*, the film thickness can be determined.

There is then a series of Bragg peaks, which correspond to the period of the bilayer. The bilayer thickness can then be determined.

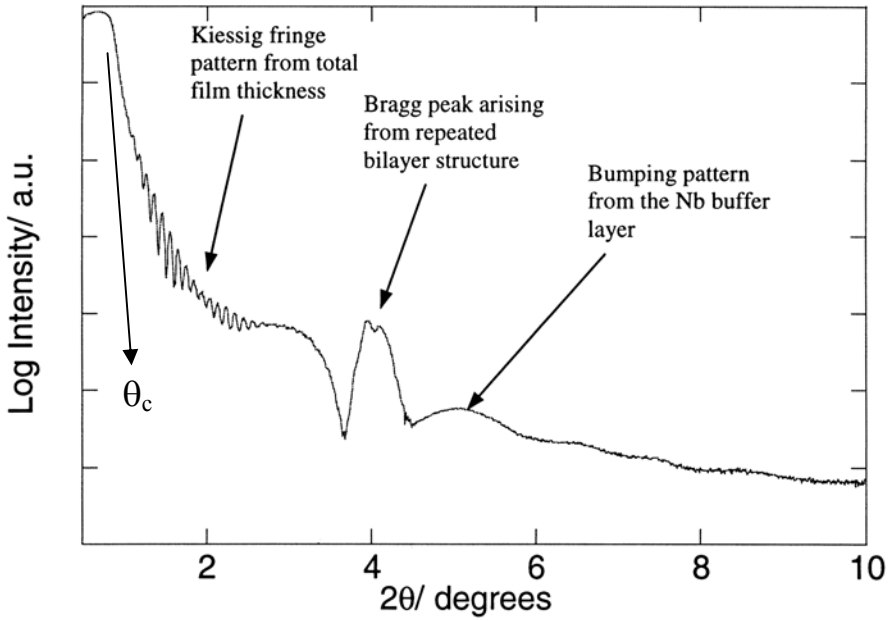

Fig. 3.10. Low angle XRD scan for a GMR bilayer with structure Nb(4.5 nm)/[Cu(0.9 nm)/Co(1.3 nm)]$_{30}$.[6]

All X-ray scans carried out in this work were done using a Philips X'pert PW3020 diffractometer in Bragg-Brentano geometry. CuK_α radiation (λ=1.54056 Å) was generated using a sealed copper tube (PW 1730 X-ray generator) with a tube current of 40 mA and a tube voltage of 40 kV. The divergence, receiving and anti-scatter slits were 1/2°, 0.2 mm and 1/2° respectively and a 10 mm mask was used. For the low angle scans smaller slits were used (1/12°, 0.1 mm and 1/12°). A 12×12 mm piece of silicon single crystal was mounted on an aluminium sample holder using a small amount of plasticene. The sample was then mounted onto the silicon single crystal. The single crystal does not produce any peaks in the range that is scanned, so all peaks must come from the film or the substrate. It was ensured that there was no plasticene visible to the X-rays because it does produce a peak. It was important that the sample was level with the sample holder so that

the film surface is coincident with the axis of rotation of the goniometer. Any displacement by distance, *D* of the sample surface from the center of the diffractometer (radius *R*) will cause an error in the measurement of 2θ. This error can be expressed as,[7]

$$\partial(2\theta) = 2D(\cos\theta)/R \qquad (3.10)$$

A nickel filter was employed whenever a substrate with an intense substrate peak was used, since a large number of counts can damage the X-ray detector. All data was collected using Philips X'Pert software and profile fitting was carried out using Philips PROFIT software.

3.3.3 Atomic Force Microscopy (AFM)

This is a widely used technique to investigate the surface microstructure and quantify surface topography. A stylus (supported by a cantilever) is scanned across the surface in a raster pattern using piezoelectric actuators. As the stylus is scanned across the surface, the magnitude of the force experienced by it will depend on the distance between the stylus and the surface atoms. A feedback mechanism detects the changes in force (or deflection of the stylus) and a proportional voltage is applied to a *z* piezoelectric control. This moves the stylus in the *z* direction so that a constant distance is maintained between the stylus and the surface. The variation in voltage during a scan is then translated electronically into an image of the surface. The vertical deflection of the cantilever can be measured directly as it is dragged across the sample surface, and this is known as contact mode. However, tapping mode is more commonly used because the surface is not damaged. The stylus oscillates into and out of contact with the surface. Contact of the oscillating stylus with the surface is detected by the accompanying drop in cantilever resonant frequency.

For this work a Digital Instruments Nanoscope III Scanning probe microscope was used in tapping mode with a Si_3N_4 tip (radius is 0.1 μm). The 3D information collected is displayed as a topographic image, where different heights are indicated using a grey scale. Cross-sections through the surface can be taken, and the distribution of heights can be clearly seen and measured to within 0.1 nm. The software was used to determine the root mean square (RMS) surface roughness, of areas that had been first order plane fit flattened. Since this is an indirect imaging technique, there are various artefacts that may be present and could be interpreted as surface features. Therefore it is always a good idea to confirm observations with another imaging technique. In this case FEG-SEM was used.

3.3.4 Vibrating Sample Magnetometer (VSM)

The VSM (Princeton measurements corporation, MicroMag™ 2900) is essentially a gradiometer, measuring the difference in magnetic induction between a region of space with and without the specimen. A schematic diagram of a VSM is shown in figure 3.11. The sample (S) is mounted on a small plastic cylinder using some silicone grease and is attached to a glass rod, which is then placed in the VSM. The sample is centrally located between four, stationary pick-up coils and oscillated vertically in a uniform magnetic field (sample is driven by a loudspeaker mechanism). At the upper end of the glass rod there is a reference in the form of a small permanent magnet (M) situated between a set of reference coils. Therefore the AC signal induced in the pick-up coils by the magnetic field of the sample is compared with the signal from the permanent magnet and is converted to a number proportional to the magnetic moment. This means that the set-up is insensitive to changes in the vibration amplitude and frequency.

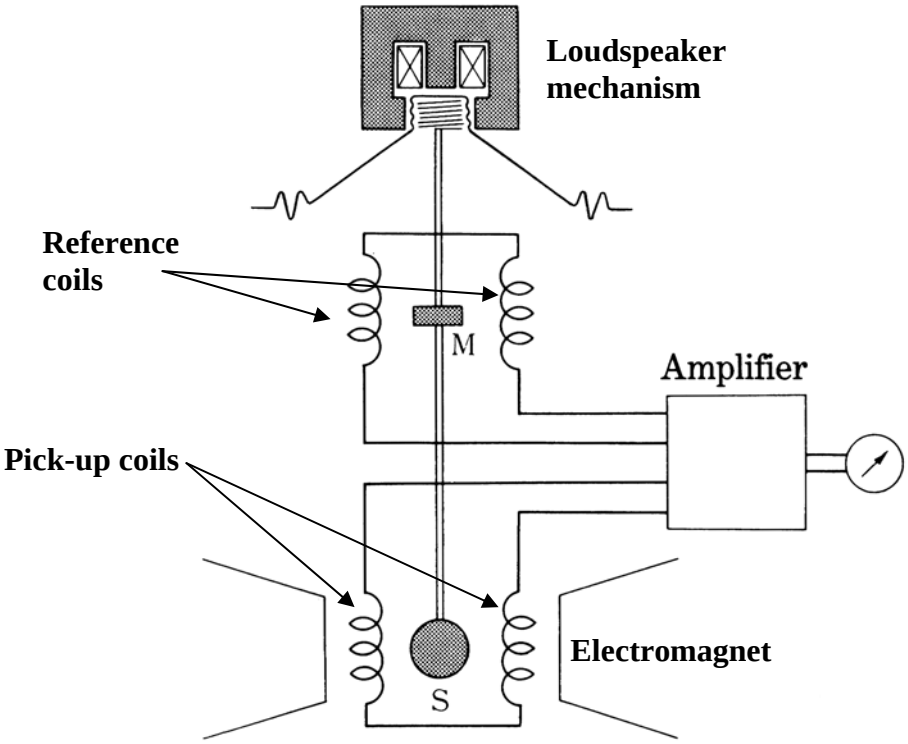

Fig. 3.11. A schematic diagram of a VSM (adapted from [8]).

The VSM has a high sensitivity and is capable of measuring magnetic moments in the range of μemu. Its accuracy is better than 2 %. However, the specimens used have to be rather short to fit between the pole pieces of the electromagnet and so the hysteresis loops obtained are not intrinsic because of demagnetising effects associated with using short specimens. For quantitative work, the VSM was calibrated with a bulk sample of Ni of known saturation magnetisation. This sample

was small enough to assume that all flux produced will cut the sense coils. However, thin film samples are normally grown on 10×5 mm^2 substrates and so in certain orientations not all of the magnetic flux from these larger samples will cut the sense coils. From a study carried out on this VSM it was found that the same M_s was obtained for a 2×2 mm^2 sample as for a 10×5 mm^2 (long axis parallel to applied field) but a reduction in M_s of 23 % was found when the short axis of the 10×5 mm^2 was parallel to the applied field. Therefore, in general 5×5 mm^2 samples were used for VSM work and for the case of measurements down to 10 K (using a ^{4}He cryostat) 4×4 mm^2 were used so that the sample could be rotated in the glass capillary.

3.3.5 Transport measurements

3.3.5.1 R-T measurements

This was carried out using a standard dc 4-point geometry using a constant current supply and standard digital voltmeters. Contact was made to the film via spring-loaded pins, and the pins used for the measurement were always located in the corners of the film. The resistance was measured down to 4.2 K by inserting the probe into a liquid He dewar.

3.3.5.2 Magnetoresistance (MR) measurements

Resistance measurements as a function of applied field were carried out by the four-point probe geometry using a water cooled electromagnet system. It was possible to apply an in-plane field of up to 500 mT and the system could be cooled to 4.2 K using a continuous flow cryostat. This was used to characterise the spin valve devices (chapter 9) and the normalised MR ratio was defined as,

$$\frac{R - R_{\max}}{R_{\max}} \times 100\% \qquad (3.11)$$

References

[1] J. I. Goldstein, D. E. Newbury, P. Echlin, D. C. Joy, A. D. Romig, C. E. Lyman, C. Fiori, and E. Lifshin, *Scanning Electron Microscopy and X-ray Microanalysis*, 2nd ed. (Plenum Press, 1992).

[2] J. I. Langford and D. Louer, Powder Diffraction **1**, 211 (1986).

[3] T. H. Dekeijser, J. I. Langford, E. J. Mittemeijer, and A. B. P. Vogels, J. Appl. cryst. **15**, 308 (1982).

[4] B.D. Cullity, *Elements of X-ray diffraction*. (Addison-Wesley, 1978).

[5] H. Kiessig, Ann. Phys. **10**, 769 (1931).

[6] C. W. Leung, PhD thesis, University of Cambridge, 2002.

[7] J. A. Leake, *Techniques of Materials Reserch*, (University of Cambridge, 1997).

[8] S. Chikazumi, *Physics of Ferromagnetism*, 2 ed. (Oxford Science Publications, 1997).

"Words are, of course, the most powerful drug used by mankind."
Rudyard Kipling.

Chapter 4

Sm-Co thin films: high coercivity medium

In this chapter the applications of Sm-Co thin films are outlined. In particular the growth and optimisation of the intermetallic $SmCo_5$ is reviewed.

4.1 Introduction

It is possible to achieve exceedingly high longitudinal magnetic recording densities if improvements in magnetic heads and media can be made. However, at high areal recording densities the bit length becomes shorter and a high H_c medium is needed in order to support a narrower transition width (i.e. the distance over which a magnetic reversal occurs).[1] Although a high H_c is essential, it is not sufficient to obtain a high signal to noise ratio. Micromagnetic modelling studies of magnetisation structures in thin film metal media indicate that exchange and magnetostatic coupling among grains must be reduced in order to obtain sharp, low noise transition boundaries.[2,3] Since media noise in thin films is attributed to exchange coupling and to inhomogeneities in the medium, thin films with very small magnetically non-interacting grains are required.[4] In order to achieve both high H_c and small isolated grains simultaneously, a material with a very high magnetic anisotropy is required. Sm-Co alloys exhibit high magnetic anisotropy in both the amorphous and crystalline state,[5,6] and therefore it may be easier to prepare thin Sm-Co films with high in-plane coercivities than is possible with simple transition metal Co-based alloys.

Amorphous Sm-Co thin films prepared by evaporation and sputtering were studied in the mid 1980's, but coercivities less than 700 Oe were achieved.[7,8] However, Velu and Lambeth renewed interest in these films in the early 1990's, obtaining coercivities of up to 3000 Oe by using a Cr underlayer.[9,10] An underlayer of polycrystalline Cr has been used in other Co-based alloys such as CoCrTa,[11] and CoNiPt.[12] The underlayer increases H_c by controlling the grain size and morphology of the magnetic layer. It provides an appropriate crystallographic texture that improves the in-plane magnetisation and produces a magnetically isolated or voided microstructure (i.e. a structure with low density boundaries between magnetic islands), which reduces the media noise. Amorphous Sm-Co films are magnetically softer than crystalline films[5] and so Sm-Co is grown on an underlayer of Cr to induce microcrystallinity into the film. There is a very close lattice match between the $SmCo_5$ $(11\bar{2}0)$ and Cr (110) atomic planes. All the Sm-Co films discussed in this section were found to be in the X-ray amorphous state (i.e. no crystalline peaks were detected by XRD) and were deposited at room temperature.

4.2 The effect of composition and microstructure of the Sm-Co layer on the coercivity

The films discussed in this review have been fabricated by dc magnetron or RF sputtering. The sputtering parameters along with the magnetic properties are summarised in table 4.1 at the end of this chapter. It is difficult to compare findings since not all the deposition parameters are

provided. None of the authors have used a combination of single element targets, even though some investigated a range of film compositions. Alloy targets are used, and the composition is varied by placing small plates of Sm or Co onto the target. Sometimes a mosaic target is used, where pieces of Sm are attached to a cobalt target. These methods do not allow as good a control of the composition compared to using several, single element targets.

Okumura *et al.*[13,14] were the only authors who investigated the effect of the composition of the films on the magnetic properties (Fig. 4.1). The films were deposited by RF sputtering onto glass substrates, using an alloy target. The thickness of the Sm-Co and Cr layer were 50 and 100 nm respectively. The coercivity values for the films with and without an underlayer showed similar composition dependencies. It was found that for both types of films, the maximum H_c was obtained at a Sm content of 15 at. % ($SmCo_{5.7}$).

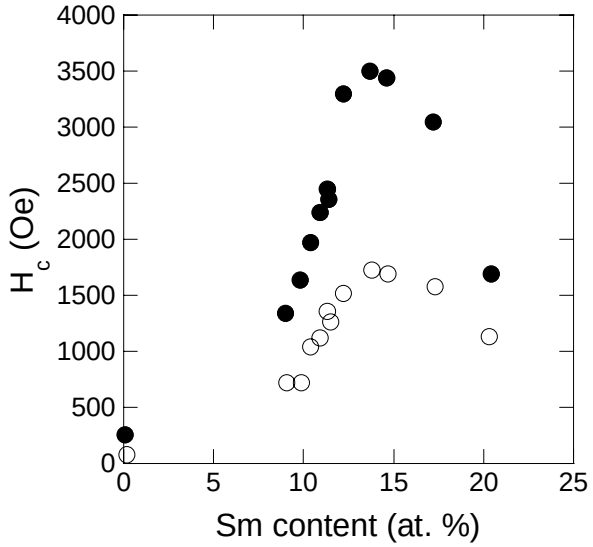

Fig. 4.1. Dependence of H_c on the composition of Sm-Co thin films.[14] Filled circles represent films with a Cr underlayer and open circles are for films without an underlayer.

These films contain about 1.7 at. % less Sm than the intermetallic compound $SmCo_5$, which shows the importance in studying off-stoichiometric compounds. The maximum coercivities obtained were 3500 and 1500 Oe for the $SmCo_{5.7}$ films, with and without the underlayer respectively. They compare their results to those of Gronau *et al.*,[15] who prepared Sm-Co/Cr films on glass substrates by flash evaporation and found that the maximum H_c occurred at a Sm content of 25 at. %. This is 10 at. % more than the composition obtained by Okumura *et al*. The saturation magnetic moment, M_s was also studied by Okumura *et al.* and was found to decrease monotonically with increasing Sm content. The values of M_s were about 10 % smaller than those obtained by Gronau *et al*., and the coercivity values were larger. Therefore, the preparation method of the films affects the

magnetic properties of Sm-Co and this is probably due to a difference in the microstructure of these films. It is surprising that later authors have not used these findings, since most of them have deposited $SmCo_4$ films and have probably obtained lower coercivities as a result.

Okumura *et al.* also carried out a detailed transmission electron microscopy (TEM) study of their films. In the case of Sm-Co films without an underlayer, TEM revealed that there were some crystallised clusters of 4-8 nm in diameter within an amorphous matrix. This was also observed in Sm-Co films with an underlayer of Cr. However, in addition it was found that columns of the Sm-Co layer grow on columns of Cr and crystallised boundaries separate the amorphous, columnar regions. EDS analysis showed that the ratio of Sm:Co inside the amorphous-like regions was smaller than in the crystallised boundary regions. The higher concentration of Sm in the boundary regions is thought to play an important role in increasing the pinning forces of magnetic domain walls. A wall-pinning model was used by Yang *et al.*[16] to explain H_c in amorphous RE-TM alloys. Pinning sites were considered to arise from fluctuations in the local anisotropy caused by local inhomogeneities in short-range ordering and composition. However, this model does not explain the difference in the values of H_c obtained for films with and without the underlayer. There must be an additional mechanism for the coercivity and the most likely is that the net-like structures provide another source of wall-pinning. This is supported by observations of a 'shoulder' in the hysteresis loop of films with an underlayer (Fig. 4.2). No shoulder was observed for films without the underlayer, which suggests that the shoulder results from domain wall pinning due to the net-like microstructure.

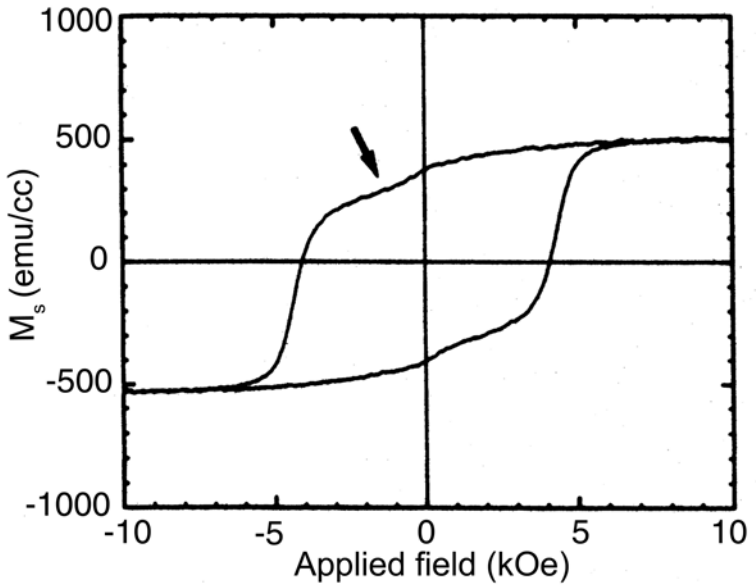

Fig. 4.2. Hysteresis loop of a $SmCo_{5.7}$ film with a Cr underlayer.[14]

Liu *et al.*[17,18] also carried out detailed TEM work on $SmCo_4$/Cr/glass films. They fabricated films by dc magnetron sputtering and the Cr underlayer was a constant thickness of 95 nm. Their findings were very similar to Okumura *et al.* except that they did not report on any crystalline boundaries. TEM work indicated that a large portion of the grain boundaries have gaps (inherited from the underlayer) and they found that the width of the gaps was about 1-3 nm and varied from place to place. The grain size of the Cr underlayer was about 25 nm and since the Sm-Co layer inherits the structure of the underlayer it also had a grain size of 25 nm. Fig. 4.3 schematically illustrates the growth process of the Cr grains and subsequent growth of the Sm-Co layer. The lattice constant of the Cr crystallites was a = 2.89 Å. As the sputtering gas pressure was increased, the grain boundary gaps of the Cr underlayer (and hence the Sm-Co layer) increased. These gaps may weaken the interaction between different grains and therefore reduce the noise when used as a magnetic recording medium. Liu *et al*. also made the important point that the grains observed were not direct evidence of magnetic grains, so one must be careful to make this distinction. They found that as the thickness of the Sm-Co layer was increased the gaps became smaller, or at least the grain-like contrast from bright field images becomes weaker and at a thickness of 96 nm there is no contrast. This indicates that the gaps are sealed at places far from the Cr underlayer.

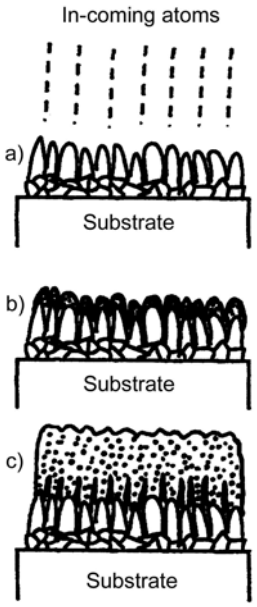

Fig. 4.3. a) Schematic illustration of the formation of grain boundary gaps in the Cr underlayer, b) morphology of Sm-Co films of 24 nm or less, c) morphology of Sm-Co films of 96 nm or more.[17]

Liu *et al.* also carried out detailed TEM studies on the structure of the crystallites in the Sm-Co films deposited on Cr underlayers. They claimed that the volume fraction of the crystallites (about 5 nm in diameter) in the amorphous phase was about 91 %. The lattice constants were a = 2.53 Å

and c = 4.13 Å. The crystallites had a close-packed structure, consisting of a random stacking sequence with local special stacking modes present. The Sm atoms were found to be randomly distributed in the Co lattice. It needs to be determined if this is the case for all the sputtered Sm-Co films in the literature before one can determine mechanisms for the magnetic properties that have been measured. In general, different sputtering processes have different dynamics for the formation of the nanostructure and so it is important to identify the structure of the crystallites.

In all the literature, the authors talk about lattice matching of the Cr (110) and the $SmCo_5$ $(11\bar{2}0)$ atomic planes, but in light of the microstructure revealed by the TEM work it is not clear how this lattice matching occurs. Since only the nanocrystallites can be lattice matched and they are distributed discontinuously in the amorphous matrix, it seems unlikely that there can be any overall lattice matching.

4.3 Optimisation of the Sm-Co layer

Unfortunately not all authors optimise films of the same composition, even though films based on the intermetallic compound $SmCo_5$ give the maximum H_c. Also, not all the deposition parameters are provided, so it is difficult to compare results. However, with this in mind a rough comparison is made in this section.

Velu and Lambeth[9] investigated $SmCo_4$/Cr/glass films made by RF diode sputtering using a mosaic target. They optimised the deposition parameters (table 4.1), and found that H_c increased with decreasing thickness of the Sm-Co layer, and reached a value of 2410 Oe at a film thickness of 14 nm.

Takei *et al.*[19] also investigated $SmCo_4$/Cr/glass films made by dc magnetron sputtering but did not optimise all the deposition parameters. They kept the Cr underlayer at a constant thickness of 100 nm and varied the thickness of the Sm-Co layer from 1-400 nm. H_c showed a maximum of about 3300 Oe at a thickness of 40 nm. This contradicts the findings of Velu and Lambeth,[9] since they did not obtain a maximum H_c, and the coercivity still increased at thicknesses below 14 nm. The grain diameter of the Sm-Co layer was determined using AFM. The grain diameter of a SmCo/Cr film with the Sm-Co layer thinner than 100 nm was about 50 nm which was almost the same as that of the Cr underlayer. This is expected since the Sm-Co layer inherits the structure of the Cr underlayer, as discussed above. The surface roughness of the films tends to increase slightly with increasing film thickness but is about 6 nm for Sm-Co films thinner than 100 nm. The roughness of the Cr underlayer was 5.8 nm.

4.4 Optimisation of the underlayer

4.4.1 Cr underlayers

Most of the research effort seems to be dedicated to optimising the underlayer. Velu and Lambeth[9] fixed the forward power of the Cr underlayer at 100 W and varied the argon pressure, sputtering time and substrate temperature. The optimised deposition parameters for the Sm-Co layer were used, as described in the table, and the film thickness was 45 nm. The maximum H_c was obtained for an underlayer thickness of 110 nm deposited at 1.3 Pa at room temperature (deposition rate, 11 nm/min). At this pressure, H_c remained constant at underlayer thicknesses above 100 nm. H_c decreased with increasing substrate temperature at an argon pressure of 1.3 Pa, although H_c only decreased slightly at temperatures below 373 K. The observed drop in H_c at T_{sub}>373 K may be due to a texture change of the Cr underlayer from [110] to [200], although this normally occurs at temperatures greater than 573 K.

Okumura *et al.*[13] looked at $SmCo_{5.7}$/Cr/glass films deposited in an RF sputtering system. The sputtering Ar pressure was kept constant for the Sm-Co layer but the pressure was varied from 0.67-4.0 Pa for the Cr underlayer. H_c reached a maximum of 3600 Oe at 2.7 Pa.

Takei *et al.*[20] followed on from their previous work on optimising the magnetic layer of $SmCo_4$/Cr/glass films to optimising the underlayer. The underlayer thickness was varied from 10-1000 nm and all the films had a [110] texture, and the lattice parameter was 2.86-2.88 Å. When the layer thickness was 100 nm, the grain size of the Cr underlayer was about 25 nm, which is half the value that was reported in their previous work,[17] suggesting that some of the deposition parameters may have been changed. The average Cr grain size increased with increasing underlayer thickness, as did the roughness of the films. The roughness of a film with a 100 nm Cr underlayer was about 1.4 nm, whereas it was 2.2 nm when the underlayer was 200 nm in thickness. H_c reached a maximum of 3300 Oe at an underlayer thickness of 200 nm. This disagrees with the findings of Velu and Lambeth, who found that H_c remained fairly constant at underlayer thickness above 100 nm.

X.H. Liu *et al.*[21] fabricated $SmCo_{3.5}$(44 nm)/Cr(126 nm)/glass films using a multiple-gun dc magnetron sputtering system. The substrates were water-cooled and the target consisted of a cobalt disk and small Sm chips. Cr underlayers were deposited at two different pressures. They both had the Cr (110) peak of the bcc structure, indicating that the Cr underlayer is highly textured. However, the underlayer deposited at the lower pressure had a (200) peak as well. The underlayer deposited at the higher sputtering pressure had the higher H_c of 4200 Oe.

4.4.2 Other underlayers

Alloying Co with large atoms such as Sm changes its lattice spacing, so a pure Cr underlayer is not the best candidate for the optimum epitaxial match. This could be solved by alloying Cr with larger atoms such as W, V, and Mo which would not alter the basic Cr bcc structure. The desired lattice parameter can be achieved by increasing the percentage of X in the alloy. It was Howard *et al.* who initiated adjusting the lattice parameter of the underlayer in order to improve the coercivity.[22]

As well as Cr underlayers, Okumura *et al.* also looked at Ti, V and Cu underlayers in the work described in the previous section. H_c increased with sputtering pressure as before for the Ti, V and Cu underlayers, but no maximum was observed. The highest values obtained for a sputtering pressure of 4 Pa was 2600 Oe for Ti, 2200 Oe for V and 1800 Oe for Cu. The microstructure of these films (in cross-section) was observed using TEM. The columnar structure could not be seen clearly in the case of the V underlayer and even less so for the Cu underlayer. This explains the lower coercivity values obtained with these underlayers.

In the work by Takei *et al.*,[20] described in the previous section, they also studied Mo, Al, W and W/Cr underlayers. It was found that the H_c of the films with W, W/Cr, and Al underlayers was lower than 3000 Oe, but with a Mo underlayer H_c was higher than 3000 Oe when the underlayer thickness was greater than 100 nm. At an underlayer thickness of 200 nm H_c of the film with the Mo underlayer reached a maximum H_c of 4000 Oe, which was higher than the value obtained for the film with the Cr underlayer. Therefore, a Mo underlayer may be better than a Cr underlayer at increasing the coercivity of the magnetic layer.

Author	Sputtering Method	Film structure	Deposition Parameters	Maximum H_c (Oe)
Velu and Lambeth[9]	RF-diode	$SmCo_4$(14 nm)/Cr(110 nm)/glass	Sm-Co: 50 W (RF), 2.7 Pa, 9 nm/min. Cr: 100 W, 1.3 Pa, 11 nm/min	2410
Okumura *et al.*[14]	RF	$SmCo_{5.7}$(50 nm)/Cr (100 nm)/glass	Sm-Co: 4.7 Pa Cr: 2.7 Pa	3500
Takei *et al.*[19]	DC magnetron	$SmCo_4$(40 nm)/Cr(100 nm)/glass	Sm-Co: 34W, 1.1 Pa Cr: 57W, 0.27 Pa.	3300
Takei *et al.*[20]	DC magnetron	$SmCo_4$(40 nm)/Mo(200 nm)/glass	Sm-Co: 34 W, 1.1 Pa Mo: 57 W, 0.27 Pa	4000
Liu *et al.*[21]	DC magnetron	$SmCo_{3.5}$(44 nm)/Cr(126 nm)/glass	Sm-Co: 0.60 Pa, 6.6 nm/min, 150 mm target-substrate distance Cr: 0.40 Pa, 10.8 nm/min	4200

Table 4.1. Summary of results from the literature.

4.5 Summary

Sm-Co thin films are good potential candidates for high density recording media. The highest coercivity films were grown on Cr underlayers at room temperature. The Cr underlayer has two possible effects. The first is that there is an epitaxial relationship between the Cr and the Sm-Co film, encouraging the c-axis of the Sm-Co layer to lie in the plane of the film, although it is not clear how this occurs. The second is that the morphology of the Cr underlayer influences the structure of the Sm-Co: columns of Sm-Co growing on top of columns of Cr with low density boundaries, resulting in the desired isolation of 'magnetic grains.' The optimised layer thickness is around 100 nm Cr and 40-50 nm Sm-Co, resulting in a maximum H_c of 4200 Oe.[21]

References

[1] R. M. White, J. Magn. Magn. Mater. **226**, 2042 (2001).

[2] J. G. Zhu and H. N. Bertram, J. Appl. Phys. **69**, 4709 (1991).

[3] J. G. Zhu and H. N. Bertram, IEEE Trans. Magn. **27**, 3553 (1991).

[4] T. Chen and T. Yamashita, IEEE Trans. Magn. **24**, 2700 (1988).

[5] F. J. Cadieu, T. D. Cheung, L. Wickramasekara, N. Kamprath, H. Hegde, and N. C. Liu, J. Appl. Phys. **62**, 3866 (1987).

[6] E. A. Nesbitt and J. H. Wernick, *Rare Earth Permanent Magnets*, (Academic, New York, 1973).

[7] U. Kullmann, E. Koester, and C. Dorsch, IEEE Trans. Magn. **20**, 420 (1984).

[8] N. R. Belk, P. K. George, and G. S. Mowry, J. Appl. Phys. **59**, 557 (1986).

[9] E. M. T. Velu and D. N. Lambeth, J. Appl. Phys. **69**, 5175 (1991).

[10] E. M. T. Velu and D. N. Lambeth, IEEE Trans. Magn. **28**, 3249 (1992).

[11] J. C. Lin, C. D. Wu, and J. M. Sivertsen, IEEE Trans. Magn. **26**, 39 (1990).

[12] N. Mahvan, A. M. Zeltser, D. N. Lambeth, D. E. Laughlin, and M. H. Kryder, IEEE Trans. Magn. **26**, 2277 (1990).

[13] Y. Okumura, H. Fujimori, O. Suzuki, N. Hosoya, X. B. Yang, and H. Morita, IEEE Trans. Magn. **30**, 4038 (1994).

[14] Y. Okumura, O. Suzuki, H. Morita, X. B. Yang, and H. Fujimori, J. Magn. Magn. Mater. **146**, 5 (1995).

[15] M. Gronau, H. Goeke, D. Schuffler, and S. Sprenger, IEEE Trans. Magn. **19**, 1653 (1983).

[16] X. B. Yang and T. Miyazaki, J. Magn. Magn. Mater. **86**, 37 (1990).

[17] Y. Liu, B. W. Robertson, Z. S. Shan, S. H. Liou, and D. J. Sellmyer, J. Appl. Phys. **77**, 3831 (1995).

[18] Y. Liu, D. J. Sellmyer, B. W. Robertson, Z. S. Shan, and S. H. Liou, IEEE Trans. Magn. **31**, 2740 (1995).

[19] S. Takei, Y. Otagiri, A. Morisako, and M. Matsumoto, J. Appl. Phys. **85**, 6145 (1999).

[20] S. Takei, A. Morisako, and M. Matsumoto, J. Appl. Phys. **87**, 6968 (2000).

[21] X. H. Liu, L. Y. Cui, S. X. Zhou, C. Y. Wang, B. Y. Quan, L. J. Wang, W. Zeng, A. L. Wang, and J. C. Chen, Mater. Sci. and Eng. A **304-306**, 1043 (2001).

[22] J. K. Howard, R. Ahlert, and G. Lim, J. Appl. Phys. **61**, 3834 (1987).

"Just as appetite comes by eating so work brings inspiration."
Igor Stravinsky.

Chapter 5

Sm-Co thin films: composition control

In this chapter the binary intermetallic alloy system, Sm-Co is studied from the point of view of composition control and the effect this has on the magnetic properties. From the literature reviewed in the previous chapter, films with compositions around the intermetallic $SmCo_5$ have been heavily studied. Therefore, in this preliminary study films with lower Sm content are investigated.

5.1 Film preparation

Thin films of Sm-Co were deposited by dc magnetron co-sputtering from two elemental targets onto an array of fused quartz substrates (no substrate heating). The UHV sputtering system described in section 3.2.1. was used. Prior to loading, the substrates were cleaned in acetone and isopropanol. Substrates were placed on the tray depicted in 3.2.1., enabling a number of films to be deposited in one run (typically 10-15) each having a different composition and hence the variation in magnetic properties could be investigated. The target-substrate distance varied between 71 and 112 mm and was altered by changing the number of stainless steel spacers, as shown in 3.2.1. The base pressure of the system was $5x10^{-7}$ Pa and the argon pressure during the film deposition was 3.1 Pa. In some cases a Cr buffer layer was used and this was grown in an argon pressure of 0.4 Pa. Film compositions were determined by EDS in a SEM with a relative precision of 1.5 %.

5.2 The effect of composition on the magnetic properties of Sm-Co films

5.2.1 Composition spread

The initial deposition was carried out at a target-substrate distance (d) of 71 mm and table 5.1 shows the results of the characterisation of the films. H_c values in bold type indicate that the easy axis is located in the film plane.

Sector of Tray	Sm Content (at. %)	Ratio Co:Sm	H_c (Oe)	Film Thickness (nm)
B4	1.11	89.1	320	100
B5	1.56	63.0	356	119
B6	3.50	27.6	441	127
B7	7.20	12.9	367	120
B8	11.27	7.9	**228**	134
C4	1.38	71.2	340	175
C5	1.59	61.9	345	208
C6	2.80	34.7	386	215
C7	5.39	17.5	475	210
C8	8.79	10.4	**222**	184

Table 5.1. Summary of results for d = 71 mm. Values of H_c in bold indicate an in-plane easy axis of magnetisation.

The table is presented in this fashion so that the relationship between the position of the targets and the composition of the films is apparent. Basically, the Co rich films are located at the top of the

tray and the Sm rich films are located towards the base of the tray. Fig. 5.1 shows the dependence of H_c on the film composition.

The curve is asymmetric, showing a maximum value of H_c of approximately 475 Oe at Sm = 5.3 at. % ($SmCo_{17.9}$). This shows that the extrapolated curve of Okumura *et al.*[1] shown in section 4.2 (the graph in Fig. 4.1 is shown without the best fit curve for clarity) for low Sm content is incorrect because there is actually a second maximum.

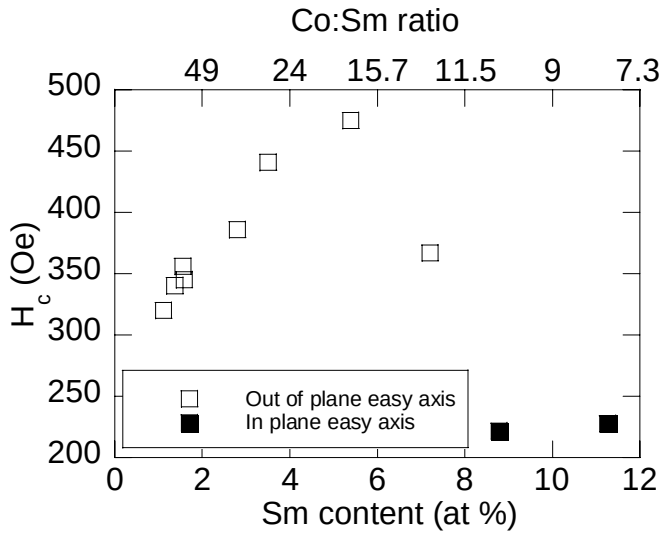

Fig. 5.1. Dependence of H_c on composition

The curve drops off more sharply at higher samarium concentrations, and at lower samarium concentrations the curve is tending towards H_c of a pure Co film.

5.2.2 Film morphology

Fig. 5.2 shows typical XRD patterns for films that have a Sm content that is a) less than 8 at. % ($SmCo_{11.5}$) and b) greater than 8 at. %. The black curve is a scan of the film grown on a fused quartz substrate and the red curve is a scan of the bare substrate carried out under identical conditions. For the film in Fig. 5.2a) only the (002) reflection of the $SmCo_{19.7}$ is present. The peak consists of an amorphous 'hump' and a nanocrystalline peak. The c lattice parameter was calculated to be 4.06 Å. By profile fitting the peak in Fig. 5.2a) and applying the Scherrer equation (section 3.3.2), the crystallite size was calculated to be about 5 nm. This is consistent with the TEM observations carried out by Liu *et al.*[2, 3] who found crystallites of about 5 nm in diameter distributed in an amorphous matrix in $SmCo_5$ films (discussed in previous chapter). The

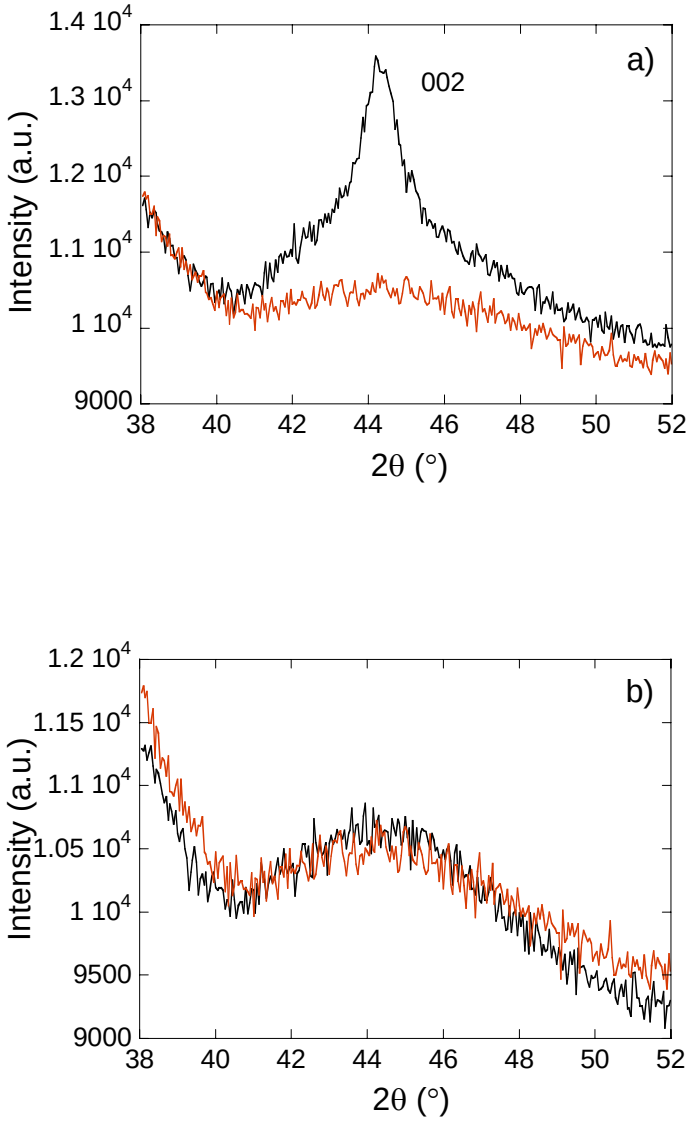

Fig. 5.2. X-ray diffraction patterns of a) $SmCo_{19.7}$ and b) $SmCo_{10.7}$ film.

volume fraction of crystallites was estimated by Liu *et al.* to be 91 % but by estimating the area of the peak in Fig. 5.2a), the volume fraction is much lower than this (~50 %). The film in Fig. 5.2b) shows no (002) reflection, only the amorphous hump from the substrate. This is in agreement with the literature, where the c-axis of the crystallites are preferentially growing in the plane of the film. Fig. 5.3 shows a FEG-SEM image of a $SmCo_{12.9}$ film. There is a distribution of apparent grain size, ranging from 15-50 nm, although the larger grains may contain smaller particles that could not be resolved. There are clearly defined grooved boundaries, as predicted by Thornton's zone structure model (section 2.2.5). A zone 1 structure is expected at low T_{sub} and this consists of fine-scale crystallites with domed tops and voided boundaries.

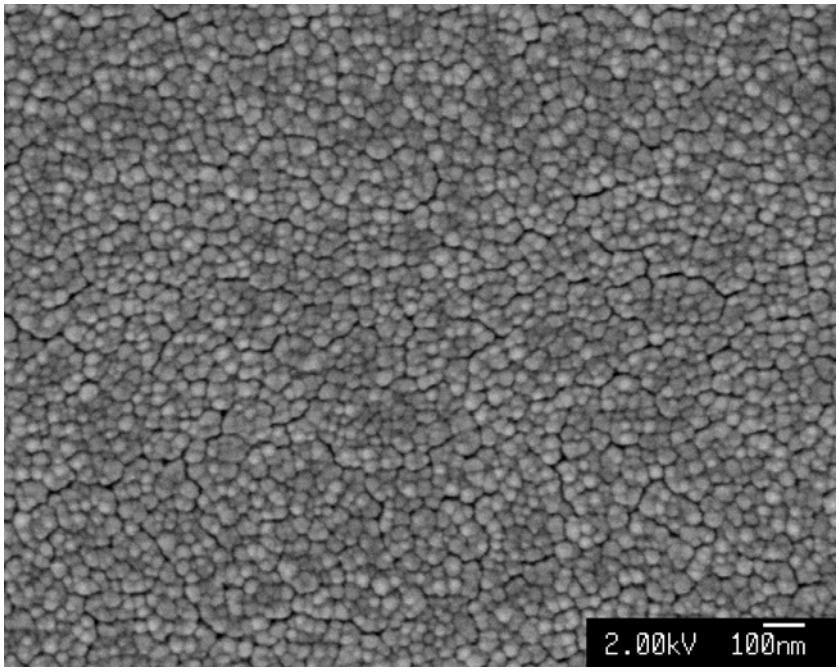

Fig. 5.3. FEG-SEM image of a $SmCo_{12.9}$ film.

Figure 5.4 shows an AFM image of the $SmCo_{12.9}$ film, which is similar to the FEG-SEM image, except the grooved boundaries cannot be seen. The grain shape is almost round. Once again there is a distribution of grain sizes, ranging from 10-60 nm. The rms roughness was 3.1 nm over an area of 1 μm^2.

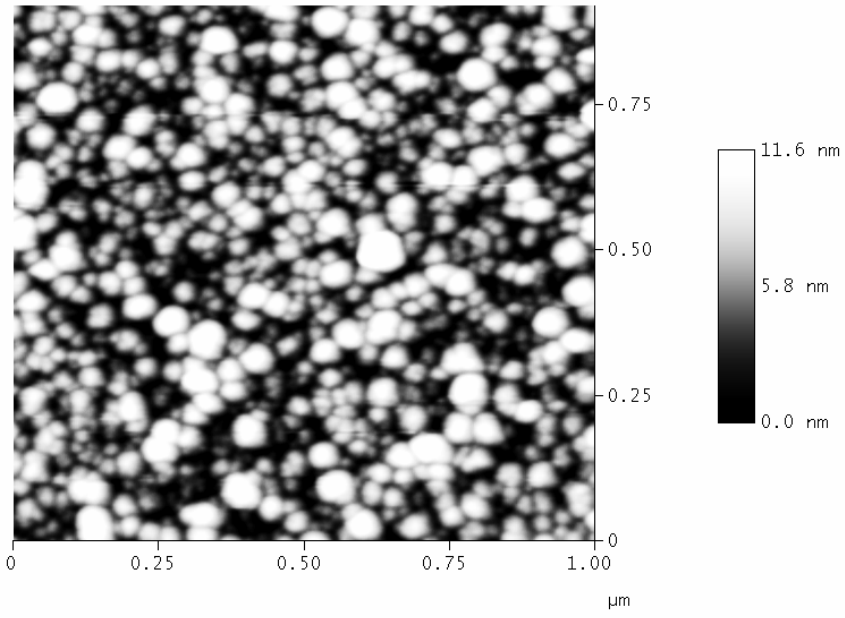

Fig. 5.4. AFM image of a $SmCo_{12.9}$ film (120 nm).

5.2.3 Magnetic properties

Hysteresis loops of a $SmCo_{17.5}$ and a $SmCo_{10.4}$ film are shown in Fig. 5.5. These were conducted in a VSM at room temperature. The shape of the 'out of plane' hysteresis loop, shown in Fig. 5.5a), is because of the demagnetising effect, explained in section 2.3.2. The easy axis can be recognised by the shape of the curve and the amount of hysteresis. It is located in the plane of the film for $SmCo_{10.4}$, but perpendicular to the film plane for $SmCo_{17.5}$. Sm-Co compounds are based on the hexagonal $TbCu_7$ system and the c-axis is the easy direction of magnetisation. Co is hcp and tends to grow with the c-axis aligned perpendicular to the plane of the substrate. Therefore, in the case of $SmCo_{17.5}$, which is Co rich, the c-axis of the crystallites are oriented out of the plane of the film (as confirmed by XRD in section 5.2.2) and so the easy axis of magnetisation is out of plane. For $SmCo_{10.4}$ the c-axis of the crystallites are oriented in the plane of the film (section 5.2.2) and so the easy axis of magnetisation is in plane. However, there are other factors that determine the direction of $\boldsymbol{M}$, such as the magnetostatic energy, E_m, which tends to prefer the direction of $\boldsymbol{M}$ to be in plane for a thin film. Sm, as we know, has a large crystalline anisotropy, and so there is competition between E_m and E_a. There is a critical concentration of Sm and probably a critical film thickness in which the transition from $\boldsymbol{M}$ being out of plane to in-plane occurs. This will be investigated further in later sections.

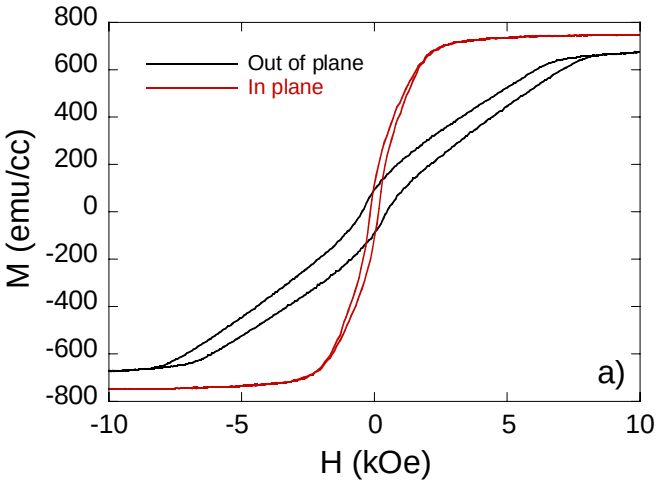

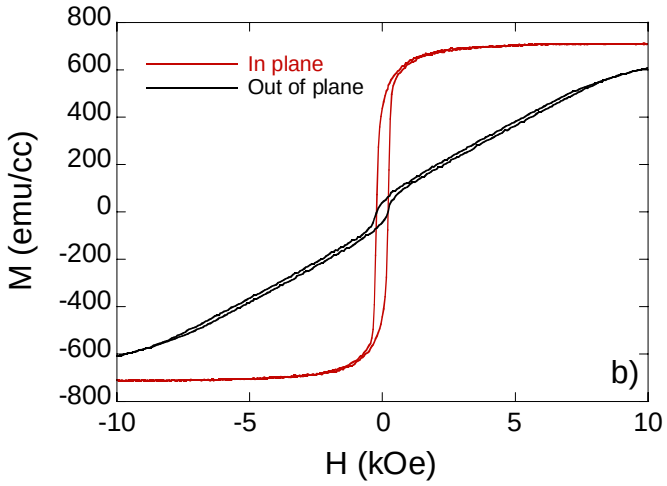

Fig. 5.5. Hysteresis loops of a) $SmCo_{17.5}$ (210 nm), b) $SmCo_{10.4}$ (184 nm) films.

In this initial deposition, the composition variation across the tray was too large: there was a composition variation across each film, which means a variation in magnetic properties. One way to reduce this large variation is to increase *d*. The flux of atoms from the two targets will be scattered more since the distance to the substrates is larger, so more mixing of the two target materials should occur. The effect of increasing *d* is discussed in more detail in the next section.

5.3 The effect of increasing *d* on the composition variation across the films

In order to compare directly the results, the position of the substrate tray relative to the targets must be maintained. Therefore, the inside of the chamber was marked using a diamond scribe, so that the tray would always be in the same position for each deposition. The results are shown in Fig. 5.6. The substrates were basically arranged in two lines on the tray, hence the red and blue lines shown in the graphs. However one can visualise a surface in between. As *d* increases, the composition variation decreases, as predicted, and the films become less cobalt rich. If one compares films in the same sector of the tray but at different values of *d*, the films at the top of the tray show a larger change in composition with d than the films at the base of the tray, but they all tend towards the same value (i.e. there is less variation in composition as *d* increases). This is illustrated in Fig. 5.7.

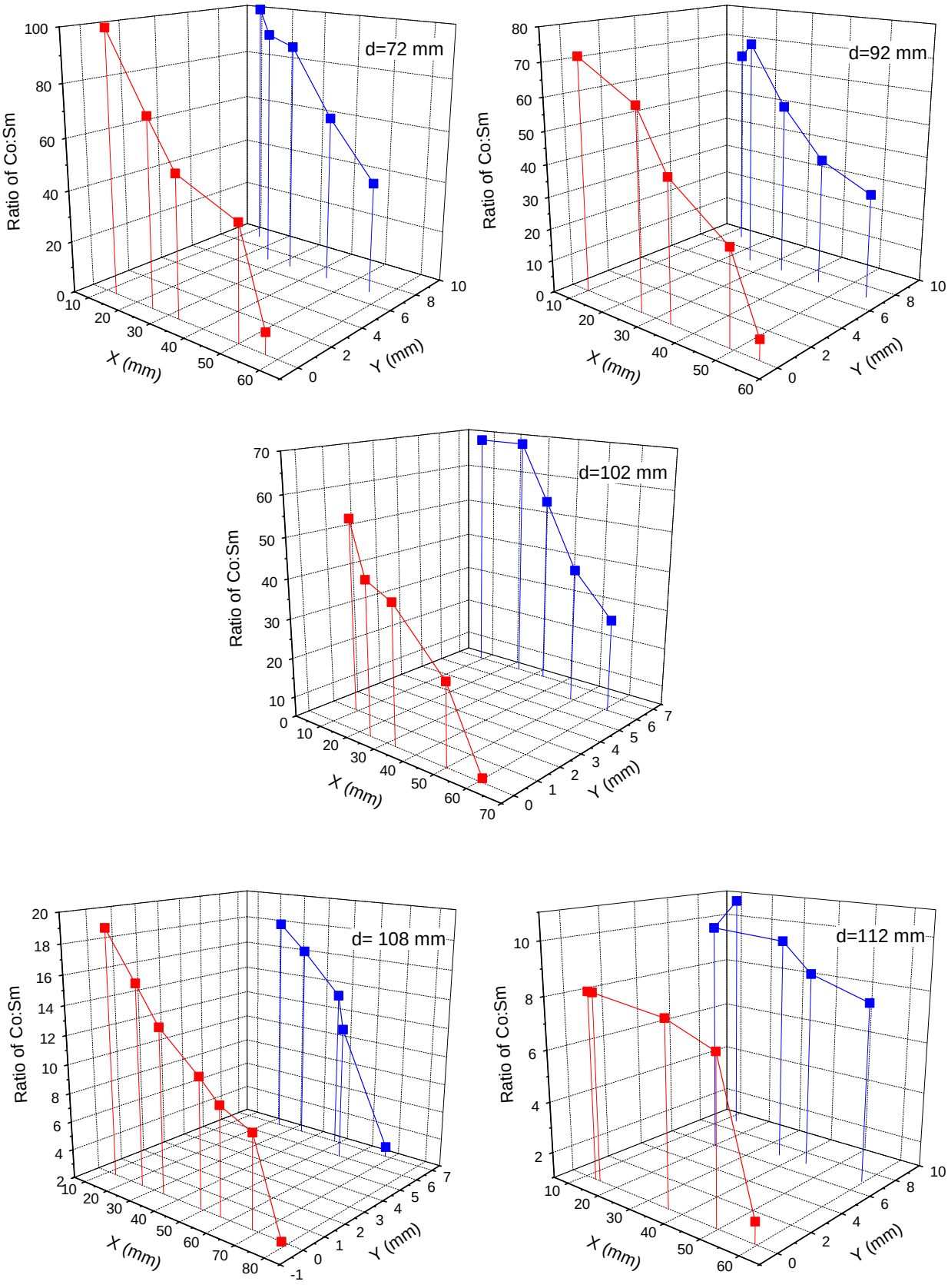

Fig. 5.6. Plots of composition variation across the substrate tray for different target-to-substrate distances, *d* (lines are a guide to the eye).

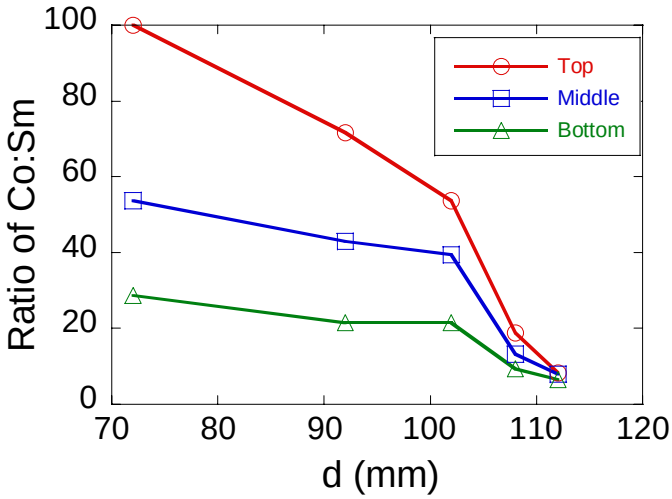

Fig. 5.7. Plot of how composition varies with *d* for a fixed substrate position (lines are a guide to the eye).

Films of interest were at d = 108 mm, because this target-substrate distance provided a good compromise between a reasonable composition spread across the substrate tray but small variation across each substrate (<4 % across a 5×5 mm^2 substrate). Another deposition was carried out to ensure that films of the same composition could be obtained. The composition was reproducible and so H_c of the films was determined, as described in the previous section. Table 5.2 shows a summary of the results. Once again, H_c values in bold type denote that the easy axis is located in the plane of the film.

Sector of Tray	Sm content (at. %)	Ratio of Co:Sm	H_c (Oe)	Film thickness (nm)
B5	4.83	19.7	534	78
B6	5.84	16.1	414	83
B7	6.85	13.6	299	74
B8	8.52	10.7	**215**	72
B11	12.25	7.2	**217**	44
C6	5.29	17.9	544	95
C7	5.72	16.5	490	101
C8	6.85	13.6	306	103
C9	7.80	11.8	**196**	70

Table 5.2. Summary of results for d=108 mm. Values of H_c in bold indicate an in-plane easy axis of magnetisation.

Comparing table 5.1 and table 5.2, the results are similar and do not to vary significantly with film thickness. It is the film composition, rather than the film thickness, which determines whether the

easy axis is located in the plane of the film or not, in this thickness regime. There is a critical composition, somewhere between $SmCo_{11.8}$ and $SmCo_{12.9}$ in which the easy axis changes from being in-plane to out of plane. In order to make the easy axis lie in-plane for films of composition greater than $SmCo_{12.9}$, the thickness of the films should be reduced in order to increase E_m, forcing the easy axis to be in-plane. The effect of film thickness is investigated in section 5.5.2.

Figure 5.8 shows a plot of H_c versus composition. The red curve represents the current results and the black curve is from the previous section (with smaller d). Once again, the filled symbols indicate that the easy axis of magnetisation is in-plane. The curves have a similar profile, both showing a maximum H_c for the $SmCo_{17.9}$ film.

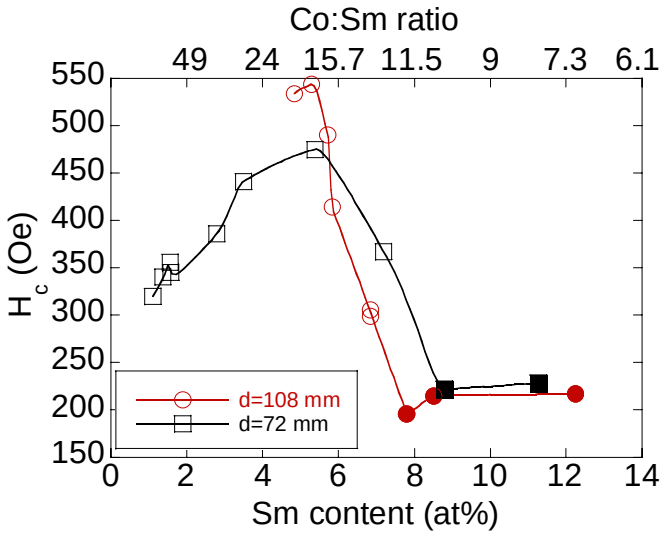

Fig. 5.8. Dependence of H_c on the ratio of Co:Sm (lines are a guide to the eye).

Fig. 5.9 shows an AFM image of the $SmCo_{16.1}$ film. The grain size varies from 10-45 nm and the structure looks more interconnected than the previous image (Fig. 5.4). The rms roughness was 2.3 nm over an area of 0.5 μm^2.

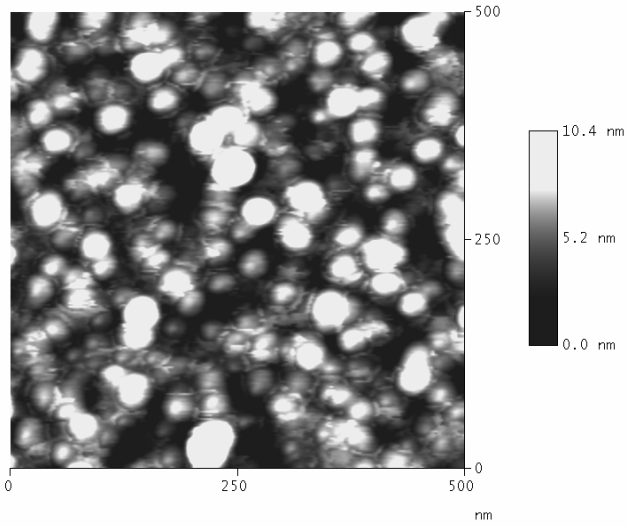

Fig. 5.9. AFM image of $SmCo_{16.11}$ (83 nm) film.

Since $SmCo_{17.9}$ has the largest H_c, it would be desirable for some applications if the easy axis could be in-plane. It is well known in the literature (chapter 4) that using an underlayer of polycrystalline Cr promotes the c-axis of Sm-Co films to lie in-plane and so the easy axis would also be in-plane. The next section investigates this.

5.4 The effect of using a Cr underlayer on the magnetic properties of Sm-Co films.

The quality of the Cr underlayer plays an important part in the H_c of the Sm-Co films. A smooth underlayer with small grains is required. Therefore, Cr films were deposited on a range of substrates to determine which one was the most suitable. The Cr underlayers are highly textured since the (110) XRD reflection is much more intense than the (200) reflection. This is expected since Cr is bcc, so the (110) close packed planes are likely to grow parallel to the substrate surface. The (200) reflection seems to be the least intense for the Cr grown on fused quartz. The crystallite sizes were evaluated using profile fitting, as described in section 4.2.3 and the results are shown in table 5.3. The mixing parameter, η determines the shape of the profile, from pure Lorentzian (η=0) to pure Gaussian (η=1) in the limiting cases. In this case, η is near to 1, so the profile is Gaussian, which means that the peak broadening is mainly due to size rather than strain broadening. Therefore any change in the integral breadth just results from a change in the grain size. There is not a huge variation in the results but fused quartz was chosen. The X-ray diffraction pattern of the Cr underlayer on fused quartz is shown in figure 5.10.

Substrate	(110) peak position (°2θ)	Integral breadth (°)	η	Lattice parameter (Å)	Grain size (nm)
Fused quartz	44.491	0.663	0.87	2.878	14.77
Glass	44.420	0.662	0.75	2.882	14.80
Sapphire	44.463	0.659	0.87	2.879	14.87
Silicon	44.456	0.662	0.86	2.880	14.80
Oxidised silcon	44.489	0.663	0.86	2.878	14.77

Table 5.3. Summary of the X-ray analysis for the Cr underlayers on different substrates.

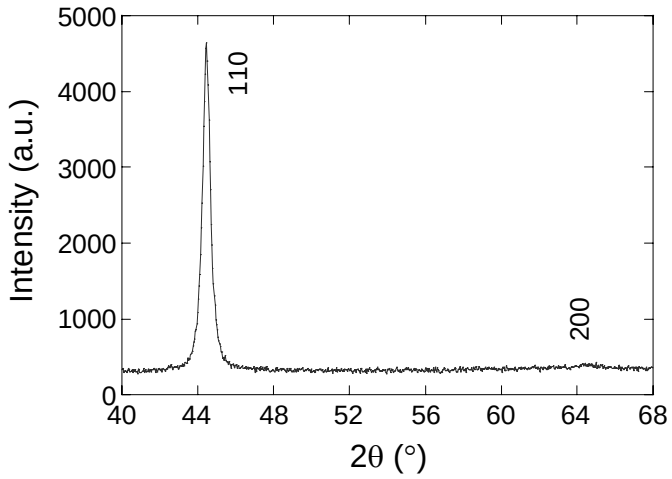

Fig. 5.10. X-ray diffraction pattern of Cr underlayer (250 nm) on fused quartz.

A deposition was carried out in which a series of Sm-Co films were deposited onto Cr underlayers (substrate was fused quartz). The results are summarised in table 5.4. Comparing table 5.4 and table 5.2, the results are fairly similar, although the films with in-plane easy axes have slightly higher coercivities than before. The Cr underlayer appears to have had little effect on the magnetic properties and the easy axis is still out of plane for the films of interest (i.e. films around the composition $SmCo_{17.9}$).

Sector of Tray	Sm content (at. %)	Ratio of Co:Sm	H_c (Oe)	Thickness of Sm-Co/Cr (nm)
B5	4.83	19.7	531	42/122
B6	5.84	16.1	482	44/109
B7	6.85	13.6	341	40/101
B8	8.52	10.7	**289**	38/116
B10	10.83	8.2	**278**	30/52
B11	12.25	7.2	**242**	24/47
C6	5.29	17.9	536	51/100
C7	5.72	16.5	471	54/86
C9	7.80	11.8	**272**	37/59

Table 5.4. Summary of results for the Sm-Co/Cr/fused quartz films at d=108 mm. Values of H_c in bold indicate an in-plane easy axis of magnetisation.

Figure 5.11 shows a plot of the maximum H_c obtained for each film composition. The blue curve represents the current results and the red curve is the data obtained from the deposition carried out at the same target-substrate distance but without the underlayer. The results are similar although the in-plane coercivities have been enhanced a little by the Cr underlayer.

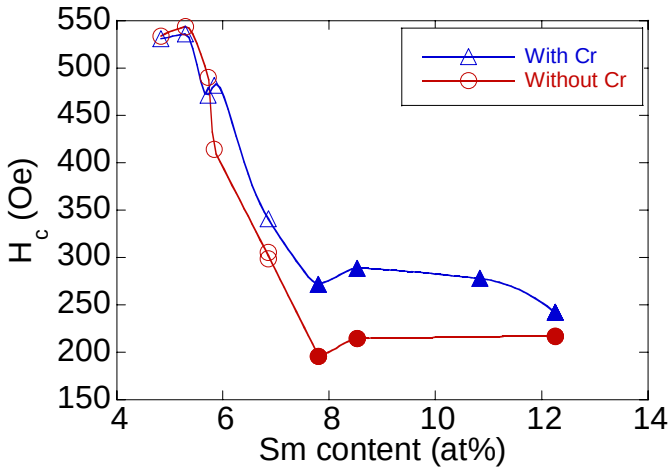

Fig. 5.11. Dependence of H_c on the Sm content (lines are a guide to the eye).

Since there is no change in the direction of the easy axis with the addition of the Cr underlayer for films with a Co:Sm ratio greater than 13.6, an X-ray scan was carried out to check that the Cr was still growing with a (110) texture. The X-ray diffraction pattern for the $SmCo_{19.69}$ film is shown in Fig. 5.12. The underlayer is growing with a (110) texture, so the fact that the easy axis remains out of plane cannot be attributed to a poorly oriented underlayer. The (002) peak from the Sm-Co layer cannot be seen because it occurs at the same value of 2θ as the Cr peak.

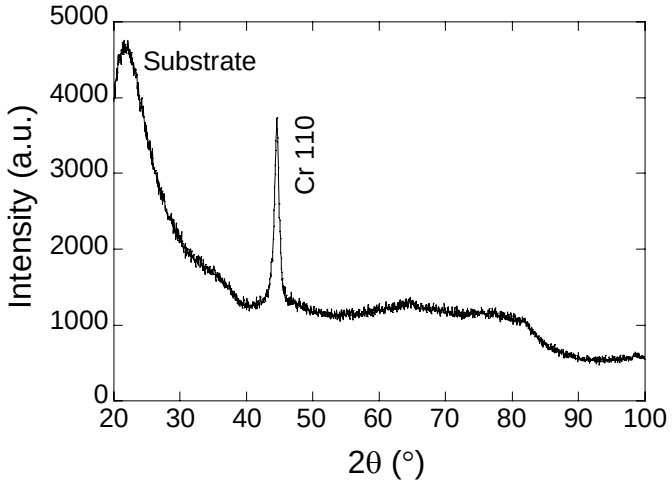

Fig. 5.12. X-ray diffraction pattern of a $SmCo_{19.69}$ (42nm)/Cr(122nm) film.

A thicker Cr underlayer (300 nm) was then deposited to see if this encouraged the c-axis of the Sm-Co layer to lie in-plane. Figure 5.13 shows an X-ray diffraction pattern of this film.

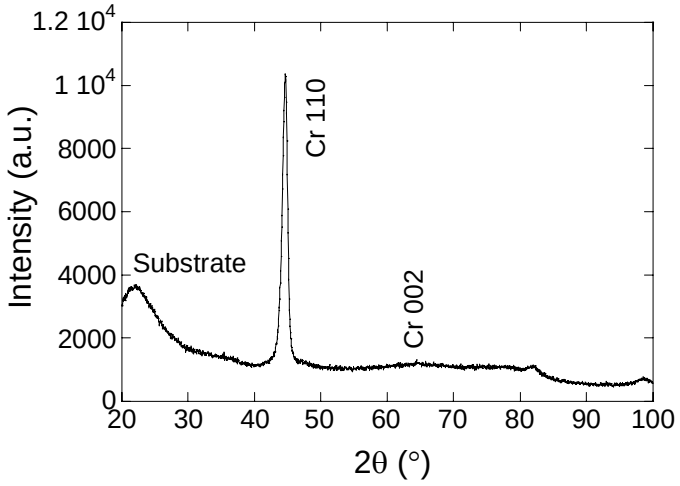

Fig. 5.13. X-ray diffraction pattern of a $SmCo_{19.69}$ (50nm)/Cr(300nm) film.

The Cr was still growing with a (110) texture. The (110) peak is much more intense relative to the substrate peak, compared to the previous scan simply because the Cr underlayer is about 2.5 times thicker. VSM revealed that the easy axis was still out of plane although the H_c was 600 Oe, which is slightly higher than before.

AFM was carried out on a 229 nm Cr film to determine the grain size and roughness (Fig. 5.14). The grains have an elongated form and seem to be connected in a string like fashion. Takei *et al.*[4] observed a similar morphology.

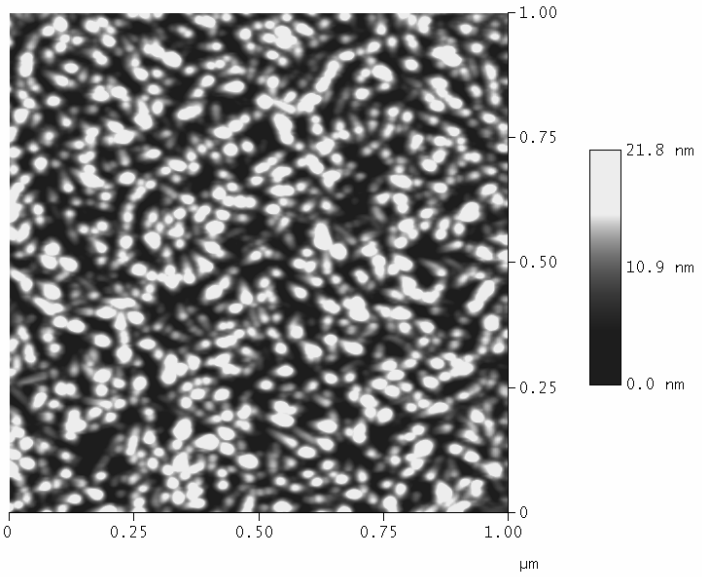

Fig. 5.14. AFM image of a Cr film (229 nm).

The grain size varies from about 14-35 nm and this is in agreement with the XRD analysis which estimated the crystallite size to be about 16 nm in a 40 nm film at d = 72 mm. The rms roughness was 4.6 nm over an area of 1 μm^2, which is smoother than the Cr underlayers deposited by Takei *et al.*[5] AFM was then carried out on the $SmCo_{17.9}$ film with a 300 nm Cr underlayer (Fig. 5.15).

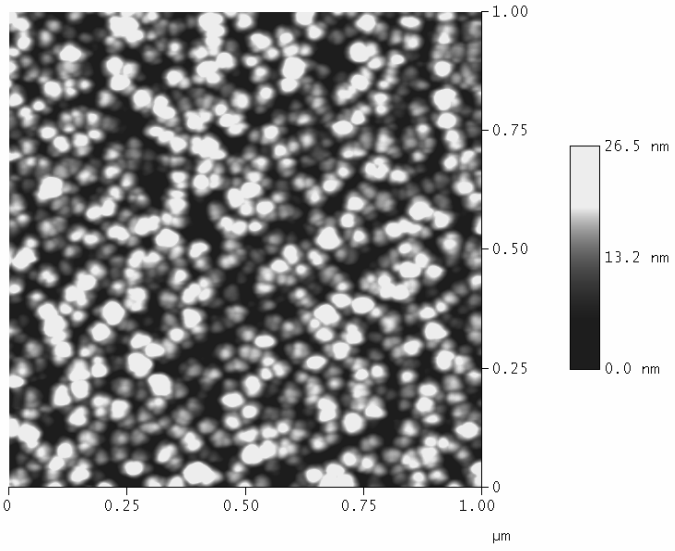

Fig. 5.15. AFM image of a $SmCo_{17.9}$ (50 nm)/Cr(300 nm) film.

The grain size ranges from 16-39 nm, which is similar to the Cr underlayer. This is in agreement with Takei *et al.*[5] who found that the grain size of the Sm-Co layer matched the grain size of the underlayer. They found that the grain size of both layers was about 50 nm, whereas the grain sizes obtained here are smaller.

However, the average grain size of the Sm-Co layer is larger than that of the Cr underlayer. Therefore, the grain size of the Cr underlayer needs to be larger in order to influence the growth of the Sm-Co layer. The rms roughness was 5.5 nm over an area of $1\mu m^2$, which is smoother than the films deposited by Takei *et al.*[5]

5.5 Controlling the orientation of the easy axis of magnetisation

5.5.1 Effect of not using liquid nitrogen cooling in the sputtering system

The geometry of the set up (section 3.2.1) meant that the substrate tray was in contact with the base of the sputtering chamber, which was being cooled by the liquid nitrogen jacket. In the literature, however, films were deposited at room temperature. Therefore, the deposition of the film shown in Fig. 5.13 was repeated but without nitrogen cooling. The easy axis is now in the plane of the film (Fig. 5.16). This can be explained by the increase in the mobility of ad-atoms in the Sm-Co layer, which enables them to follow the morphology of the Cr underlayer more closely. The next stage is to work on increasing the in-plane H_c.

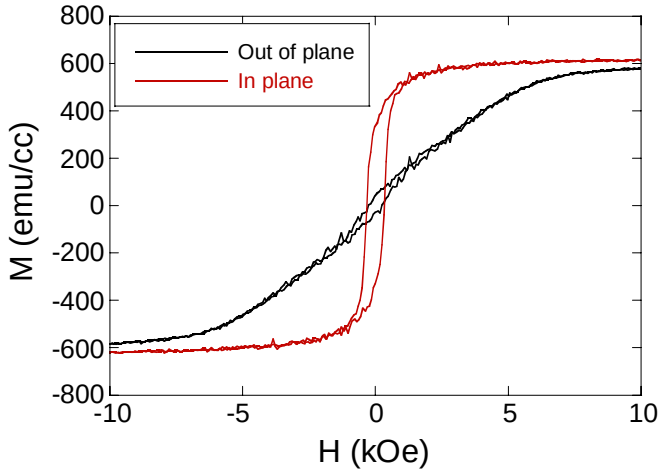

Fig. 5.16. Hysteresis loops of $SmCo_{17.9}$ (50 nm)/Cr(300 nm) film.

Fig. 5.17a) shows the effect of halving the power of both targets and not using the underlayer. Once again, the easy axis returns to being out of plane. Addition of the underlayer makes the out of plane component less easy.

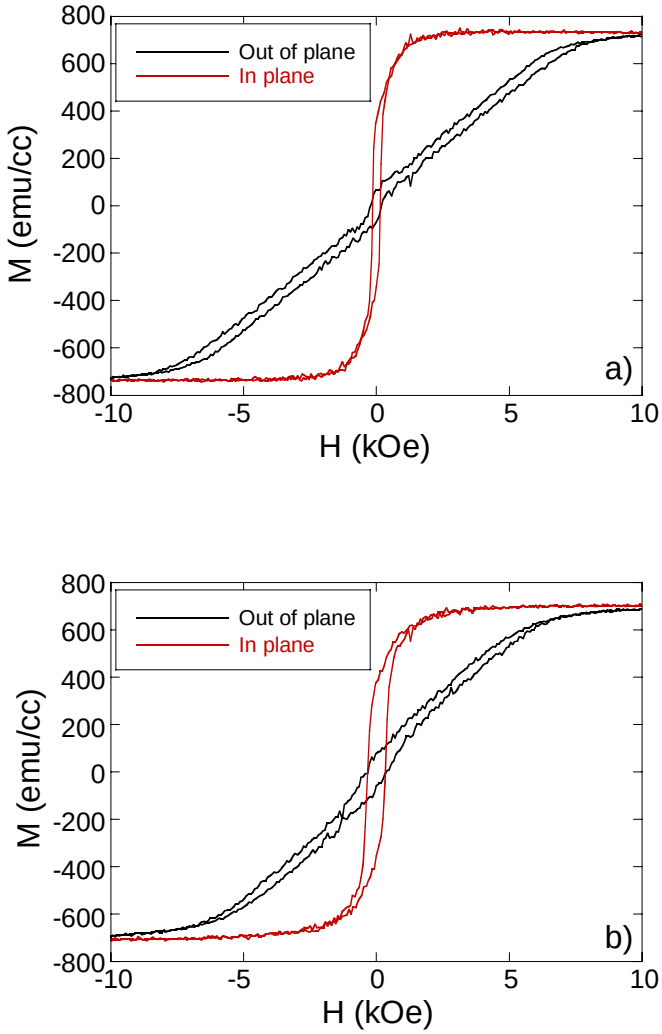

Fig. 5.17. Hysteresis loops of a) $SmCo_{19.0}$ (50 nm) and b) $SmCo_{19.0}$ (50 nm)/Cr (300 nm).

5.5.2 Effect of film thickness

Fig. 5.18 shows the effect of reducing the thickness of the Sm-Co layer from 50 nm to 20 nm. H_c is greatly increased from 358 Oe to 920 Oe. The easy axis is now well defined in the plane of the film. This can be explained by considering the increase in E_m due to the increased demagnetising field in the thinner film, as discussed in section 5.2.3. The increase of H_c with decreasing film thickness for Sm-Co thin films is also consistent with other studies.[6]

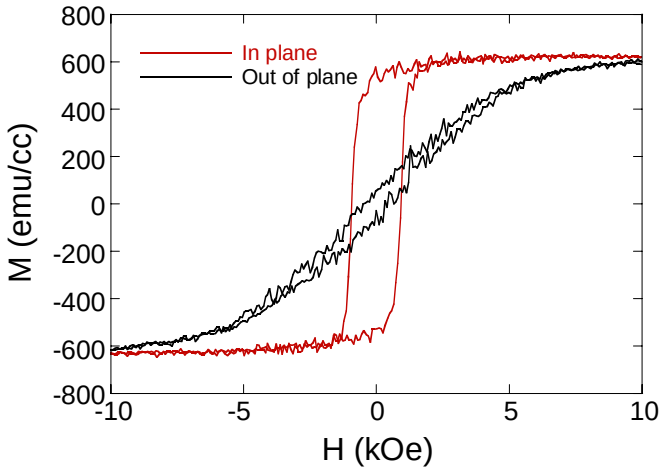

Fig 5.18. Hysteresis loop of a $SmCo_{19.0}$ (20 nm)/Cr (300 nm) film.

5.6 Summary

Thin films of Sm-Co were grown by co-sputtering from single elemental targets and this enabled good control of the film composition and more flexibility compared to using an alloy/mosaic target. Many films of different composition could be fabricated in one deposition by placing a large number of substrates on a tray located directly below the targets. The composition spread could be reduced by increasing the target-substrate distance.

Therefore, it was quickly determined that the maximum H_c in the composition range investigated (1-11 at. % Sm) occurred at a Sm content of 5.3 at. %. This is an off-stoichiometric compound, illustrating the importance of investigating a composition range. This study showed that there was a second maximum in the H_c at low Sm content that was not previously known about. There was a critical composition around 8 at. % in which the easy axis of magnetisation switched from being out of the film plane (<8 at. %) to in-plane (>8 at. %). This was supported by XRD measurements, which showed that the c-axis (easy axis of magnetisation) of the crystallites was oriented out of the film plane for compositions <8 at. % but in the plane of the film for compositions >8 at. %. It was found that for a fixed composition, the easy axis could be changed from being out of plane to in-plane by not cooling with the liquid nitrogen jacket during film growth and that H_c could be increased by decreasing the film thickness.

The preliminary study of this binary intermetallic system has provided good insight in how to construct a sputtering flange and in optimisation and tailoring of film properties. We are now in a position to scale this up to the growth and optimisation of a more complicated ternary intermetallic system (chapter 7).

References

[1] Y. Okumura, O. Suzuki, H. Morita, X. B. Yang, and H. Fujimori, J. Magn. Magn. Mater. **146**, 5 (1995).

[2] Y. Liu, B. W. Robertson, Z. S. Shan, S. H. Liou, and D. J. Sellmyer, J. Appl. Phys. **77**, 3831 (1995).

[3] Y. Liu, D. J. Sellmyer, B. W. Robertson, Z. S. Shan, and S. H. Liou, IEEE Trans. Magn. **31**, 2740 (1995).

[4] S. Takei, A. Morisako, and M. Matsumoto, J. Appl. Phys. **87**, 6968 (2000).

[5] S. Takei, Y. Otagiri, A. Morisako, and M. Matsumoto, J. Appl. Phys. **85**, 6145 (1999).

[6] E. M. T. Velu and D. N. Lambeth, J. Appl. Phys. **69**, 5175 (1991).

"The difficulty lies, not in the new ideas, but in escaping the old ones, which ramify, for those brought up as most of us have been, into every corner of our minds."
John Maynard Keynes.

Chapter 6

Heusler alloys: new materials for spintronics

In this chapter the family of ternary intermetallic alloys, Heusler alloys are reviewed. They are promising materials for both spintronics and the shape memory effect but we will focus mainly on spintronic applications.

6.1 Half Heusler alloys

In chapter 2 the two families of Heusler alloys and their respective crystal structures were introduced: the half Heusler alloys which have compositions of the form XYZ and the full Heusler alloys which have compositions of the form X_2YZ. The half Heusler alloy, NiMnSb was the first material which was predicted to be a HMF by de Groot *et al.*[1] in 1983 and has been the most extensively studied Heusler alloy. Hence we will begin by reviewing NiMnSb and other half Heusler alloys before moving on to discussing the full Heusler alloys. Some of the key results are summarised in table 6.1.

Material and Author	Fabrication Method	Deposition parameters	Substrate	Lattice parameter (Å)	M_s (μ_B/formula unit)	H_c (Oe)	ρ_{5K} ($\mu\Omega$cm)
Bulk value				5.903	4.0 (from theory)		
NiMnSb, Kabani *et al.*[2]	Simultaneous, three-source evaporation	623 K, post anneal at 773 K for 2 h	Sapphire	5.907	3.9	85	
NiMnSb, Caballero et al.[3]	rf magnetron sputtering, alloy target	523-623 K, 0.33 Pa	Glass	5.907	4.2	1	
NiMnSb, Ristoiu et al.[4]	dc sputtering, alloy target	673 K, 0.40 Pa	MgO (100), Mo buffer	5.905	3.9		5.3
NiMnSb, Gardelis et al.[5]	PLD	473 K	InSb(100)	5.984	4	2	6

Table 6.1. Summary of the properties of NiMnSb thin films.

6.1.1 Growth of the half Heusler alloy NiMnSb and PtMnSb

The first thin films of **NiMnSb** were grown by Kabani *et al.*[2] on glass and sapphire substrates by simultaneous three-source evaporation. Substrate temperature was 623 K during growth and films were subsequently annealed at 773 K for 2 h. Stoichiometric, polycrystalline films were obtained and thinner films (~80 nm) grown on sapphire had a (111) texture. The film lattice parameter of 5.907 Å was close to the bulk value of 5.903 Å.[6] M_s was found to be 3.9 μ_B/formula unit, which is in agreement with the theoretical value of 4.0 μ_B/formula unit,[7] and H_c was 85 Oe. NiMnSb and PtMnSb are found to exhibit interesting magneto-optical (MO) properties, like the magneto-optical Kerr effect (MOKE), important in MO recording technology. In this case, at room temperature the polar Kerr rotation at 3.5 kOe was 0.06°.

Caballero *et al.*[3] focussed on obtaining good quality films of **NiMnSb** at moderate temperatures. Low temperature growth is important for device structures involving metallic multilayers because interdiffusion at the interface is a problem and low interfacial roughness is required. Film roughness tends to increase with increasing temperature and thickness. Films were grown onto glass substrates by rf magnetron sputtering from a single, stoichiometric target. They found that a combination of low argon pressures (~0.33 Pa) and very low rf power (15 W) led to good quality films at moderate temperatures (~523-623 K). The deposition rate was 0.03 nm/s. The reduction in sputtering pressure corrected the initial problems of extra phases and off-stoichiometry. Like Kabani *et al.*[2] they also obtained a film lattice parameter of 5.907 Å and an M_s of 4.2 μ_B/formula unit (close to the theoretical value) but they obtained a much lower H_c of less than 1 Oe. A minimum roughness of 5 Å was observed at 0.40 Pa for a 20 nm film. Preliminary results indicated that the resistivity was independent of temperature in the 4.2-20 K range, which is consistent with the expected absence of spin-flip scattering in 100 % spin-polarized materials (discussed in section 2.4.3. in more detail). Magneto-optical Kerr spectra of optimised films[8] were very similar to bulk NiMnSb crystals, indicating that the band structure of these films reproduces that of the bulk. At room temperature the polar Kerr rotation was –0.33° in an applied magnetic field of ±26 kOe.

Ristoiu *et al.*[4] managed to achieve epitaxial growth of **NiMnSb** on MgO monocrystalline substrates (100) with a Mo buffer layer by dc facing-targets sputtering (an alloy target on a planar magnetron was used and three pairs of facing target sputtering electrodes). Although MgO and NiMnSb have a smaller lattice mismatch (1 %) compared to Mo and NiMnSb (5.8 %) it was found that the growth of NiMnSb directly onto MgO resulted in polycrystalline films (although (200) textured). It was thought that Mo wets the MgO surface better than NiMnSb. In agreement with Caballero *et al.*[3] it was found that film roughness increased with increasing temperature and sputtering pressure and optimum films were obtained at a pressure of 0.40 Pa, a deposition rate of 0.06 nm/s and a temperature of 673 K. The rms roughness was found to be 0.8-0.9 nm over an area of 10 μm^2. Four-fold magnetic anisotropy was observed, as expected for the cubic system. An M_s of 3.9 μ_B/formula unit was obtained, which is close to the theoretical value and a very low value of $\rho_{4.2\ K}$ of 5.3 $\mu\Omega$cm was reported. For both the magnetisation and the resistivity as a function of temperature, a transition at around 100 K was observed. It is postulated that there is a transition from a normal metal state (T>100 K) to a half-metallic state (T<100 K). This was studied in greater detail in a later work of Hordequin *et al.*[9] who found anomalies in various physical properties (resistivity, magnetisation, anomalous Hall coefficient, magnetoresistance) of NiMnSb near 80 K and explained these in terms of a cross-over from a half metallic state (T<

80 K) to a normal metallic ferromagnet (T> 80 K). They concluded that it would be desirable to find a compound where T_c was high (magnetic splitting between the up and down-spin subbands would be large) and the Fermi level falls at the bottom of the gap for the minority band (large energy difference between the Fermi level and the conduction band for the down spins). The half-metallic character would perhaps last up to higher temperatures compared to the Curie point.

Ristoiu *et al.*[10,11,12] also investigated surface segregation in **NiMnSb** since surface segregation is common in intermetallic compounds because the surface free energy is expected to be different from the bulk. Bona *et al.*[13] proposed that Sb segregation dominates the surface region. Ristoiu *et al.* found that during the growth of NiMnSb films, Sb and then Mn atoms segregate to the surface and hence the spin-polarisation is reduced. However, by removing the excess Sb by flash annealing, a nearly stoichiometric alloy surface terminated by a MnSb layer was obtained and a spin-polarisation of about 67 % was achieved at room temperature.

Gardelis *et al.*[5] are one of the few groups that have grown a Heusler alloy by PLD. **NiMnSb** was grown onto single crystal InSb(100) substrates at a substrate temperature of 473 K. Low temperature depositions were required because InSb-based structures suffer from structural damage when heated to temperatures above 523 K. Single phase, stoichiometric films were obtained and were polycrystalline with a (220) texture. An M_s of 4 μ_B/formula unit at 5 K was obtained, in good agreement with the theoretical value. A very low H_c of 2 Oe was achieved and $\rho_{5\ K}$ was 6 μΩcm. These results indicate that the films are of good structural quality unlike the previous PLD films grown on Si (111) substrates.[14] As for Ristoiu[4] and Hordequin,[9] they find that at low temperatures (T<200 K) the system behaves like a Heisenberg ferromagnet as expected for a half-metal, while at T>200 K it behaves like an itinerant ferromagnet. However, they observe this cross-over at higher temperatures, perhaps indicating that these films are of better quality so the half-metallic state persists to higher temperatures. In spite of the high quality of these films, the spin polarisation determined by point-contact Andreev reflection spectroscopy was only 45 %. However, this is a surface sensitive technique and so this value may not be representative of the bulk of the film.

Branford *et al.*[15,16] focussed on the transport properties of **NiMnSb** (grown by PLD by Gardelis *et al.*) to determine whether bulk-like transport could be achieved in thin films and hence evaluate NiMnSb as a potential spin injector. In contrast to the bulk stoichiometric material (for which spin-polarised holes are predicted), the Hall carriers in the films became increasingly electron-like as the film thickness decreased, and as the temperature increased from 50 K toward room temperature. The thickness dependence is probably due to the increasing significance of interface or free surface electronic states and so the current injected from a NiMnSb:semiconductor

interface may not necessarily carry the bulk spin polarisation. They conclude that strictly controlled interface engineering will be required in order to use this Heusler alloy as a spin injector, which will be demanding for these ternary alloys. Non-stoichiometric films showed a low temperature upturn in the resistivity for film thickness of 130 nm and below. This resistivity minimum corresponded to a maximum in the positive magnetoresistance and the magnitude of both of these increased with decreasing film thickness. They reported a positive magnetoresistance of more than 100 % at 200 K in 8 T for a 5 nm sample.

Moodera and Mootoo[17] were also very interested in the transport properties of **NiMnSb** and **PtMnSb**: two Heusler alloys that have been predicted to be HMF. The absence of states at E_F for minority spin electrons, means that these alloys should exhibit unique features in their transport properties. Films were grown by three-source co-evaporation onto glass substrates at 723-773 K and films were annealed at this temperature for 20 mins. They found that the resistivity versus temperature showed the absence of the T^2 dependence at low temperature (found in ferromagnets such as Fe and Ni). Below about 15 K both NiMnSb and PtMnSb showed a linear decrease with temperature, NiMnSb showing a more rapid decrease in resistance. The Hall constant increased significantly below about 100 K for both alloys, but once again NiMnSb shows the largest change. Similar behaviour had previously been observed by Otto *et al.*[18] in polycrystalline bulk samples. The transport data indicated a drop in the carrier density and a large increase in their mobility at low temperature, consistent with there being a gap at E_F for the minority spin band.

Ritchie *et al.*[19] looked at the properties of boules of **NiMnSb** grown by the Czochralski method. M_s was 4.02 μ_B/formula unit, in good agreement with the theoretical value. $\rho_{5\,K}$ is about 31 μΩcm and the resistivity ratio, RR was 1.7, suggesting a significant degree of atomic disorder. The spin polarisation at 4.2 K was found to be 45 % by point contact Andreev reflection spectroscopy.

Kautzky *et al.*[20] evaluated **PtMnSb** for its suitability as an electrode for giant magnetoresistance (GMR) applications. This half Heusler was grown epitaxially on Al_2O_3(0001) by dc magnetron co-sputtering at 773 K in 0.19 Pa argon. The films were very flat and films below 10 nm in thickness has an rms roughness of ~0.3 nm. XRD and VSM work indicated that the entire film was single phase and ferromagnetic with no evidence of a nonstoichiometric or oxidised surface layer. Hall-effect measurements carried out at room temperature yielded a positive sign of the Hall coefficient indicating that holes are the dominant carriers and similar values were obtained by both Moodera and Mootoo[17] and Otto *et al.*[18] From structure factor analysis of integrated x-ray peak intensities, atomic site disorder was estimated ~10 %. No evidence was found for defects at the surface of PtMnSb which might limit GMR but the results suggested that the bulk properties will play the largest role in determining the effectiveness of PtMnSb in GMR. However, they

pointed out that the poor GMR performance observed so far could also be due to factors relating to the multilayer structure (spacer layer, antiparallel HMF layer alignment). The progress of spin valve structures comprising one or more HMF is reviewed in section 6.3.1.

PtMnSb is regarded as a potential MO recording material because of its unusually high Kerr rotation. However, thin films have lacked the strong perpendicular magnetic anisotropy required for MO data storage. Kautzky *et al.*[21] tried to use epitaxial strain to achieve perpendicular magnetisation and so grew **PtMnSb** on MgO(001) with a W underlayer. However, the level of strain in the film was insufficient to induce perpendicular magnetisation. Polar MOKE measurements carried out at room temperature showed a peak rotation of 1.02° at 575 nm.

6.1.2 Growth of the half Heusler alloy NiMnSb on GaAs

As mentioned in chapter 1, the combination of related crystal structures with close lattice matching to compound semiconductors makes Heusler alloys ideal candidates for spin-injecting contacts to compound semiconductors. Turban *et al.*[22] found that the higher the growth temperature, the fewer the number of defects in NiMnSb epitaxial layers grown on MgO. However high growth temperatures are not appropriate for the case of growth onto semiconductors because of interfacial reactions that can form magnetic dead layers. Therefore it is necessary to make a compromise between crystal quality and interfacial reactions. The growth temperature of III-V semiconductors is chosen such that the sticking coefficient (fraction of incident atoms that stick to the sample surface) of the Group V element becomes zero once the surface is saturated with group V species. Therefore automatic stoichiometric growth is achieved because the growth is limited by the group III arrival rate. However, unlike III-V semiconductors, which are essentially line compounds, the Heusler alloys have large phase fields and so the composition may not be self-regulating. This means that achieving stoichiometric films is non-trivial and so the fluxes must be controlled carefully.

Van Roy *et al.*[23,24] pioneered the growth of NiMnSb on GaAs(001) by MBE. Unlike Turban *et al.*[22] who found that for high temperature growth (>850 K) Sb incorporation was self-limiting, Van Roy *et al.* found that this did not apply to the lower growth temperatures (373-673 K) that they were using. They found that controlling the Sb flux was particularly difficult, and the films had some twinning faults leading to inclusions of hexagonal MnSb.[25] In the case of stoichiometric NiMnSb, the amount of the MnSb phase was estimated to be about 14 % of the total sample volume. During initial growth runs there was the additional Mn_2As phase detected by XRD and was triggered by too high arsenic background in the chamber. This could be suppressed by pumping the chamber for ≥2 h after the growth of the GaAs buffer layer, annealing the GaAs 2×4

surface to remove excess As, over cooling the GaAs buffer in an Sb flux and the growth of GaSb, AlAs, and AlSb interface layers. Stoichiometric films were epitaxial and exhibited the bulk lattice constant but showed a reduced M_s (500-650 kA/m) from the bulk value (720 kA/m). Films exhibited a strong in-plane uniaxial magnetic anisotropy with an easy axis that was either [110] or [$1\bar{1}0$] depending on the growth conditions and choice of interlayer.

6.2 Full Heusler alloys

This second family of Heusler alloys has attracted a lot of interest and exhibits diverse magnetic phenomena, the transition from a ferromagnetic phase to an antiferromagnetic one (by changing the concentration of the carriers) being the most extensively studied.[26] Like NiMnSb and PtMnSb, a number of the full Heusler alloys have been predicted to be HMF (Co_2MnSi,[27] Co_2MnGe,[27] Fe_2MnSi[28]). However, Brown *et al.*[29] found that there is a finite density of states in the minority spin d band of manganese and so these compounds cannot be classified as HMF. Fortunately, the prediction of spin filtering at the Heusler alloy/semiconductor interface is expected to reduce the requirement for 100 % spin polarised materials while still achieving a high spin polarised injection efficiency.[30,31] The full Heusler alloy, Co_2MnSi will be discussed first in this review, since this is the alloy that is studied in this thesis. Other Heusler alloys will then be reviewed, and these have mainly been grown epitaxially on compound semiconductors by MBE. Results are summarised in table 6.2.

6.2.1 Growth of the full Heusler alloy Co_2MnSi (and a few other Co based full Heusler alloys).

Raphael *et al*.[32] were the first group to grow thin films of **Co_2MnSi**. Polycrystalline films 100-200 nm in thickness were grown by dc magnetron sputtering from an alloy target onto glass substrates. A range of deposition temperatures and sputtering gas pressures were investigated but the dc power was kept fixed at 30 W. Optimum properties were obtained at the highest deposition temperature of 773 K and the lowest sputtering pressure of 2.0 Pa. XRD patterns revealed that films grown below 423 K were amorphous but films grown between 573 and 773 K were single phase, (110) textured and had the $L2_1$ structure. As the deposition temperature increased and the sputtering pressure decreased, the lattice parameter decreased and the optimised film had a value of 5.6515 Å, close to the value of their bulk single crystal (5.6535 Å).[33] An M_s of 4.9 μ_B/formula unit (close to single crystal value of 5.1 μ_B/formula unit),[33] an H_c of 3 Oe and an rms roughness of 0.3 nm was obtained for the optimised film. $\rho_{5\ K}$ was 16 μΩcm and RR was 1.43, which is equal to or higher than RR of epitaxially grown single crystalline thin films of

Material and author	Fabrication method	Deposition parameters	Substrate	Lattice parameter (Å)	M_s (μ_B/formula unit)	H_c (Oe)	$\rho_{5\,K}$ ($\mu\Omega$cm)
Bulk value for Co_2MnSi				(5.6535)[33]	(5.1)[33]		
Co_2MnSi, Raphael *et al*.[32]	dc magnetron sputtering, alloy target	773 K, 2.0 Pa	Glass	5.6515	4.9	3	16
Co_2MnSi, Geiersbach *et al*.[34]	rf sputtering	743 K, 0.53 Pa	a-plane sapphire, V buffer	5.688	3.5		106
Co_2MnSi, Kämmerer *et al*.[35]	dc magnetron sputtering, alloy target	724 K, 0.27 Pa	Oxidised Si(111), V buffer	5.665	4.1	1.5	131
Co_2MnSi, Kim *et al*.[36]	dc magnetron cosputtering, single targets	773 K, 0.40 Pa	Oxidised Si	5.655	5.4	10-40	59
Co_2MnGe, Ambrose *et al*.[37]	MBE	448 K	GaAs(001)	5.77 (5.743)	5.1 (5.1)[38]	35	90
Ni_2MnGa, Dong *et al*.[39]	MBE	573 K	GaAs(001), $Sc_{0.3}Er_{0.7}As$ buffer	6.12 (5.825)	2.4 (4.1)[40]	10	82
Ni_2MnIn, Xie *et al*.[41]	MBE	353 K, anneal for 10 min at 433 K	InAs(001)	3.065 (6.069 for $L2_1$)[42]	2.6 (4.2)[31]	40	
Ni_2MnGe, Lu *et al*.[43]	MBE	433 K	GaAs(001)	5.96 (5.69 for $L2_1$)[44]	2.5	5 (at 50 K)	90

Table 6.2. Summary of the properties of full Heusler alloy thin films (values in brackets are bulk values).

Co_2MnGe.[37] From this they concluded that intragranular scattering (i.e. point defects) was the dominant scattering process as opposed to intergranular effects such as grain boundaries. In addition to this, the lattice parameter decreased towards the bulk value as the resistivity decreased, indicative of a reduction in antisite disorder,[38] which these ternary alloys are prone to. In the case of this alloy, it is most likely that there is disorder between the Co and Mn sublattices, since they have similar atomic radii. They proposed that the larger Mn cation residing on the Co sublattice caused an increase in lattice strain and this explains the reduction in lattice parameter as the deposition temperature increased. This was supported by neutron diffraction experiments performed on bulk samples, which showed that 10-14 % of the Mn atoms were on the Co sublattices with no detectable disorder between the Mn and Si sublattices.[45,46] The spin polarisation of bulk single crystals of Co_2MnSi and Co_2MnGe were determined using point contact Andreev reflection spectroscopy.[33] At 1.5 K, P was 50-55 % for Co_2MnSi and a little higher for Co_2MnGe (55-60 %).

Geiersbach *et al.*[34] investigated a range of Heusler alloys, grown from stoichiometric targets by rf sputtering. The optimised parameters were an Ar pressure of 0.53 Pa, a growth rate of 0.06 nm/s and a substrate temperature of 743 K. **Cu_2MnAl** grew epitaxially on MgO(100), and with a (110) texture on a-plane sapphire. However for the Co-based Heusler alloys investigated (**Co_2MnSi**, **Co_2MnSn** and **Co_2MnGe**) polycrystalline growth occurred when sputtering directly onto a-plane sapphire or MgO. Metallic seedlayers were required to obtain good quality textured growth and V, Au and Cr were the optimum underlayers for the Co_2MnSi, Co_2MnSn and Co_2MnGe alloys respectively. With the seedlayer, perfectly textured (110) films are obtained and they have a roughness below 1 nm. Cu_2MnAl and Co_2MnSi films did not preserve the stoichiometry of the target and this resulted in a reduced M_s from the bulk values, illustrating the importance of obtaining stoichiometric films. M_s was found to decrease with increasing temperature (from 5 K to RT) by about 5 % for Co_2MnSi and Co_2MnGe and by about 7 % for Co_2MnSn. The lowest H_c obtained was 70 Oe, which is much higher compared to other values in the literature for these alloys. The resistivity at 5 K was also high and was 110, 106, 60 and 26 μΩcm for the Co_2MnGe, Co_2MnSi, Co_2MnSn and Cu_2MnAl films respectively. In all the Co-based Heusler films they observed a shallow minimum in the ρ(T)-curve around 40 K and tentatively attributed it to a thermal excitation of charge carriers across the gap in the minority spin band.

Kämmerer *et al.*[35] focussed on achieving smooth films of **Co_2MnSi** with a good texture, since these are necessary requirements if these films will be incorporated into GMR or TMR structures. Films were grown by dc magnetron sputtering from a stoichiometric target onto a range of substrates. An argon pressure of 0.27 Pa was used and the deposition rate was 0.26 nm/s. Films grown at high temperatures tend to have very rough surfaces, but this can be overcome by lowering the sputtering pressure. Best films were obtained on oxidised Si (111) at 724 K. The films were polycrystalline with a lattice constant of 5.665 Å. 130 nm films had a rms roughness of 0.5 nm. H_c was low (1.5 Oe) but a reduced M_s of 4.12 μ_B/formula unit was obtained. $\rho_{300\,K}$ was high (170 μΩcm) and from this it was concluded the realisation of a large GMR amplitude was questionable and this alloy might only be useful for TMR applications only. However, Raphael *et al.*[32] obtained films with a much lower $\rho_{300\,K}$ of 23 μΩcm so this is not necessarily the case. It was found that at substrate temperatures of about 724 K, polycrystalline films could be prepared independently of substrate material and orientation. Like Geiersbach *et al.*[34] they found that using an underlayer of V improved the (110) texture of the films. A (110) texture was even obtained at room temperature but films showed a very low M_s of 0.25 μ_B/formula unit because of an additional amorphous phase in the films.

Kim *et al.*[36] grew films of **Co_2MnSi** and **Cu_2MnAl** on thermally oxidised Si substrates by DC, RF co-sputtering from single elemental targets. The argon pressure was 0.40 Pa and the deposition rate was 0.2 nm/s. The composition had to be optimised by trial and error, and films within 2 at. % from stoichiometric composition could be fabricated reproducibly. Polycrystalline films were obtained at 573 and 773 K for Cu_2MnAl and Co_2MnSi respectively, but at room temperature films were amorphous, although Cu_2MnAl showed some crystalline phase. Lattice parameters were close to the bulk value but the M_s for Cu_2MnAl was 6 % of the bulk value. This reduced M_s indicates that there is a lot of disorder in these films, although T_c was 600 K, which is very close to the bulk value (603 K). This indicates that the disordered phase can be transformed to the ordered phase by thermal activation. For Co_2MnSi, M_s was a little higher than that of the bulk but within the uncertainty of the measurement of the film thickness. The T_c of Co_2MnSi was extrapolated (950 K) and was slightly reduced from the bulk value of 985 K.[29] $\rho_{5\,K}$ was lower for the Cu_2MnAl film grown at 573 K (24 μΩcm) compared to the Co_2MnSi film grown at 773 K (59 μΩcm).

Ritchie *et al.*[19] looked at the properties of boules of **Co_2MnSi** grown by the Czochralski method. M_s was 4.78 μ_B/formula unit, reduced from the bulk value. $\rho_{5\,K}$ is about 7 μΩcm and RR was 3, which is more than half the value obtained by Raphael *et al.*[32] (RR=6.5), indicating that these boules are not of as high a quality. No MR was observed to within the limits of the measuring system. The spin polarisation at 4.2 K was found to be 55 % by point contact Andreev reflection spectroscopy, comparable to the value obtained by Cheng *et al.*[33]

6.2.2 Growth of full Heusler alloys on GaAs(001)

6.2.2.1 Co-based Heusler alloys

Ambrose *et al.*[37] grew single-crystal films of **Co_2MnGe** epitaxially on GaAs(001) by MBE. These were grown at a low substrate temperature of 448 K and the deposition rate was 0.003 nm/s. The lattice parameter obtained from RHEED pattern was 5.77 Å, slightly larger than the bulk value of 5.743 Å. M_s was in agreement with the bulk value and H_c was 35 Oe, which is relatively high for the Heusler alloys. Magnetically, the inequivalence of the two <110> directions (although they are both relatively easy) means that there is an in-plane uniaxial anisotropy along a <110> axis, although a cubic material should show fourfold anisotropy. $\rho_{5\,K}$ was 90 μΩcm, which is also high compared to films of NiMnSb, for example, although these films are about 10× thinner (25 nm).

Yang *et al.*[47] observed unusual magnetic switching behaviour of the above films. They showed single, double and triple hysteresis loops. This can be understood from a unique magnetic anisotropy consisting of the cubic magnetocrystalline anisotropy of single-crystal **Co_2MnGe**(001) films and the (surface) uniaxial anisotropy of comparable magnitude due to the epitaxy with the

underlying GaAs(001) substrate. Theoretical calculations of the hysteresis loops using coherent rotation show good agreement with the experimental results.

Chen *et al.*[48] grew films of **Co_2MnAl** epitaxially on GaAs(001) by MBE. M_s was 3.4 μ_B/formula unit, reduced from the theoretical value of 4.0 μ_B/formula unit.[49] A complex ferromagnetic transition occurs at around 800-1000 K: there is a transition at 756 K (comparable to theoretical value of T_c[26] of 808 K), but there is also a second one at 815 K. It is not clear how it was possible to carry out this measurement, since As from the substrate will start out-diffusing at around 650 K, and this could explain the double transition observed. Like Ambrose *et al.*[37] they also observed a weak uniaxial anisotropy, the [110] being the easier of the two <110> directions. These films exhibited a giant Hall effect arising from the extraordinary Hall effect.

6.2.2.2 Ni-based Heusler alloys

The MBE growth of Ni-based Heusler alloys on compound semiconductors has been pioneered at the University of Minnesota. Dong *et al.*[39] looked at the growth of **Ni_2MnGa** on GaAs(001) by MBE. The interest in this particular alloy is because of the exceptionally large magnetostriction (~4.3 %) observed in bulk single crystals.[50] Thin films of this ferromagnetic shape memory alloy would be promising for microelectromechanical systems (MEMS). Single crystal films are expected to have superior properties over polycrystalline ones, and so epitaxial growth of single crystal films is desired.[51] Control of the first few atomic layers is important for controlling the growth orientation and so a lattice matched template layer of $Sc_{0.3}Er_{0.7}As$ was used. Epitaxial films of Ni_2MnGa were obtained but found to be growing pseudomorphically on GaAs. Ni_2MnGa was growing with a tetragonal structure with a=b=5.65 Å and c=6.12 Å. This is surprising since the critical thickness for a 3 % mismatch system is expected to be substantially thinner than 300 Å (current film thickness). M_s was 450 emu/cc, H_c was 10 Oe and no strong in-plane anisotropy was observed. T_c was found to be ~320 K, lower than the cubic bulk (376 K),[42] which could be due to the tetragonal structure of the Ni_2MnGa film.

Dong *et al.*[52] then looked at using a relaxed NiGa interlayer. Similar properties were obtained, but a different tetragonal phase was obtained (a=b=5.79 Å and c=6.07 Å), suggesting that **Ni_2MnGa** is a very compliant material that can relieve stress by changing its crystal structure rather than forming misfit dislocations. This means that one has more freedom in choosing the semiconductor substrate without the formation of interfacial misfit dislocations and so this is an ideal candidate for possible spin-injection devices. T_c is about 350 K, still reduced from the bulk value but still higher than the value obtained using the $Sc_{0.3}Er_{0.7}As$ template.

Xie *et al.*[41] investigated the growth of **Ni_2MnIn** on InAs(001) by MBE, because InAs is of great interest for spintronic applications because of its high electron mobility and the ease to form an ohmic contact to it. Epitaxial growth was achieved and films had the B2 crystal structure with a lattice constant of 3.065 Å (about half the value for the $L2_1$ phase, a=6.069 Å).[42] M_s of 420 emu/cc was obtained and H_c was 40 Oe. T_c was 170 K, which is substantially lower than the bulk (314 K)[42] and this is probably because of the difference in crystallographic structure as observed by Dong *et al.*[52]

Lund *et al.*[53] looked at the magnetotransport properties of **Ni_2MnGa**, **Ni_2MnGe**, and **Ni_2MnAl** grown by MBE onto GaAs(001). The zero temperature resistivities are quite large (80-160 μΩcm for 90 nm films) but the overall variation with temperature is weak. Both Ni_2MnGa and Ni_2MnGe (the ferromagnetic alloys) show a crossover from metallic to weak semiconductor-like behaviour around their respective T_c of 340 and 300 K and this correlates with a maximum in the negative MR. Ni_2MnGe showed an upturn in the resistivity at temperatures below 20 K and this is due to weak localisation or electron-electron interaction effects. These anomalous properties were taken as evidence that these alloys are not conventional metals and should be considered as heavily disordered electronic systems.

Dong *et al.*[54] investigated the magnetic behaviour of **Ni_2MnAl**, which out of all the investigated bulk samples of Ni_2MnZ (where Z is a group IIIA or IVA element) is the only alloy that is either antiferromagnetic or ferromagnetic depending on the crystal structure (B2 or $L2_1$). Films of Ni_2MnAl were grown on GaAs(001) by MBE with $Sc_{0.3}Er_{0.7}As$ interlayers. Lower growth temperatures (<523 K) resulted in non-ferromagnetic films, while higher growth temperatures (~673 K) gave rise to ferromagnetic films. This was proposed to be due to an increased atomic ordering of Mn and Al atoms resulting in a more $L2_1$-like crystal structure as the growth temperature is increased. The exchange bias effect at ferromagnet/antiferromagnet interfaces was used to test if the non-ferromagnetic films of Ni_2MnAl were antiferromagnetically ordered. Ni_2MnAl/Ni_2MnGe and Co/Ni_2MnAl bilayers were exchange biased, indicating that Ni_2MnAl films grown at 453 K are antiferromagnetically ordered.

Lu *et al.*[43] grew epitaxial films of **Ni_2MnGe** on GaAs(001) at 433 K by MBE. Ni_2MnGe grew in a tetragonally distorted $L2_1$-like structure (a=5.65 Å, c=5.96 Å). A diffraction pattern from an area including both Ni_2MnGe and GaAs showed a complete overlap of the diffraction spots in the in-plane [110] direction, but a splitting in the growth direction [001], indicating this tetragonal distortion. Pseudomorphic growth is not expected for an 85 nm film with a 0.8 % mismatch. However, Ni_2MnGe is known to have a fairly broad free energy minimum as a function of the c/a ratio (similar to that of the Heusler alloy Ni_2MnGa),[55] suggesting that it may be energetically

favourable for it to grow tetragonally strained rather than relaxing by forming mismatch dislocations at the interface. Magnetic measurements reveal that the films are ferromagnetic with a weak in-plane anisotropy and a T_c of about 320 K.

Interfacial reactions are a major issue for the full Heusler alloys on compound semiconductors. It has been found that interfacial reactions between Co thin films and GaAs start at around 600 K by the formation of a ternary phase, most probably Co_2GaAs.[56] Mn films on GaAs(001) annealed at 573 K showed interfacial reactions resulting in the formation of an epitaxial two phase region of Mn_2As and MnGa.[57] Minimal interfacial reactions occurred at anneals of 473 K. Research at the University of Minnesota (most of the above section) found that for the growth of Ni_2MnGe above 473 K, cross-sectional TEM studies indicated that interfacial reactions had occurred, but for growth at 373 K, a large number of planar defects formed. Optimum growth was obtained at 433 K, but by using interlayers (e.g. $Sc_{0.3}Er_{0.7}As$ discussed earlier) the Heusler layer can be grown at higher temperatures and so it is not necessary to compromise on the structural quality of the film.

6.3 Devices utilising Heusler alloys

The high spin polarisation of these alloys means that they should increase the GMR and TMR amplitude of devices if one or both of the ferromagnetic electrodes are replaced with a Heusler electrode. Both spin valve and tunnel junction devices utilising Heusler alloys as the electrodes are reviewed in this section and a summary of the performance of these devices is provided in table 6.3.

Author	Heusler electrode	Device	GMR/TMR
Hordequin *et al.*[58]	NiMnSb	Spin valve, CIP	1 %, 60 K
Caballero *et al.*[59]	NiMnSb	Spin valve, CPP	9 %, 4.2 K
Kelekar *et al.*[60]	$Co_2Cr_{0.6}Fe_{0.4}Al$	Spin valve, CIP	4%, 15 K (2 %, 295 K)
Tanaka *et al.*[61]	NiMnSb	Tunnel junction	8.1 %, 77 K (2.4 %, RT)
Inomata *et al.*[62,63]	$Co_2Cr_{0.6}Fe_{0.4}Al$	Tunnel junction	26.5 %, 5 K (16 %, RT)
Conca *et al.*[64]	$Co_2Cr_{0.6}Fe_{0.4}Al$	Tunnel junction	9.9 %, 77 K (6 %, RT)
Kubota *et al.*[65]	Co_2MnAl	Tunnel junction	40 %, RT
Kämmerer *et al.*[66]	Co_2MnSi	Tunnel junction	86 %, 10 K (33 %, RT)

Table 6.3. Summary of the performance of spin valve and tunnel junction devices.

6.3.1 Spin valve structures with Heusler electrodes

Hordequin *et al.*[58] looked at CIP spin valve structures employing **NiMnSb** as the ferromagnetic layers, Mo as the spacer layer and amorphous $SmCo_2$ as the biasing layer. The optimised structure was: NiMnSb(6 nm)/Mo(2 nm)/NiMnSb(6 nm)/a-$SmCo_2$(46 nm). The Heusler layers were grown at 523 K. A clear spin-valve contribution of about 1 % at 60 K was observed in a field of 50 mT. Measurements were not carried out below this temperature because the a-$SmCo_2$ would not reach saturation owing to its high magnetocrystalline anisotropy. The low value of MR is disappointing considering the expected high polarisation of the Heusler layers. However, three limiting factors were considered to account for this low value: i) Large resistivity of the Mo layer, ii) Existence of magnetic dead layers at the NiMnSb/Mo interfaces and iii) Incomplete antiferromagnetic alignment at T<60 K (because of pinning layer). The half-metallic character is only expected to exist below 80 K in bulk and probably at even lower temperatures in thin films. Lower resistivity spacers (e.g. Cu, Ag, Au) were not used because of significant interdiffusion and the precipitation of interfacial secondary phases (Mn, NiSb). It is thought that larger effects could be achieved by growing similar structures epitaxially or performing measurements in the CPP configuration.

Caballero *et al.*[59] investigated CPP spin valve structures using **NiMnSb** as the ferromagnetic layers, Cu as the spacer layer and FeMn as the biasing layer. Sample was sandwiched between crossed, Nb strips. Optimised structure was NiMnSb(20 nm)/Cu(15 nm)/NiMnSb(10 nm)/FeMn(10 nm). The intrinsic CPP-GMR was <10 % which suggests that improvements in the crystalline quality of NiMnSb and NiMnSb/Cu interfaces are necessary. Epitaxial Nb layers with subsequent growth of epitaxial NiMnSb could increase the GMR.

Kelakar *et al.*[60] carried out preliminary work on CIP spin valve structures using the Heusler alloy **$Co_2Cr_{0.6}Fe_{0.4}Al$**. This compound is of particular interest because bulk polycrystalline compacts were found to exhibit a large magnetoresistance of 30 % at room temperature in a magnetic field of 0.1 T, whereas similarly prepared samples of Co_2CrAl showed a negligible magnetoresistance.[67] $Co_2Cr_{0.6}Fe_{0.4}Al$(10 nm)/Cu(2.5 nm)/$Fe_{10}Co_{90}$(8.1 nm) on MgO had an MR of 4 % at 15 K and 2 % at 295 K. This is the highest MR to date for CIP spin valves using Heusler alloy electrodes.

Takahashi *et al.*[68] investigated CPP-GMR devices fabricated with **Fe_3O_4** as the magnetic layers. Films were grown on Au at 523 K. Fe_3O_4(5 nm)/Au (5 nm)/Fe_3O_4(40 nm) showed an MR of 0.04 % at RT and a ΔRA of 3.9 $m\Omega\mu m^2$.

Van Dijken *et al.*[69,70] investigated CIP spin valve structures with **Fe_3O_4** as the magnetic layers. Fe_3O_4/Au/Fe_3O_4 spin valves exhibited a clear AMR, but no GMR because of simultaneous

magnetic reversal in the two Fe_3O_4 layers. However, Fe_3O_4/Au/Fe spin valves showed a negative GMR of –0.16 % at 90 K (-0.05 % at 300 K). The negative GMR was attributed to an inverse electron spin scattering asymmetry at the Fe_3O_4/Au interface or an induced spin scattering asymmetry in the Au interfacial layers.

6.3.2 Tunnel junctions with Heusler electrodes

Tanaka *et al*.[61] investigated ferromagnet-insulator-ferromagnet tunnel junctions with one **NiMnSb** electrode. A maximum JMR of 8.1 % was observed in NiMnSb/Al_2O_3/$Ni_{0.8}Fe_{0.2}$ junctions at 77 K (2.4 % at RT). These junctions had 10 % additional Mn, but junctions with stoichiometric NiMnSb showed a smaller JMR of 6.1 % at 77 K, indicating that some depletion of Mn due to oxidation may be a problem. The JMR observed was much lower than expected, and using the Jullière model,[71] the polarisation was estimated to be only 15 % for NiMnSb. However, tunnelling is an extremely surface sensitive technique and the quality of the surface composition and structure of the NiMnSb is unknown.

Inomata *et al*.[62,63] looked at tunnel junctions with one **$Co_2Cr_{0.6}Fe_{0.4}Al$** electrode. This alloy was found to grow with the B2 (CsCl-type) structure at RT, as opposed to the $L2_1$ structure. A large TMR of 26.5 % at 5 K (16 % at RT) was obtained for $Co_2Cr_{0.6}Fe_{0.4}Al$(10 nm)/AlO_x(1.8 nm)/CoFe(3 nm)/NiFe (5 nm)/IrMn (15 nm)/Ta (5 nm) deposited on thermally oxidised Si substrate without a buffer layer. This is a promising alloy for spintronic applications because it crystallises at RT and a recent theoretical study showed that the CrAl-terminated (001) surface of Co_2CrAl has a large polarisation of 84 % (unlike the (001) surfaces of other Co-based Heusler alloys which lose the half metallic character and the net spin polarisation at the Fermi level is close to zero).[72] They also investigated having the $Co_2Cr_{0.6}Fe_{0.4}Al$ as the upper electrode, instead of the bottom electrode. Similar TMR was obtained (27.2 % at 5 K and 19.1% at RT), suggesting that $Co_2Cr_{0.6}Fe_{0.4}Al$ films form the B2 structure without any magnetic dead layers at the interface on an AlO_x layer, even though the Heusler layer is deposited onto a thin amorphous AlO_x layer. By using the Jullière expression the spin polarisation of the $Co_2Cr_{1-x}Fe_xAl$ was estimated to be 15.7 % for x=0, 29.2 % for x=0.4, 30.1 % for x=0.6, and 45.8 % for x=1.

Conca *et al*.[64] also looked at tunnel junctions employing one electrode of **$Co_2Cr_{0.6}Fe_{0.4}Al$**. However, not such large TMR was obtained, 9.9 % at 77 K (6 % at RT) for the following device structure: $Co_2Cr_{0.6}Fe_{0.4}Al$(125 nm)/AlO_x/Co(200 nm). The minimum thickness of the Heusler electrode was 125 nm in order to reduce the resistance of the bottom electrode, because otherwise one would not be able to discard the effects of geometrical enhancement of the TMR ratio. Best crystallographic properties of the Heusler layer were obtained at deposition temperatures of 873 K.

However, for optimum device performance films were deposited at room temperature to obtain smooth surfaces to grow a good insulating barrier. Increasing the growth temperature to 673 K did not affect the TMR significantly, but higher growth temperatures resulted in very low or nonexistent TMR signal. This is possibly due to increased roughness of the Heusler surface and an enhanced degradation of the surface due to oxygen impurities in the sputtering gas.

Kubota *et al.*[65] have obtained the largest TMR at RT for MTJs utilising Heusler electrodes. After annealing the device structure at 523 K the RT TMR increased from 27 % to 40 %. The device structure is Si/SiO_2/Cr(5-10 nm)/Co-Mn-Al(20-50 nm)/Al(2 nm)-O/Co-Fe(4 m)/Ir-Mn(10 nm)/cap layer. **Co_2MnAl** has a B2 structure with partial disorder between the Mn and Al atoms and so it is surprising that the maximum TMR value obtained was larger than previous reports based on ordered Heusler alloys. Previous calculations carried out for the perfect ordered state ($L2_1$) showed that the spin polarisation was low.[27] For the B2 structure the density of states was calculated, and it was deduced that the spin polarisation was 76 % and just considering the s-electrons it was 88 %. This supports the large TMR results that were obtained experimentally.

Kämmerer *et al.*[66,73] investigated tunnel junctions employing Co_2MnSi as one of the ferromagnetic electrodes. A large TMR of 86 % was obtained at 10 K, but this dropped off rapidly with increasing temperature and was 33 % at RT. From the Jullière model the spin polarisation of the Co_2MnSi was estimated to be 61 %. The device structure was as follows: SiO_2/V(42 nm)/Co_2MnSi(100 nm)/AlO_x(1.8 nm)/$Co_{70}Fe_{30}$(5.1 nm)/$Mn_{83}Ir_{17}$(10 nm)/Cu(40 nm)/Ta(5 nm)/Au(40 nm). After plasma oxidation of the Al layer, the structure was annealed for 40 min at 723 K to induce texture and atomic ordering into the Co_2MnSi layer (which was deposited at RT) and to homogenise the AlO_x barrier. The rapid decline of TMR with increasing temperature was attributed to the presence of a plasma oxidation induced Mn/Si segregation and oxide formation at the barrier interface that enlarges the effective barrier thickness.[74]

References

[1] R. A. de Groot, F. M. Mueller, P. G. Vanengen, and K. H. J. Buschow, Phys. Rev. Lett. **50**, 2024 (1983).

[2] R. Kabani, M. Terada, A. Roshko, and J. S. Moodera, J. Appl. Phys. **67**, 4898 (1990).

[3] J. A. Caballero, P. D. Park, A. Cabbibo, J. R. Childress, F. Petroff, and R. Morel, J. Appl. Phys. **81**, 2740 (1997).

[4] D. Ristoiu, J. P. Nozieres, and L. Ranno, J. Magn. Magn. Mater. **219**, 97 (2000).

[5] S. Gardelis, J. Androulakis, J. Giapintzakis, O. Monnereau, and P. D. Buckle, Appl. Phys. Lett. **85**, 3178 (2004).

[6] L. Castellitz, Monatsch. Chem. **82**, 1059 (1951).

[7] R. B. Helmhold, R. A. de Groot, F. M. Mueller, P. G. van Engen, and K. H. J. Buschow, J. Magn. Magn. Mater. **43**, 249 (1984).

[8] J. A. Caballero, W. J. Geerts, J. R. Childress, F. Petroff, P. Galtier, J. U. Thiele, and D. Weller, Appl. Phys. Lett. **71**, 2382 (1997).

[9] C. Hordequin, D. Ristoiu, L. Ranno, and J. Pierre, Eur. Phys. J. B **16**, 287 (2000).

[10] D. Ristoiu, J. P. Nozieres, C. N. Borca, T. Komesu, H. K. Jeong, and P. A. Dowben, Europhys. Lett. **49**, 624 (2000).

[11] D. Ristoiu, J. P. Nozieres, C. N. Borca, B. Borca, and P. A. Dowben, Appl. Phys. Lett. **76**, 2349 (2000).

[12] C. N. Borca, T. Komesu, H. K. Jeong, P. A. Dowben, D. Ristoiu, C. Hordequin, J. Pierre, and J. P. Nozieres, Appl. Phys. Lett. **77**, 88 (2000).

[13] G. L. Bona, F. Meier, M. Taborelli, E. Bucher, and P. H. Schmidt, Solid State Commun. **56**, 391 (1985).

[14] J. Giapintzakis, C. Grigorescu, A. Klini, A. Manousaki, V. Zorba, J. Androulakis, Z. Viskadourakis, and C. Fotakis, Appl. Phys. Lett. **80**, 2716 (2002).

[15] W. R. Branford, S. K. Clowes, Y. V. Bugoslavsky, S. Gardelis, J. Androulakis, J. Giapintzakis, C. E. A. Grigorescu, S. A. Manea, R. S. Freitas, S. B. Roy, and L. F. Cohen, Phys. Rev. B **69**, 201305 (2004).

[16] W. R. Branford, S. K. Clowes, M. H. Syed, Y. V. Bugoslavsky, S. Gardelis, J. Androulakis, J. Giapintzakis, C. E. A. Grigorescu, A. V. Berenov, S. B. Roy, and L. F. Cohen, Appl. Phys. Lett. **84**, 2358 (2004).

[17] J. S. Moodera and D. M. Mootoo, J. Appl. Phys. **76**, 6101 (1994).

[18] M. J. Otto, R. A. M. Vanwoerden, P. J. Vandervalk, J. Wijngaard, C. F. Vanbruggen, and C. Haas, J. Phys.:Condens. Matter **1**, 2351 (1989).

[19] L. Ritchie, G. Xiao, Y. Ji, T. Y. Chen, C. L. Chien, M. Zhang, J. L. Chen, Z. H. Liu, G. H. Wu, and X. X. Zhang, Phys. Rev. B **68**, 104430 (2003).

[20] M. C. Kautzky, F. B. Mancoff, J. F. Bobo, P. R. Johnson, R. L. White, and B. M. Clemens, J. Appl. Phys. **81**, 4026 (1997).

[21] M. C. Kautzky and B. M. Clemens, Appl. Phys. Lett. **66**, 1279 (1995).

[22] P. Turban, S. Andrieu, B. Kierren, E. Snoeck, C. Teodorescu, and A. Traverse, Phys. Rev. B **65**, 134417 (2002).

[23] W. Van Roy, J. De Boeck, B. Brijs, and G. Borghs, Appl. Phys. Lett. **77**, 4190 (2000).

[24] W. Van Roy, G. Borghs, and J. De Boeck, J. Cryst. Growth **227**, 862 (2001).

[25] M. Wojcik, W. Van Roy, E. Jedryka, S. Nadolski, G. Borghs, and J. De Boeck, J. Magn. Magn. Mater. **240**, 414 (2002).

[26] J. Kubler, A. R. Williams, and C. B. Sommers, Phys. Rev. B **28**, 1745 (1983).

[27] S. Ishida, S. Fujii, S. Kashiwagi, and S. Asano, J. Phys. Soc. Jpn. **64**, 2152 (1995).

[28] S. Fujii, S. Ishida, and S. Asano, J. Phys. Soc. Jpn. **64**, 185 (1995).

[29] P. J. Brown, K. U. Neumann, P. J. Webster, and K. R. A. Ziebeck, J. Phys.:Condens. Matter **12**, 1827 (2000).

[30] G. A. de Wijs and R. A. de Groot, Phys. Rev. B **64**, 020402 (2001).

[31] K. A. Kilian and R. H. Victora, J. Appl. Phys. **87**, 7064 (2000).

[32] M. P. Raphael, B. Ravel, M. A. Willard, S. F. Cheng, B. N. Das, R. M. Stroud, K. M. Bussmann, J. H. Claassen, and V. G. Harris, Appl. Phys. Lett. **79**, 4396 (2001).

[33] S. F. Cheng, B. Nadgorny, K. Bussmann, E. E. Carpenter, B. N. Das, G. Trotter, M. P. Raphael, and V. G. Harris, IEEE Trans. Magn. **37**, 2176 (2001).

[34] U. Geiersbach, A. Bergmann, and K. Westerholt, J. Magn. Magn. Mater. **240**, 546 (2002).

[35] S. Kammerer, S. Heitmann, D. Meyners, D. Sudfeld, A. Thomas, A. Hutten, and G. Reiss, J. Appl. Phys. **93**, 7945 (2003).

[36] K. Kim, S. J. Kwon, and T. W. Kim, Phys. Status Solidi B-Basic Res. **241**, 1557 (2004).

[37] T. Ambrose, J. J. Krebs, and G. A. Prinz, Appl. Phys. Lett. **76**, 3280 (2000).

[38] P. J. Webster, J. Phys. Chem. Solids **32**, 1221 (1971).

[39] J. W. Dong, L. C. Chen, C. J. Palmstrom, R. D. James, and S. McKernan, Appl. Phys. Lett. **75**, 1443 (1999).

[40] A. Ayuela, J. Enkovaara, K. Ullakko, and R. M. Nieminen, J. Phys.:Condens. Matter **11**, 2017 (1999).

[41] J. Q. Xie, J. W. Dong, J. Lu, C. J. Palmstrom, and S. McKernan, Appl. Phys. Lett. **79**, 1003 (2001).

[42] P. J. Webster, K. R. A. Ziebeck, S. L. Town, and M. S. Peak, Philos. Mag. B **49**, 295 (1984).

[43] J. Lu, J. W. Dong, J. Q. Xie, S. McKernan, C. J. Palmstrom, and Y. Xin, Appl. Phys. Lett. **83**, 2393 (2003).

[44] Y. Y. Cherkashin, Y. I. Gladyshevskiy, P. I. Kripyakevich, and Y. B. Kuz'ma, J. Inorg. Chem. USSR **3**, 650 (1958).

[45] M. P. Raphael, B. Ravel, Q. Huang, M. A. Willard, S. F. Cheng, B. N. Das, R. M. Stroud, K. M. Bussmann, J. H. Claassen, and V. G. Harris, Phys. Rev. B **66**, 104429 (2002).

[46] B. Ravel, M. P. Raphael, V. G. Harris, and Q. Huang, Phys. Rev. B **65**, 184431 (2002).

[47] F. Y. Yang, C. H. Shang, C. L. Chien, T. Ambrose, J. J. Krebs, G. A. Prinz, V. I. Nikitenko, V. S. Gornakov, A. J. Shapiro, and R. D. Shull, Phys. Rev. B **65**, 174410 (2002).

[48] Y. J. Chen, D. Basiaga, J. R. O'Brien, and D. Heiman, Appl. Phys. Lett. **84**, 4301 (2004).

[49] I. Galanakis, P. H. Dederichs, and N. Papanikolaou, Phys. Rev. B **66**, 174429 (2002).

[50] R. Tickle and R. D. James, J. Magn. Magn. Mater. **195**, 627 (1999).

[51] R. D. James and M. Wuttig, Philos. Mag. A **77**, 1273 (1998).

[52] J. W. Dong, L. C. Chen, J. Q. Xie, T. A. R. Muller, D. M. Carr, C. J. Palmstrom, S. McKernan, Q. Pan, and R. D. James, J. Appl. Phys. **88**, 7357 (2000).

[53] M. S. Lund, J. W. Dong, J. Lu, X. Y. Dong, C. J. Palmstrom, and C. Leighton, Appl. Phys. Lett. **80**, 4798 (2002).

[54] X. Y. Dong, J. W. Dong, J. Q. Xie, T. C. Shih, S. McKernan, C. Leighton, and C. J. Palmstrom, J. Cryst. Growth **254**, 384 (2003).

[55] V. V. Godlevsky and K. M. Rabe, Phys. Rev. B **6313**, 134407 (2001).

[56] M. Genut and M. Eizenberg, Appl. Phys. Lett. **50**, 1358 (1987).

[57] J. L. Hilton, B. D. Schultz, S. McKernan, and C. J. Palmstrom, Appl. Phys. Lett. **84**, 3145 (2004).

[58] C. Hordequin, J. P. Nozieres, and J. Pierre, J. Magn. Magn. Mater. **183**, 225 (1998).

[59] J. A. Caballero, A. C. Reilly, Y. Hao, J. Bass, W. P. Pratt, F. Petroff, and J. R. Childress, J. Magn. Magn. Mater. **199**, 55 (1999).

[60] R. Kelekar and B. M. Clemens, J. Appl. Phys. **96**, 540 (2004).

[61] C. T. Tanaka, J. Nowak, and J. S. Moodera, J. Appl. Phys. **81**, 5515 (1997).

[62] K. Inomata, S. Okamura, R. Goto, and N. Tezuka, Jpn. J. Appl. Phys. **42**, L419 (2003).

[63] K. Inomata, N. Tezuka, S. Okamura, H. Kurebayashi, and A. Hirohata, J. Appl. Phys. **95**, 7234 (2004).

[64] A. Conca, S. Falk, G. Jakob, M. Jourdan, and H. Adrian, cond-mat/0407034 (2004).

[65] H. Kubota, J. Nakata, M. Oogane, Y. Ando, A. Sakuma, and T. Miyazaki, Jpn. J. Appl. Phys. **43**, L984 (2004).

[66] S. Kammerer, A. Thomas, A. Hutten, and G. Reiss, Appl. Phys. Lett. **85**, 79 (2004).

[67] T. Block, C. Felser, G. Jakob, J. Ensling, B. Muhling, P. Gutlich, and R. J. Cava, J. Solid State Chem. **176**, 646 (2003).

[68] H. Takahashi, S. Soeya, J. Hayakawa, K. Ito, A. Kida, C. Yamamoto, H. Asano, and M. Matsui, J. Appl. Phys. **93**, 8029 (2003).

[69] S. van Dijken, X. Fain, S. M. Watts, K. Nakajima, and J. M. D. Coey, J. Magn. Magn. Mater. **280**, 322 (2004).

[70] S. van Dijken, X. Fain, S. M. Watts, and J. M. D. Coey, Phys. Rev. B **70**, 052409 (2004).

[71] M. Julliere, Phys. Lett. A **54**, 225 (1975).

[72] I. Galanakis, J. Phys.:Condens. Matter **14**, 6329 (2002).

[73] J. Schmalhorst, S. Kammerer, G. Reiss, and A. Hutten, Appl. Phys. Lett. **86**, 052501 (2005).

[74] J. Schmalhorst, S. Kammerer, M. Sacher, G. Reiss, A. Hutten, and A. Scholl, Phys. Rev. B **70**, 024426 (2004).

"Lack of money is no obstacle. Lack of an idea is an obstacle."

Ken Hakuta.

Chapter 7

Highly oriented (110) thin films of Co_2MnSi on a-plane Al_2O_3

From the experience gained in growing binary intermetallic compounds from single, elemental targets (Chapter 5), we move onto a more complicated system: the Heusler alloy, Co_2MnSi. This ternary intermetallic was grown from three, elemental targets onto a-plane sapphire by dc magnetron co-sputtering.

7.1 Introduction

In the previous section it was noted that films sputter deposited from a single stoichiometric target were deficient in Si and this deviation from the ideal stoichiometry resulted in a reduced M_s.[1] Therefore, in this chapter the focus is on achieving stoichiometric films by co-sputtering elemental targets. The overall composition of the film can then be varied by adjusting the power supplied to each target. In the following chapters a stoichiometric film is defined as a film within 0.4 at. % of the desired stoichiometry. The substrate chosen to carry out this preliminary optimisation and characterisation of Co_2MnSi was required to not contain any of the elements that were present in the film, otherwise it would not be possible to carry out the EDS analysis accurately. The substrate also needs to be insulating for some of the transport measurements. Sapphire a-plane met the above requirements and is readily available. It has a rhombohedral structure (a=4.754 Å, c=12.982 Å) and the a-plane is $(11\bar{2}0)$ as depicted in Fig. 7.1.

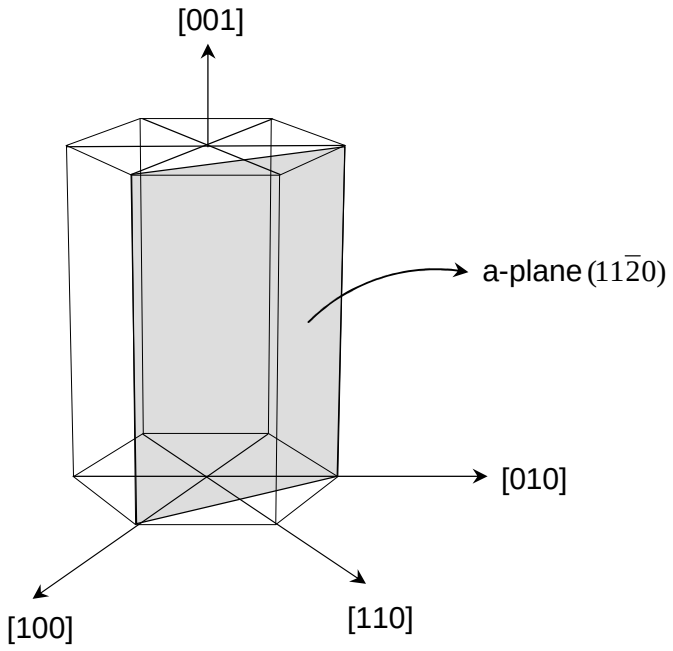

Fig. 7.1. Schematic illustrating the a-plane of sapphire.

7.2 Film preparation and deposition

Thin films of Co_2MnSi were grown by dc magnetron co-sputtering from three, elemental targets onto an array of a-plane sapphire substrates. The UHV sputtering system described in section 3.2.2. was used. Mn has a large coefficient of thermal expansion, so it was not possible to secure the sputtering target using metallic fastenings. It was glued to a thin copper sheet (non-magnetic

to prevent shielding of the magnetic field) using silver loaded epoxy. The copper sheet was designed with flaps that had several holes enabling secure fastening with screws to the sides of the magnetron. Prior to loading, the substrates were cleaned in acetone and isopropanol. The three elemental targets were arranged in a triangular configuration and the substrates were located directly below these on a Ta strip heater (Fig. 3.5c). This geometry enabled a range of compositions to be obtained in one deposition sequence. The target-substrate distance varied between 111 and 116 mm (measured from the centre of each target to the substrate position that gives the desired stoichiometry). This enabled a range of compositions to be attained on the array of substrates, but small variation across each substrate (4x9 mm^2). The base pressure of the system was $2x10^{-7}$ Pa and the argon pressure during the film deposition was 3.20 Pa. Films in the thickness range 300-400 nm were grown and the deposition rate was 0.10 nm/s. The depositions were carried out at a range of substrate temperatures from 545 to 715 K. Film compositions were determined by EDS in a SEM with a relative precision of 1.5 %.

7.3 Structural Characterisation

Structural characterisation was performed by x-ray diffraction using Cu Kα radiation. The XRD pattern of a 400 nm, stoichiometric film is shown in Fig. 7.2(a). This film is single phase and all diffraction peaks can be attributed to the Co_2MnSi $L2_1$ structure, apart from some weak, broad peaks at 20 and 60 °2θ (from the substrate) and sharp lines, which are W contamination lines from the X-ray tube. This was confirmed from an XRD pattern of a bare substrate (Fig. 7.3). The film is polycrystalline but has a strong (110) texture. This is in agreement with the literature, since polycrystalline films were always obtained if a buffer layer was not used.[1-4] In fact Kämmerer *et al.*[3] found that polycrystalline growth was observed at high substrate temperatures (~724 K), independent of the nature and orientation of the substrate. By using the sapphire peaks for reference, the out-of-plane lattice parameter was found to be 5.634 Å, which is less than the bulk value of 5.654 Å.[5] This is in agreement with the proposed growth orientations between the substrate (s) and film (f); $[001]_s//[001]_f$ and the $[110]_s//[110]_f$ which leads to a mismatch of about 13 % in the former orientation and 3 % in the latter. This large mismatch results in a tensile stress in the film plane, hence a compressive stress out-of-plane and so one would expect a smaller out-of-plane lattice parameter. In the literature there have been no reports of well oriented films on a-plane sapphire without a buffer layer. However, with a V underlayer epitaxial films were obtained but with a larger lattice parameter than the bulk of 5.688 Å.[1] In this thesis such metallic underlayers were not used, to avoid any possible interdiffusion between the underlayer and the Co_2MnSi.

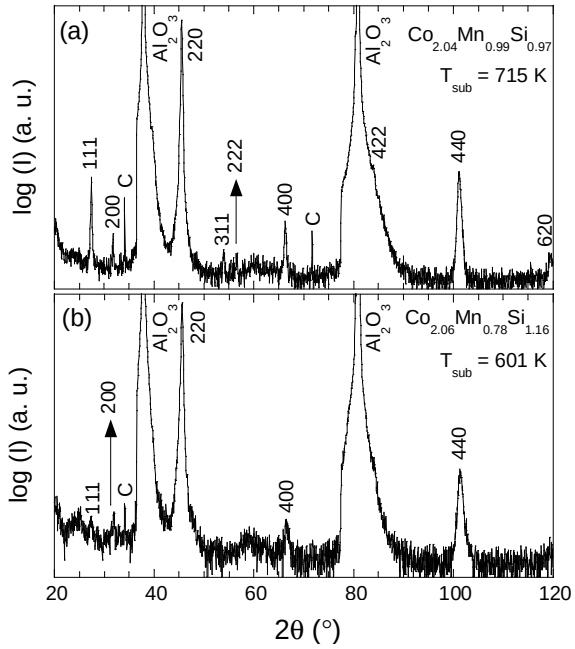

Fig. 7.2. XRD patterns of (a) stoichiometric and (b) off-stoichiometric film. The sharp lines labelled C, are W contamination lines from the X-ray tube and the weak, broad peaks at 20 and 60 °2θ were also observed on a bare substrate. (A nickel filter was used to prevent saturation of the detector, which accounts for the shape of the substrate peaks).

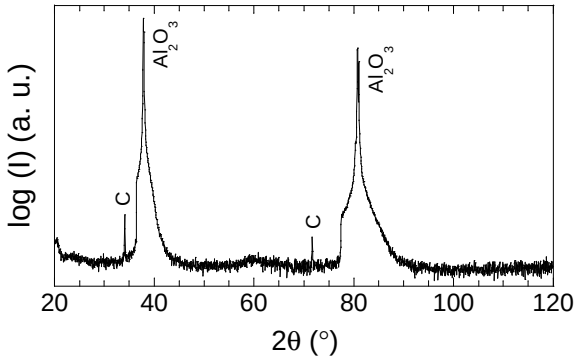

Fig. 7.3. XRD pattern of a bare substrate of a-plane sapphire (A nickel filter was used to prevent saturation of the detector, which accounts for the shape of the substrate peaks).

7.3.1 Effect of Composition

Ordering of the Mn and Si sublattices is indicated by the presence of the (111) superlattice diffraction peak, so it is of interest that in a series of films (growth temperature, 601 K and thickness, 300 nm, constant) in which the overall deviation from the desired stoichiometry is increased (by adjusting the ratio of the power to the targets), the (220):(111) XRD peak intensity

ratio increases. When the Mn/Si ratio is 0.67 ($Co_{2.06}Mn_{0.78}Si_{1.16}$) the (111) reflection is very weak and it is this trace that is shown in Fig. 7.2(b).

7.3.2 Effect of Film Thickness

The XRD patterns of a series of stoichiometric films of different thickness grown at 602 K are shown in Fig. 7.4. As the film thickness decreases, the (220):(111) XRD peak intensity ratio increases. This suggests that the film is becoming more disordered as the film thickness decreases, indicative of a disordered interface phase. However, the increase in the (220):(422) XRD peak intensity ratio and the decrease of the (220):(440) XRD peak intensity ratio also indicates an increase in the (110) texture.

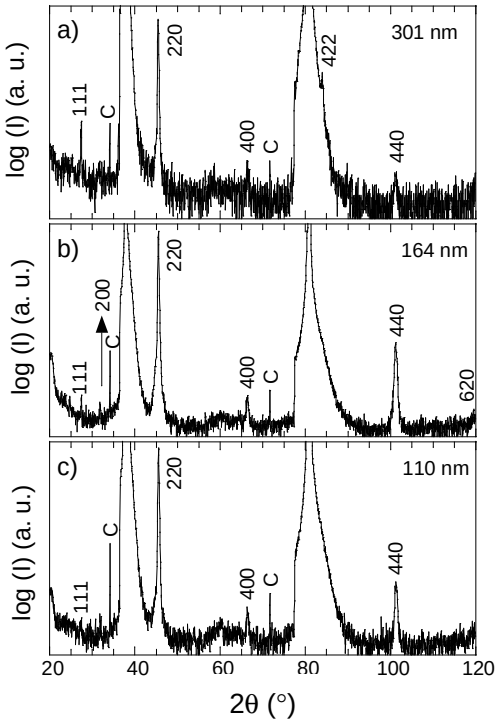

Fig. 7.4. XRD patterns of stoichiometric films grown at T_{sub} of 602 K. (The sharp lines labelled C, are W contamination lines from the X-ray tube and the weak, broad peaks at 20 and 60 °2θ were also observed on a bare substrate).

7.3.3 Effect of deposition temperature

T_{sub} also affects the film texture, as shown in Fig. 7.5 for a series of 400 nm, stoichiometric films. As T_{sub} increases, the films becomes more (110) textured, the most notable change being an increase of the (220):(422) ratio. The (220):(111) ratio also increases but only between 617 K and 715 K.

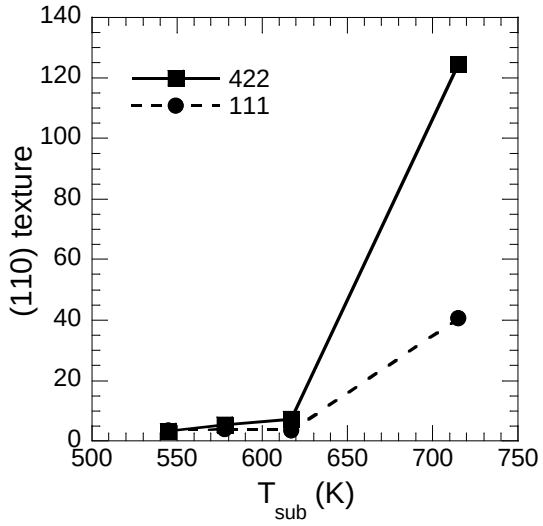

Fig. 7.5. (220):(422) XRD peak intensity ratio and (220):(111) ratio for a series of 400 nm, stoichiometric films.

7.4 Magnetic Characterisation

7.4.1 Determination of M_s

In addition to EDS and XRD, M_s also provides a good indication of the stoichiometry of the film. M_s was determined from in-plane hysteresis loops measured in both a VSM and SQUID at 10 K; for stoichiometric films M_s was 1007 ± 50 emu/cc (4.95 ± 0.25 μ_B/formula unit), which agrees well with the bulk value of 5.1 μ_B/formula unit.[6] A 3 % decrease in M_s was observed on increasing the temperature to 300 K. This small dependence of M_s on T is due to the high Curie temperature of this alloy. In bulk form this alloy has a T_c of 985 K,[7] which is the highest of the known Heuslers. In thin film form, a T_c of 950 K was obtained (Fig. 7.6), which is in agreement with the films grown by Kim *et al.*[4] although they obtained this value with extrapolation from 800 K. Cheng *et al.*[6] found a variation in T_c for the different bulk samples of Co_2MnSi (charge, boule, annealed boule and remaining melt) but not for Co_2MnGe. This suggested that Co_2MnGe is a stoichiometric compound but Co_2MnSi has a composition range in agreement with the Co-Mn-Si phase diagram. Therefore, the discrepancy of the T_c is probably due to the composition variation in Co_2MnSi. Ido and Yasuda[8] found that T_c decreases with increasing Co concentration in $Co_{2-x}Mn_{1+x}Si$, which would imply that the film measured in Fig. 7.6 had an excess of Co (although this disagrees with EDS measurements). However, Dong *et al.*[9] observed a reduced T_c in thin films of Ni_2MnGa and attributed this to the difference in structure of the film (tetragonal) compared to the bulk ($L2_1$ phase). Although thin films in this work do have the $L2_1$ structure, they are strained and so this could be the reason for the reduced T_c.

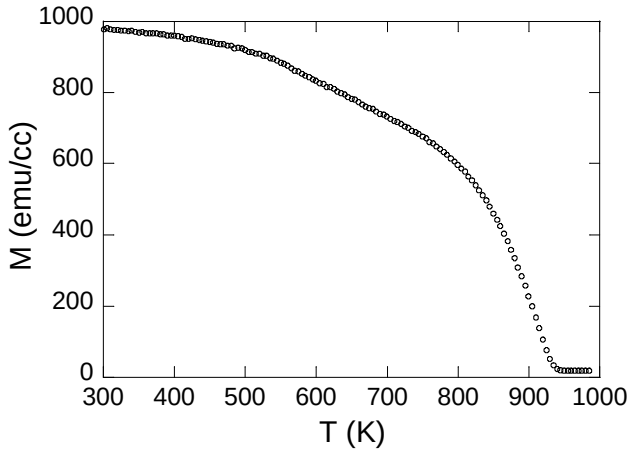

Fig. 7.6. Temperature dependence of the magnetisation for a 300 nm, stoichiometric film.

7.4.2 Dependence of H_c on T_{sub}

For a series of 400 nm, stoichiometric films, H_c was found to decrease with increasing T_{sub} as shown in Fig. 7.7, reaching the lowest value of 18 Oe at 715 K. An increase in T_{sub} from 545 to 715 K results in a reduction in H_c by a factor of three (M_s is a constant in these films). The change in coercivity is crystallographic and/or microstructural in origin: both grain size and degree of (110) texturing increase as T_{sub} increases. H_c correlates strongly with the change in film texture (inset to Fig. 7.7). As T_{sub} increases, the (422) peak decreases relative to the (220) peak and H_c decreases.

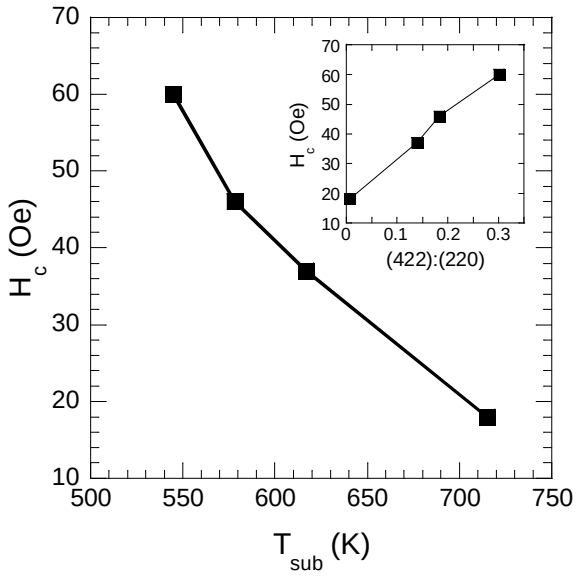

Fig. 7.7. H_c vs. T_{sub} for a series of 400 nm, stoichiometric films. The inset shows H_c vs. (422):(220) for these four films.

7.4.3 Dependence of M_s on d

The methods used so far to check the stoichiometry of the films have averaged the entire film, although XRD patterns of thinner films (Fig. 7.4) indicated the presence of a disordered interface phase. This is supported by the observation of a decrease in M_s with decreasing thickness for a series of films grown at T_{sub} of 602 K (Fig. 7.8). M_s decreases by about 25 % as the film thickness decreases from 400 to 110 nm. This indicates that thinner films are disordered, due to the absence of lattice matching between the film and substrate.

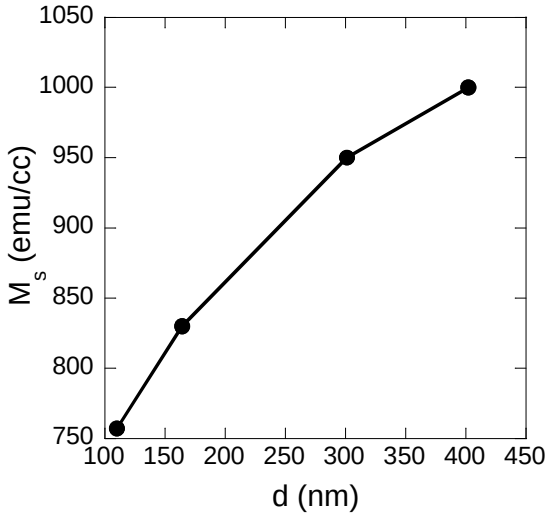

Fig. 7.8. The effect of film thickness on M_s for a series of stoichiometric films grown at 602 K.

7.5 Transport measurements

7.5.1 Dependence of ρ on T_{sub}

Transport measurements were carried out from 4.2 to 295 K using a standard DC 4-point geometry. For a series of 400 nm, stoichiometric films, ρ decreased with increasing T_{sub} as shown in Fig. 7.9. The lowest $\rho_{4.2\ K}$ measured of 47 μΩcm is reached at 715 K, and this $\rho_{4.2\ K}$ is about half that obtained in the literature[1,3] with the exception of Raphael *et al.*[2] who obtained 16 μΩcm at 773 K ($\rho_{4.2\ K}$ is 4 μΩcm for bulk single crystal).[6] The inset to Fig. 7.9 b) shows the resistivity ratio, RR ($\rho_{295\ K}/\rho_{4.2\ K}$) increasing with increasing T_{sub}, reaching a maximum of 1.41 at 715 K. This is a relatively low value for a metallic alloy film (RR of bulk single crystal is also low, 6.5)[6] but is comparable to the literature where values in the range 1.2-1.4 are reported.[1-4] Low values of RR indicate the dominance of defect scattering.

The reduction in ρ with increasing T_{sub} is most likely due to an increase in grain size and hence a reduction in grain boundary scattering. As T_{sub} increases from 545 to 715 K the surface features (which reflect the grain size) observed in a FEG-SEM increase from about 70 to 130 nm, and $\rho_{4.2\ K}$ is halved (102 to 47 μΩcm). It is evident from Fig. 7.10 that there is not only a change in the size of the features, but also in shape; there is a change from triangular to a denser, globular structure as the temperature is increased.

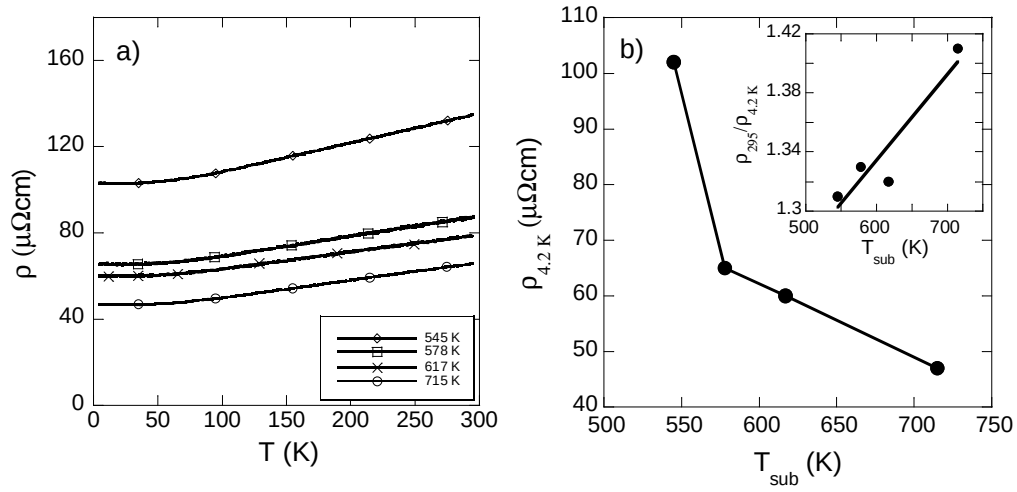

Fig. 7.9. Transport measurements on 400 nm stoichiometric films. a) ρ vs T for 4 films grown at different T_{sub}. b) $\rho_{4.2\ K}$ vs T_{sub} for these 4 films. The inset shows the resistivity ratio ($\rho_{295}/\rho_{4.2\ K}$) vs T_{sub}.

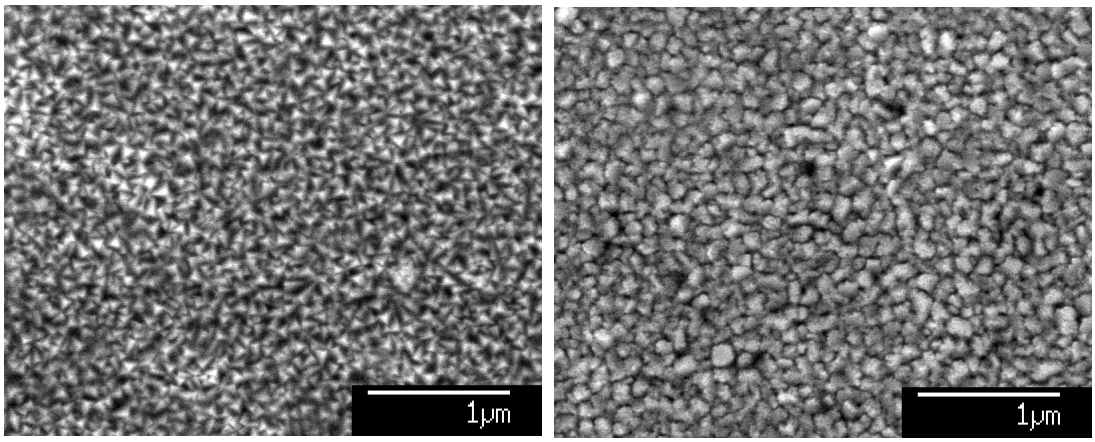

Fig. 7.10. FEG-SEM images of 400 nm, stoichiometric films grown at T_{sub} of a) 545 K and b) 715 K.

7.5.2 Dependence of ρ on d

$\rho_{4.2\ K}$ decreases with increasing film thickness (Fig. 7.11). This can be attributed to the reduction in grain boundary scattering: surface feature size increases from about 20 to 70 nm as the film thickness increases from 110 to 300 nm. Thinner films also show a stronger (110) texture.

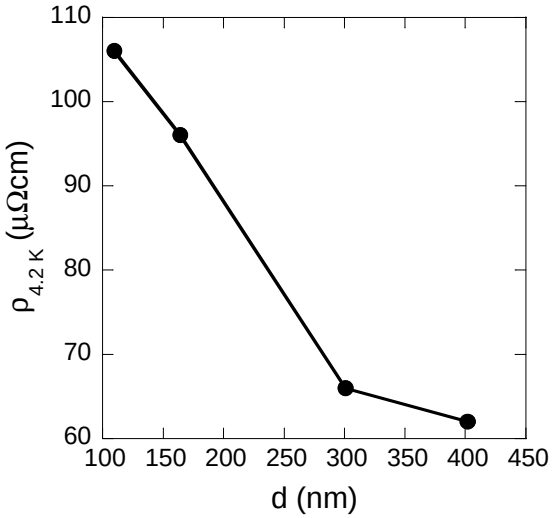

Fig. 7.11. The effect of film thickness on $\rho_{4.2\ K}$ for a series of stoichiometric films grown at 602 K.

7.5.3 Dependence of ρ on T

The lowest ρ-T curve shown in Fig. 7.9a) is typical for a relatively thick (>300 nm), stoichiometric film. This curve was fitted as shown in Fig. 7.12. In the temperature range 295 to 100 K, ρ decreased linearly with temperature. This differs from transport measurements carried out on a bulk NiMnSb polycrystal by Hordequin *et al.*[10] who reported a $T^{1.35}$ law and from Ambrose *et al.*[11] who investigated single-crystal films of Co_2MnGe and observed a $T^{1.5}$ dependence.

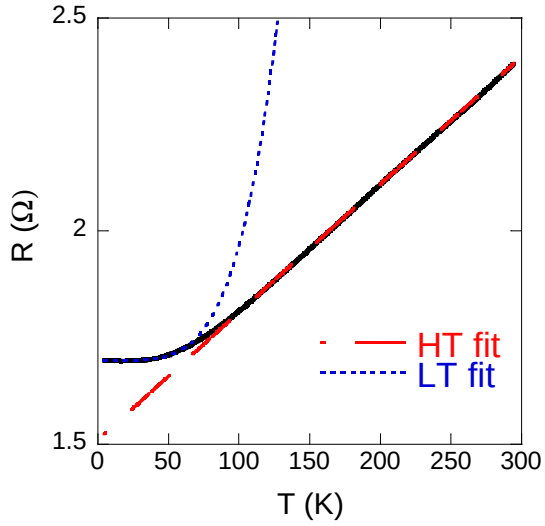

Fig. 7.12. ρ-T curve for a 400 nm, stoichiometric film grown at T_{sub} of 715 K (black line). The dashed, coloured lines show the low and high temperature fit.

However, not all films studied show linear behaviour and as the compositions become more off-stoichiometric, the non-linearity becomes more pronounced. This is illustrated in Fig. 7.13 for an off-stoichiometric film along with the curve of the stoichiometric film shown in Fig. 7.12 for comparison (the XRD patterns of both these films were shown in Fig. 7.2).

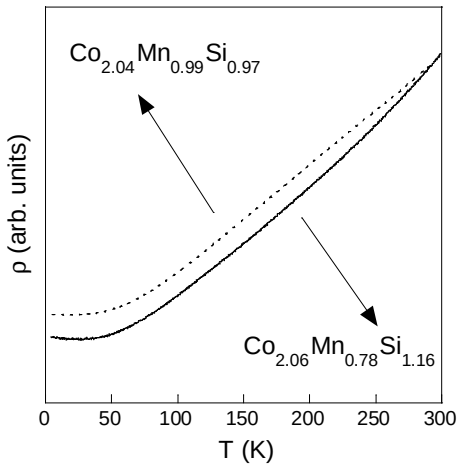

Fig. 7.13. ρ-T curves of a stoichiometric (dashed line) and off-stoichiometric film (solid line). For display purposes the curves have been translated along the y-axis to coincide at 295 K.

Below 100 K there is a change in the resistivity behaviour, and a $T^2 + T^{9/2}$ behaviour is observed in the stoichiometric film. The $T^{9/2}$ term is attributed to two-magnon scattering, which is the first available magnetic scattering process for a HMF.[12] The T^2 term results either from one magnon scattering or from electron-electron scattering.[13] In a HMF, one magnon scattering cannot occur at low temperature because there are no states at E_F into which the electron can be scattered. Therefore, if these films are truly HMF then the T^2 term must arise from electron-electron scattering. Below about 20 K, ρ shows no temperature dependence. However, for NiMnSb, Hordequin *et al.*[10] observed a T^2 dependence below 50 K for the bulk polycrystal and Moodera *et al.*[14] observed a linear dependence with T below 15 K for a polycrystalline film. In the case of the full Heusler alloys, Lund *et al.*[15] observed a $T^{1/2}$ dependence below 20 K for epitaxial films of Ni_2MnGe and Ambrose *et al.*[11] found that ρ was nearly independent of T below 50 K for single-crystal films of Co_2MnGe. The different behaviours observed could be material dependent, but are also dependent upon fabrication parameters (different behaviour is observed even for the same alloy), as different crystallography and microstructure will result in different ρ-T behaviours.

7.5.4 Effect of *d* and composition on the low temperature ρ-*T* behaviour

For a 300 nm, stoichiometric film the resistivity is temperature independent below ~20 K, but as the film thickness decreases an upturn in the resistivity at low temperatures is observed for a 164 nm film and becomes more pronounced in a 110 nm film (Fig. 7.14).

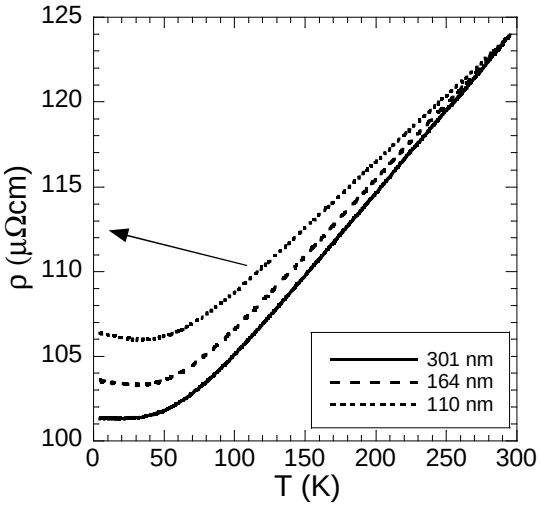

Fig. 7.14. ρ-*T* curves for stoichiometric films of different thickness, grown at the same deposition temperature of 602 K. For display purposes the curves have been translated along the y-axis to coincide at 295 K. The vertical axis corresponds to the 110 nm film. $\rho_{295\ K}$ are 89, 117, and 124 μΩcm and $\rho_{4.2\ K}$ are 66, 96, and 106 μΩcm for the 300, 164 and 110 nm films respectively.

Such upturns are also observed in off-stoichiometric films. Figure 7.15 illustrates this for three, 400 nm thick films. These films were grown at different temperatures, so cannot be directly compared but do show the range of low temperature behaviours that can occur. An upturn is observed in the cobalt deficient film. Such an upturn has been reported previously in Ni_2MnGe at 20 K by Lund *et al.*[15] and in Co_2MnSi at 40 K by Geiersbach *et al.*[1] The upturn is interpreted as weak localisation[15] due to electron interaction effects, arising in this case from disordered material, consistent with the decrease in M_s. As noted above, in the case of the stoichiometric film the resistivity is temperature independent below ~20 K. In the film with an excess of cobalt the curve has a positive slope. These three types of behaviour have been observed in other films studied, with the most extreme examples presented here. The Mn and Si content are not a constant in these films, so we cannot make any quantitative comments, but as the films become richer in cobalt, dρ/dT for the high temperature regime increases, consistent with a reduced number of scattering centres.

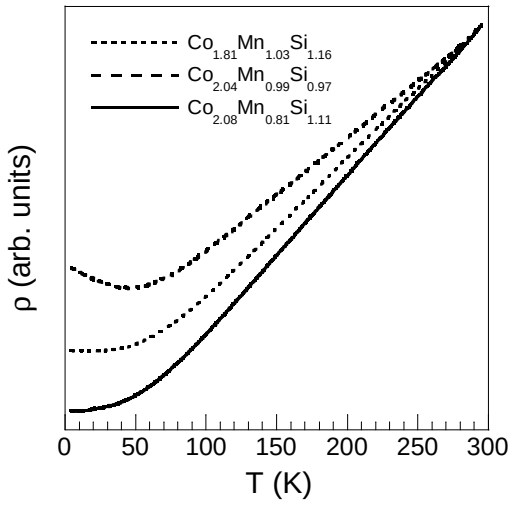

Fig. 7.15. ρ-T curves of three, 400 nm films of different compositions. For display purposes the curves have been translated along the y-axis to coincide at 295 K. The middle curve is the optimised, stoichiometric film ($\rho_{295\ K}$ = 66 μΩcm), the top curve is Co deficient ($\rho_{295\ K}$ = 160 μΩcm) and the bottom curve has an excess of Co ($\rho_{295\ K}$ = 79 μΩcm).

7.5.5 Surface polarisation[1]

The spin polarisation of the transport current, P_t was measured by point contact Andreev reflection[2,19] between Nb cut tips and the Heusler film at 4.2 K. The normalised conductance vs voltage curves were fitted to the Mazin model in the ballistic regime,[169] to determine P_t and the effective tunnel barrier height, Z. The barrier may arise due to the combined effects of surface contamination or disorder, Fermi velocity mismatch in the two materials and interface scattering. Experimentally, Z can be varied to a certain extent by changing the tip pressure (Z=0 corresponds to a clean interface and is obtained at higher pressure). The variation of P_t with Z for a 400 nm film grown at 715 K is shown in Fig. 7.16. At Z=0, P_t~54 ± 3 %, consistent with measurements on bulk single crystals of Co_2MnSi.[6,17] However, for the thinnest film (110 nm) it was only possible to obtain contacts with high values of Z. One data point for this film is shown for comparison. The larger error bars reflect the fact that in this Z range the fitting is less reliable. Nevertheless the polarisation is depressed in the thinner film within the error of our measurement. As the surface quality of all the films is similar, the non-vanishing barrier in the 110 nm film suggests that the intrinsic properties of this film are different from the others – in line with the transport and magnetisation data taken on this film. Further investigation is needed to gain a detailed understanding of the processes involved in Andreev reflection in the thinnest film.

[1] Carried out by Y. Miyoshi and Y. Bugoslavsky at the Blackett Laboratory, Imperial College

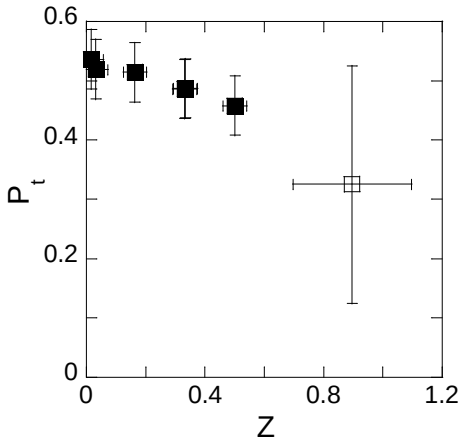

Fig. 7.16. The variation in P_t with Z for a stoichiometric, 400 nm film grown at 715 K (filled squares) and the 110 nm film (open square).

Fig. 7.17 shows P_t data for three films of different composition. Within the experimental error, P_t is the same over the range of Z values that are accessible. This means that the measurement is not sensitive to the difference in bulk stoichiometry: either the polarisation is the same within the experimental error for all films, or the measurement is dominated by surface effects, and the films undergo a surface reconstruction that is not influenced by this difference in stoichiometry.

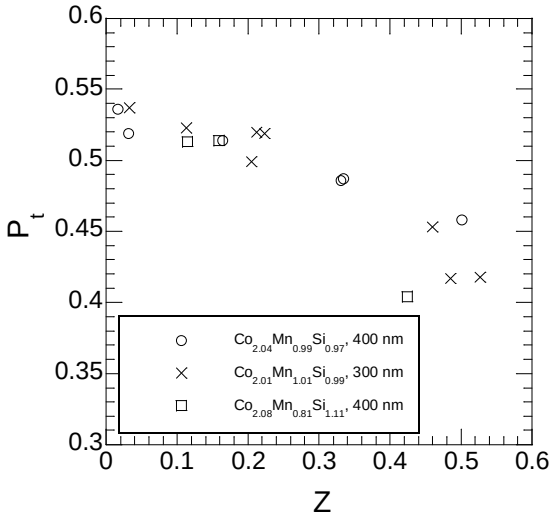

Fig. 7.17. Variation in P_t with Z as determined by the Mazin procedure for three different films.

7.6 Summary

Thin films of Co_2MnSi have been grown from three single elemental targets on a-plane sapphire substrates by dc magnetron co-sputtering. Stoichiometric films were single phase and highly textured, without the use of a seed layer. They exhibited the bulk value of M_s and films grown at the highest T_{sub} (715 K) showed the lowest resistivity (47 μΩcm at 4.2 K) and the lowest coercivity (18 Oe). P_t of a 400 nm film grown at this deposition temperature was 54 %. Within the ranges explored in this study changes in T_{sub} and stoichiometry have been found to affect crystallographic alignment, bulk magnetic properties and electrical transport behaviour of these films, but not P_t. A decrease in M_s with decreasing film thickness and the different transport behaviour of thinner films indicates a graded disorder, which is significant even at a thickness of 110 nm. By growing on GaAs(001), which has a similar lattice parameter to Co_2MnSi it is expected that this disordered region will be confined to the first few atomic layers. This is discussed in the following chapter.

References

[1] U. Geiersbach, A. Bergmann, and K. Westerholt, J. Magn. Magn. Mater. **240**, 546 (2002).

[2] M. P. Raphael, B. Ravel, M. A. Willard, S. F. Cheng, B. N. Das, R. M. Stroud, K. M. Bussmann, J. H. Claassen, and V. G. Harris, Appl. Phys. Lett. **79**, 4396 (2001).

[3] S. Kammerer, S. Heitmann, D. Meyners, D. Sudfeld, A. Thomas, A. Hutten, and G. Reiss, J. Appl. Phys. **93**, 7945 (2003).

[4] K. Kim, S. J. Kwon, and T. W. Kim, Phys. Status Solidi B-Basic Res. **241**, 1557 (2004).

[5] P. J. Webster and K. R. A. Ziebeck. (Springer, Berlin, 1988).

[6] S. F. Cheng, B. Nadgorny, K. Bussmann, E. E. Carpenter, B. N. Das, G. Trotter, M. P. Raphael, and V. G. Harris, IEEE Trans. Magn. **37**, 2176 (2001).

[7] P. J. Brown, K. U. Neumann, P. J. Webster, and K. R. A. Ziebeck, J. Phys.:Condens. Matter **12**, 1827 (2000).

[8] H. Ido and S. Yasuda, J. de Physique **C8**, 141 (1988).

[9] J. W. Dong, L. C. Chen, C. J. Palmstrom, R. D. James, and S. McKernan, Appl. Phys. Lett. **75**, 1443 (1999).

[10] C. Hordequin, D. Ristoiu, L. Ranno, and J. Pierre, Eur. Phys. J. B **16**, 287 (2000).

[11] T. Ambrose, J. J. Krebs, and G. A. Prinz, Appl. Phys. Lett. **76**, 3280 (2000).

[12] K. Kubo and N. Ohata, J. Phys. Soc. Jap. **33**, 21 (1972).

[13] M. J. Otto, R. A. M. Vanwoerden, P. J. Vandervalk, J. Wijngaard, C. F. Vanbruggen, and C. Haas, J. Phys.:Condens. Matter **1**, 2351 (1989).

[14] J. S. Moodera and D. M. Mootoo, J. Appl. Phys. **76**, 6101 (1994).

[15] M. S. Lund, J. W. Dong, J. Lu, X. Y. Dong, C. J. Palmstrom, and C. Leighton, Appl. Phys. Lett. **80**, 4798 (2002).

[16] I.I. Mazin, A.A. Golubov, and B. Nadgorny, J. Appl. Phys. **89**, 7576 (2001).

[17] L. Ritchie, G. Xiao, Y. Ji, T. Y. Chen, C. L. Chien, M. Zhang, J. L. Chen, Z. H. Liu, G. H. Wu, and X. X. Zhang, Phys. Rev. B **68**, 104430 (2003).

"Water which is too pure has no fish."
Ts'ai Ken T'an.

Chapter 8

Highly oriented (001) thin films of Co_2MnSi on GaAs(001)

In this chapter we investigate the growth of the Heusler alloy Co_2MnSi on a lattice matched and technologically important substrate, GaAs(001).

8.1 Introduction

In the previous chapter it was shown that growth of Co_2MnSi on a-plane sapphire resulted in highly textured (110) films. However, there appeared to be a disordered interface region, which we assumed was because of the large lattice mismatch. It is expected that this disordered region will be confined to the first few atomic layers by growing onto a lattice matched substrate. GaAs is cubic, a=5.6538 Å, which means that the mismatch with Co_2MnSi is negligible (0.004 %). Good quality growth of this alloy on GaAs would mean that it would be very promising as a contact for the injection of electron spin into semiconductors.

8.2 Film preparation and deposition

Thin films of Co_2MnSi were grown from three elemental dc magnetron sputtering targets onto GaAs(001) substrates (4×4 mm^2) positioned directly below the targets on a Ta strip heater. The geometry of the set-up and sputtering parameters are described in section 7.2. Prior to loading into the vacuum system, the GaAs substrates were chemically cleaned in an ultrasonic bath for 10 min using an organic alkali followed by 2 min in distilled water. The substrates were annealed in situ at 868 K for 10 min to remove the native oxide and to obtain the 4×2 surface reconstruction.[1] The temperature was then lowered to 653 K and the system was pumped for 90 mins to ensure complete removal of As, since Mn_2As forms readily at the growth temperature. The temperature was then set to the growth temperature (T_{sub}), which ranged from 620 to 689 K, and 20 mins were allowed for temperature stabilisation.

8.3 Structural Characterisation

8.3.1 XRD

The XRD pattern of a 300 nm stoichiometric film grown at T_{sub} of 647 K is shown in Fig. 8.1b. The (002), (004) and (006) peaks from the GaAs substrate can be clearly seen but only very weak peaks from the Co_2MnSi phase. The ordinate is presented as a log scale so that these weak peaks from the Heusler layer (which suggest mixed orientation material) can also be seen. The sharp line, around 60 °2θ is a W contamination line from the X-ray tube, confirmed from an XRD pattern of a bare substrate (Fig. 8.2). The weak line just below 45 °2θ is a multiple reflection appearing at GaAs(00$\frac{8}{3}$) and this along with the contamination line have also been observed on a bare substrate of GaAs(001) by Van Roy *et al.*[2] High resolution XRD work revealed the presence

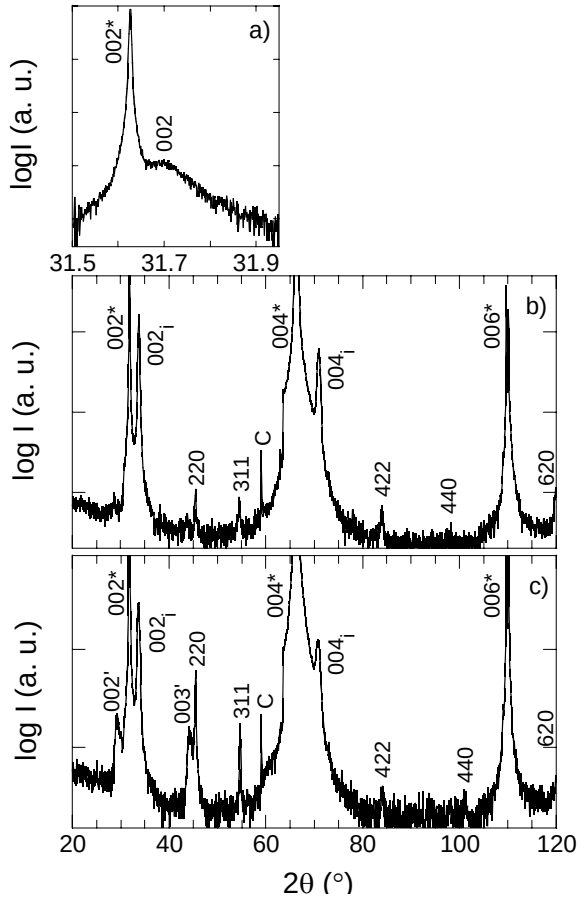

Fig. 8.1. XRD patterns of stoichiometric, 300 nm films a) High resolution diffraction pattern showing the (002) Co_2MnSi peak to the right of the GaAs(002) peak, b) film grown with the 90 mins pumping stage and c) without pumping stage. Diffraction peaks labelled with * denote substrate peaks, 'i' are interface peaks and ′ indicate Mn_2As. The sharp lines indexed with a C, are W contamination lines from the X-ray tube. (A nickel filter was used to prevent saturation of the detector, which accounts for the shape of the substrate peaks).

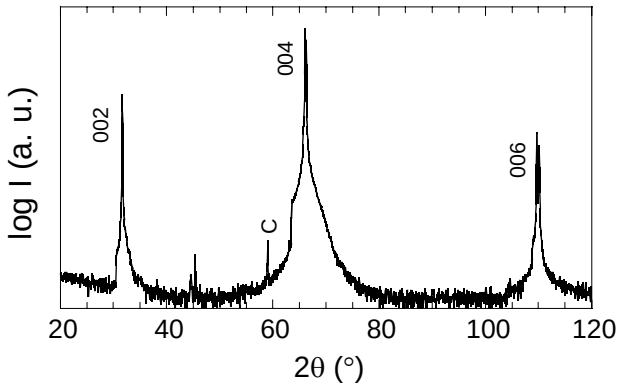

Fig. 8.2. XRD pattern of a bare substrate of GaAs(001) (A nickel filter was used to prevent saturation of the detector, which accounts for the shape of the substrate peaks).

of the expected (002) and (004) Co_2MnSi peaks, only visible as a shoulder to the right of the GaAs peaks due to the very low mismatch between the Heusler and the substrate (Fig. 8.1a). Therefore,

the Heusler layer is growing with a strong (001) texture, following the orientation of the substrate, but is not growing fully epitaxially. The out of plane lattice parameter of the Co_2MnSi was found to be 5.638 Å, which is similar to the 5.634 Å obtained on non-lattice matched a-plane sapphire (section 7.3). In addition, intense (002) and (004) peaks are observed originating from an interfacial reaction zone between the substrate and the Co_2MnSi, as has been confirmed by high resolution TEM (outlined in the next section). This reaction zone is epitaxial, and by using the GaAs peaks for reference, the out-of-plane lattice parameter was found to be 5.312 Å. Therefore, this reaction zone interferes with the lattice matching of the Co_2MnSi to the GaAs and the subsequent epitaxial growth. A sample grown without the 90 mins pumping stage following substrate annealing showed the presence of Mn_2As (Fig. 8.1c). This phase has also been observed in thin films of NiMnSb on GaAs(001).[2] Mn is reactive on a GaAs surface and tends to replace the Ga-As bond by Mn-As.[3] There is As remaining in the chamber after the substrate anneal and also As in the substrate starts to out-diffuse at around 650 K. Therefore, Mn_2As formation was reduced by firstly annealing the GaAs substrate (to achieve the 4×2 reconstruction in order to obtain a Ga rich surface) and secondly pumping the chamber for 90 mins to reduce the As background.

8.3.2 TEM[1]

TEM investigations were carried out in a JEOL JEM-3000F FEG TEM, operated at 300 kV and sample preparation was carried out using a focussed ion beam microscope (FIB). Fig. 8.3(a) shows a bright-field (BF) cross section TEM micrograph of an 80 nm film, which has been oriented to the $[1\bar{1}0]$ zone axis. This consists of (I) columnar grains of the Heusler $L2_1$ structured Co_2MnSi with a strong texture, and (II) a dark contrast region extending up to approximately 20 nm into the GaAs substrate. Phase contrast images of region II showed the same crystallographic symmetry as the GaAs substrate, with a lower degree of order. A second film grown under identical conditions (a_1) shows similar regions but is overall of a better quality. The TEM sample preparation can partly account for this but there must also be some variation in the growth conditions. Variation in growth temperature is the most likely and could explain why the surface of the Heusler in (a_1) is much smoother that the surface of (a) (top of the columns are not as faceted in a_1). For the film shown in (a_1) a fast Fourier transform (FFT) of region II (see 8.6f) overlaps well with the FFT for the GaAs, possessing the same crystallographic symmetry, although the diffraction spots are not as well defined. In particular there is streaking along the 002 direction (discussed later). At the interface between regions I and II, there is a thin interlayer (2-3 nm), which appears sharp and flat (marked with an arrow). Energy filtered TEM maps of Mn (L_3 640 eV edge), Ga (L_3 1115 eV edge), Co (L_3 779 eV edge), and As (L_3 1323 eV edge) are shown

[1] Carried out by A. Kohn at the Department of Materials, University of Oxford

in Figs. 8.3(b)-(e), respectively. Bright regions correspond to higher concentration of the mapped element. Si maps were not obtained due to the proximity of the Ga M and Si L lines. Mn is detected in regions corresponding to I and II in the BF image, while a region depleted of Mn correlates with the thin interlayer. Ga is detected in the substrate, is depleted in region II, and appears enriched in the interlayer. The Co map shows a flat interface at the bottom of the interlayer. Profile maps indicate a possible increase in the Co concentration in the thin interlayer (Fig. 8.4). In both the Mn and Co map, the intensity variations within the Heusler layer are the result of diffraction effects, as can be seen from the correlation between these maps and the BF image. The As map shows a flat interface with no apparent diffusion into the film.

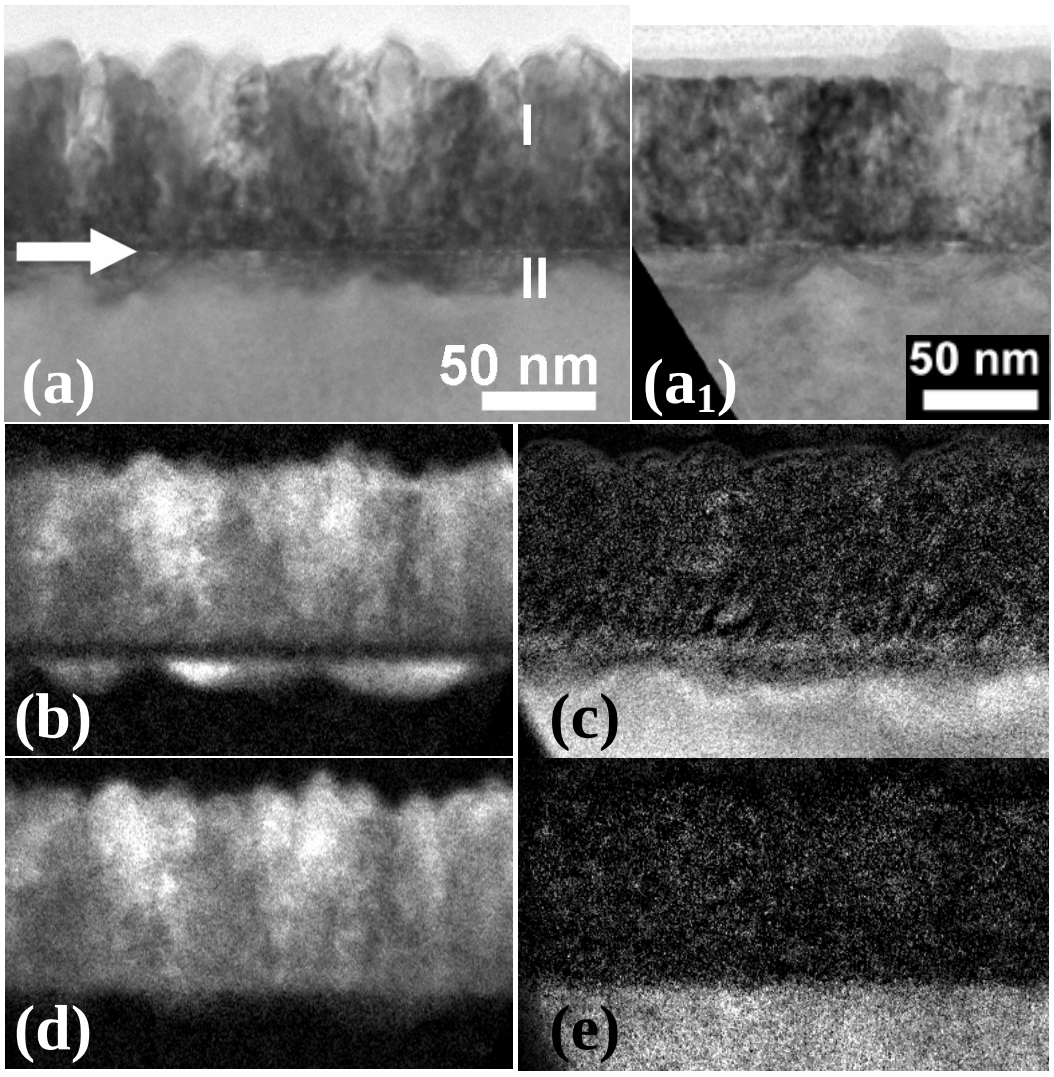

Fig. 8.3. a) Bright field, cross-sectional TEM image of Co_2MnSi on GaAs(001), oriented along the $[1\bar{1}0]$ zone axis, and energy filtered TEM mapping of b) Mn, c) Ga, d) Co, and e) As. a_1 is for another sample grown under identical conditions (films are coated with carbon for the TEM preparation).

These results suggest that region II consists predominantly of Mn and As (epitaxial interface layer observed by XRD, Fig. 8.1b), and that the thin, sharp layer between regions I and II is Co-Ga rich. These results illustrate that it is Mn diffusing into the GaAs and reacting with the As, rather than As out diffusion that is the dominant mechanism of the formation of this Mn-As region. As can be clearly seen in Fig. 8.3b), Mn shows a diffusion profile expected for a semiconductor being doped with an element. It is region II that gives rise to the epitaxial interface peaks observed by XRD (Fig. 8.1b) and c). These results are also supported by EDS spectra, but quantitative analysis of the composition of the interfacial reaction regions could not be obtained because of drift. Analysis of the composition of the middle part of the Heusler layer gave, Co: 50.2 ± 1.2 at. %, Mn: 23.8 ± 1.3 at. %, Si: 25.9 ± 1.3 at. %. This agrees well with EDS measurements carried out in the SEM, considering that the interaction volume penetrates the entire film and part of the substrate and so provides an average film composition. Analysis of the top part of the Heusler, showed that it was close to the stoichiometric ratio but slightly Si rich and for (a_1) it was slightly Co rich. Intermetallic compounds are prone to surface reconstruction.[4] The $L2_1$ structure of Co_2MnSi in the (001) direction consists of alternating Co and MnSi planes. A very recent theoretical study of Co_2MnSi shows that it is possible for the MnSi, pure Mn or pure Si terminated surfaces to be stabilised.[5] A pure Mn termination would preserve the half-metallicity of the system, while surface states appear for the other terminations.

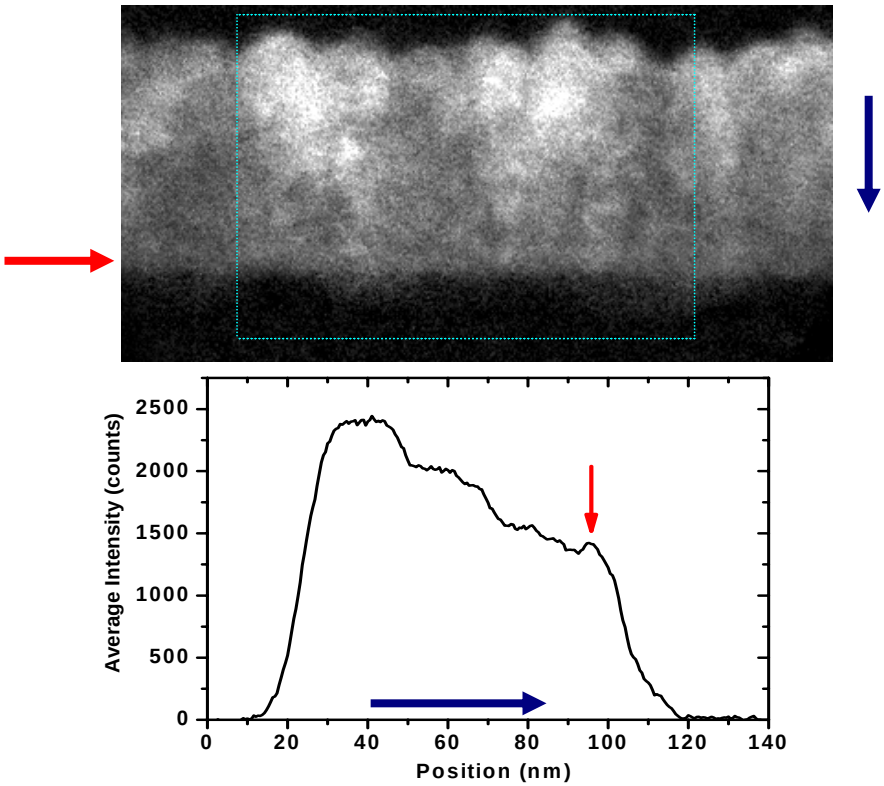

Fig. 8.4. Intensity of the Co signal as a function of depth into the Heusler layer.

Lattice images of the GaAs(001) substrate and the middle of the Co_2MnSi layer with their corresponding FFTs are shown in Fig. 8.5 (zone axis is [110]). They show very good crystallographic alignment and the FFTs overlap completely exhibiting the same symmetry. Unlike the FFT of the GaAs, the spot intensities for the Co_2MnSi are not equal and is attributed to good $L2_1$ ordering. This is supported by the simulation for the Co_2MnSi $L2_1$ structure (Fig. 8.5e).

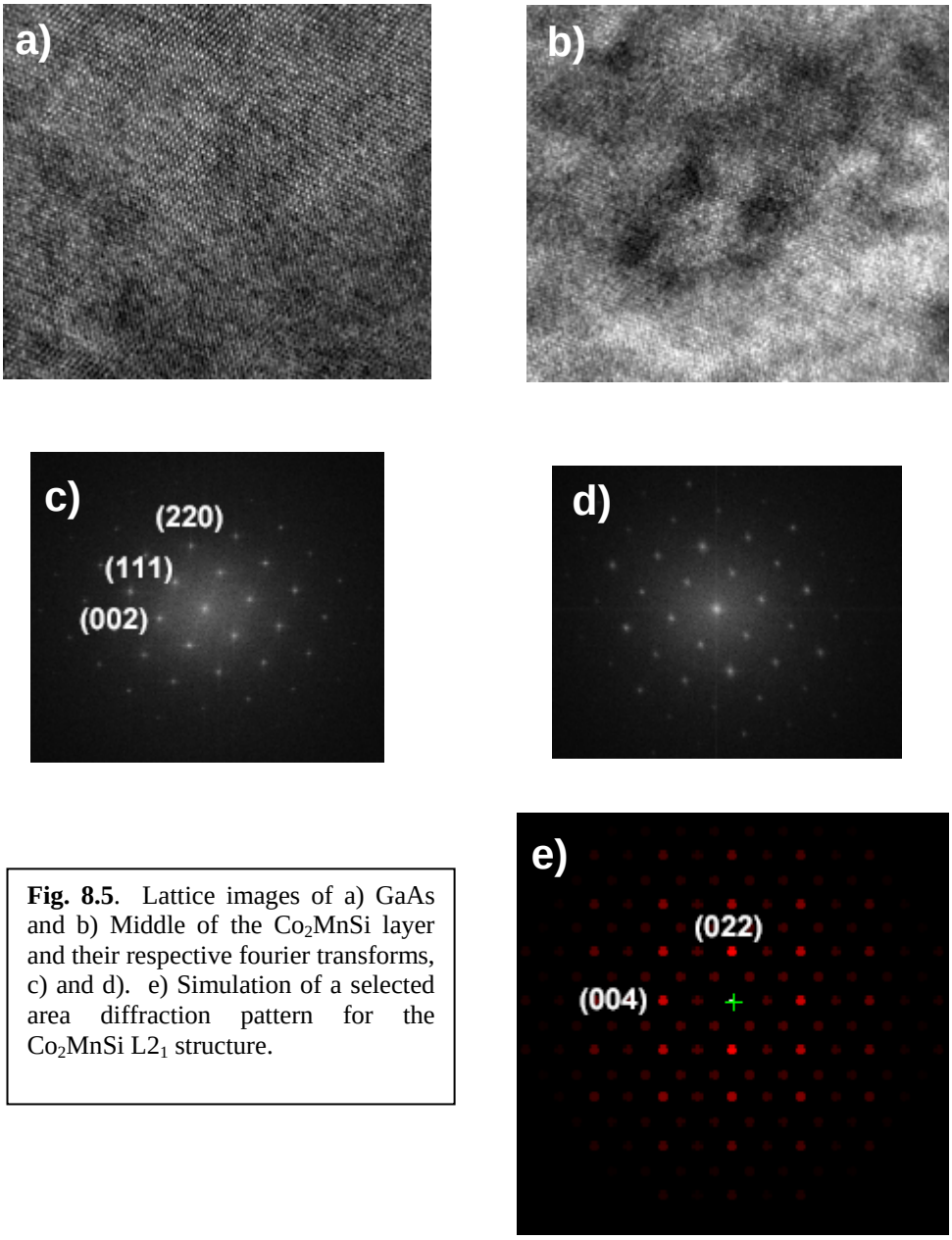

Fig. 8.5. Lattice images of a) GaAs and b) Middle of the Co_2MnSi layer and their respective fourier transforms, c) and d). e) Simulation of a selected area diffraction pattern for the Co_2MnSi $L2_1$ structure.

A more detailed study of the interface region (Fig. 8.6) reveals that close to the interface the Co_2MnSi still has a good crystallographic structure (Fig. 8.6a and c). However, in the interaction zone (Fig. 8.6 e), which corresponds to region II in Fig. 8.3(a_1), the lattice image shows bands,

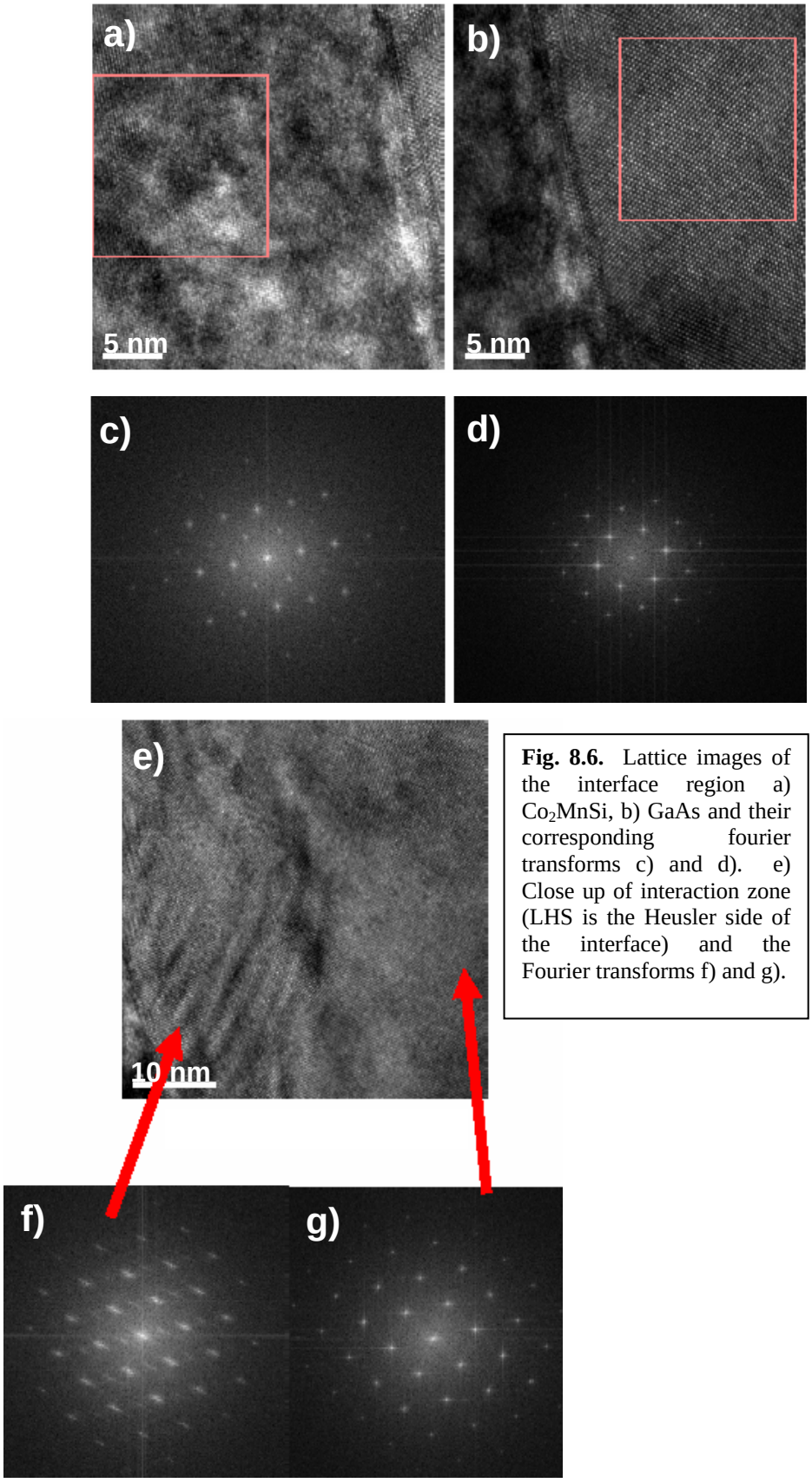

Fig. 8.6. Lattice images of the interface region a) Co_2MnSi, b) GaAs and their corresponding fourier transforms c) and d). e) Close up of interaction zone (LHS is the Heusler side of the interface) and the Fourier transforms f) and g).

which could result from compositional variation or stress. It is most likely due to compositional variation because EDS of this region did not show a fixed composition. Therefore, although we

know that this region is rich in Mn and As, it is not clear what compounds are present. Since TEM studies have not been carried out on films that contained Mn_2As as detected by XRD (Fig. 8.1c) it is not clear if this phase would be located in region II. The corresponding FFT (Fig. 8.6f) is distorted and although it has the same symmetry as the GaAs, the diffraction spots are not as well defined. Most importantly, there is streaking in the 002 direction, indicating that there are a range of compositions. From the most intense peak, the lattice parameter was found to be 5.3 Å in good agreement with the 5.312 Å obtained from XRD for the $(002)_i$ peak. The out-of-plane lattice parameters (determined from (002) spots) for the Heusler layer were in good agreement with the 5.638 Å found from the XRD measurement, and the in-plane parameter (determined from (022) spots) was always slightly larger.

From the images in Fig. 8.3 one can see that there are regions where the Mn-As reaction zone is not present (although the thin Co-Ga interlayer is continuous). Lattice images of these regions show very abrupt interfaces (Fig. 8.7), as good as films grown by MBE.[6] Elimination of the reaction zone by either lower growth temperatures or a barrier layer should result in very abrupt interfaces.

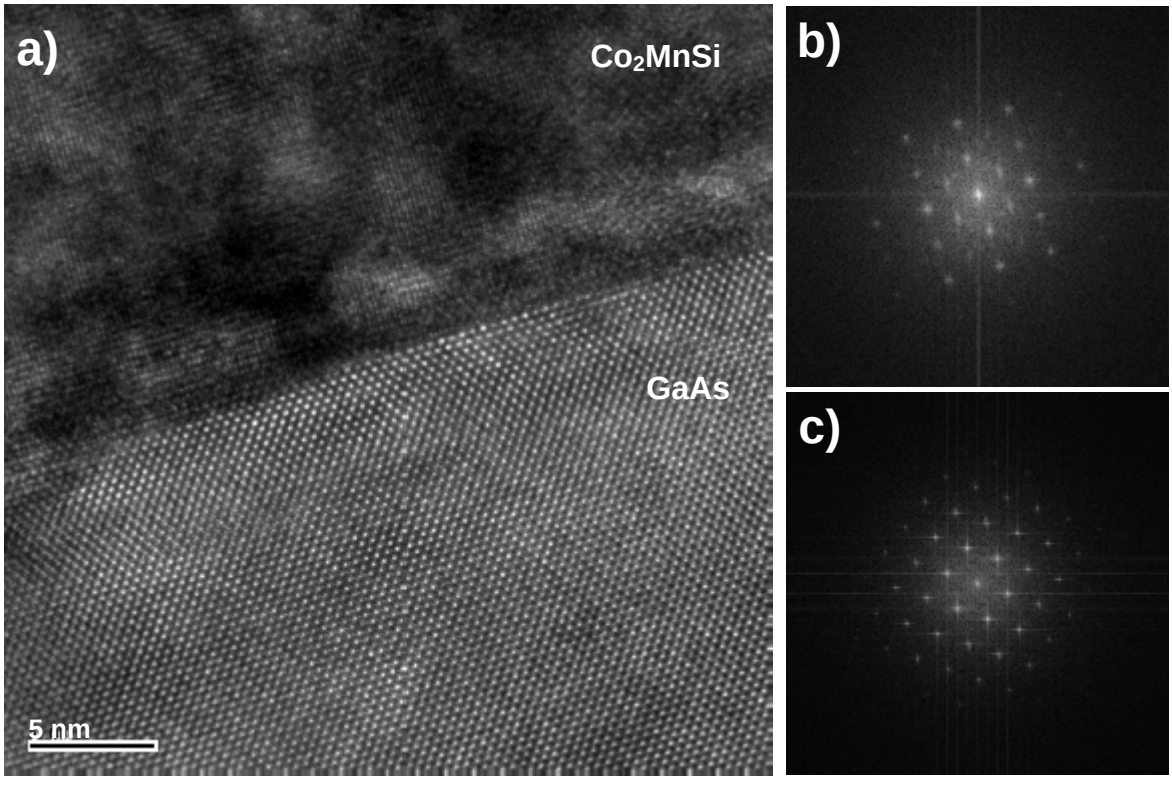

Fig. 8.7. a) HREM image of the abrupt interface, which occurs at positions where Mn has not diffused into the GaAs (the white periodic spots above the interface is the thin Co-Ga rich layer) and the corresponding FFTs of b) Co_2MnSi and c) GaAs(001).

8.4 Magnetic Characterisation

8.4.1 Determination of M_s

M_s was determined from in-plane hysteresis loops measured in a VSM at 10 K; for 300 nm, stoichiometric films M_s varied between 778 and 928 emu/cc (3.82-4.56 μ_B/formula unit). This is a reduced M_s compared to the bulk value of 1000 emu/cc (5.1 μ_B/formula unit), whereas films deposited on a-plane sapphire showed the bulk value (section 7.4.1). Such a reduced M_s has been observed in films of NiMnSb/GaAs(001).[2] The principal mechanism by which M_s is reduced is the formation of the epitaxial, Mn-As reaction zone and the thin Co-Ga rich interface layer. However, as shown in Fig. 8.8, M_s does not decrease monotonically with decreasing film thickness, suggesting either that the amount of the interface phase is not fixed (the extent of the reaction will also depend on the growth time[7]) and/or there are other mechanisms involved, as have been

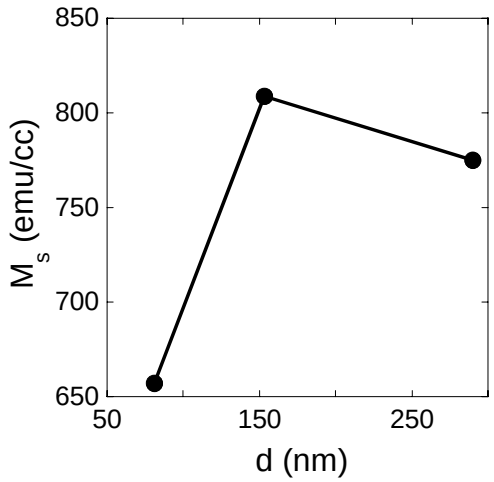

Fig. 8.8. Variation of M_s with film thickness for films grown at T_{sub} of 647 K.

reported in the literature: e.g. lattice strain induced by compressive stresses at the interface[8,9] and the effects of film and substrate morphology.[10] We observed a 3 % decrease in M_s upon increasing the temperature from 10 K to 300 K (Fig. 8.9), similar to our results for these films on sapphire. The T_c of films on GaAs could not be obtained because As starts to out-diffuse around 650 K and so this would change the properties of the Heusler layer, so T_c would be inaccurate.

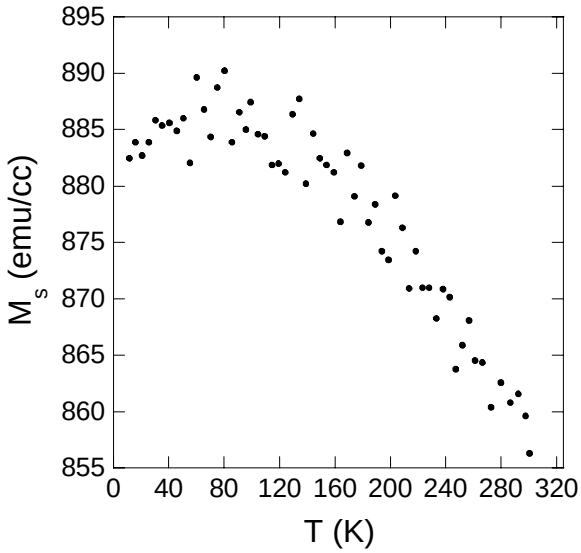

Fig. 8.9. M_s vs T for a 292 nm, stoichiometric film grown at a T_{sub} of 689 K.

8.4.2 Dependence of H_c on T_{sub}

H_c decreases with increasing T_{sub} (Fig. 8.10), reaching the lowest value of 14 Oe at 689 K. This was also observed for films on sapphire (section 7.4.2), although slightly higher values of H_c are obtained for films of similar thickness grown at the same T_{sub}.

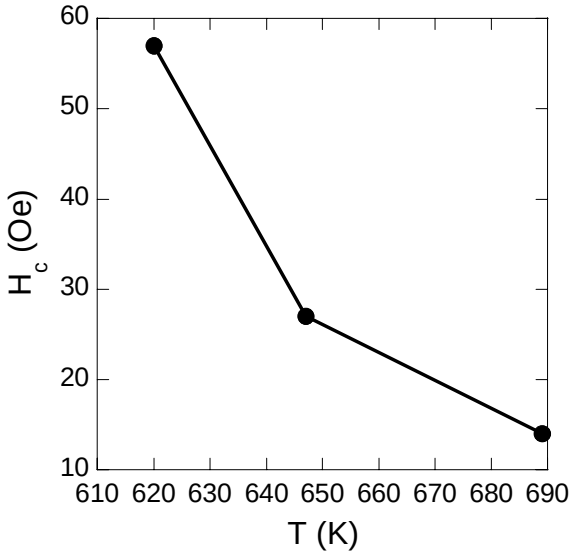

Fig. 8.10. Dependence of room temperature H_c on T_{sub} for a series of 300 nm, stoichiometric films.

8.4.3 Angular dependence of H_c

Fig. 8.11 shows the angular dependence of H_c for two, stoichiometric films. This was carried out in a VSM at room temperature, in which a hysteresis loop was taken at 10° intervals, from which H_c was extracted. Co_2MnSi is cubic and so a $Co_2MnSi(001)$ film should exhibit fourfold magnetic anisotropy. However, as can be seen from Fig. 8.11, the two <110> directions are inequivalent. This deviation from the fourfold symmetry has been observed by Ambrose *et al.*[11] in thin films of the full Heusler alloy Co_2MnGe, Van Roy *et al.*[12] in films of the half Heusler alloy NiMnSb and Krebs *et al.*[13] in films of Fe on GaAs(001). The latter author attributed this to the anisotropic nature of the tetrahedral Ga(As)-Fe bonds at the interface. GaAs exhibits tetrahedral bonding and for an unreconstructed surface, each surface atom has two unsatisfied tetrahedral bonds. Depending on the type of GaAs reconstructed surface, bonds are oriented along either [110] or $[1\bar{1}0]$. Therefore the inequivalence of the two <110> directions could be attributed to the asymmetry in the direction of the bonds at the interface.

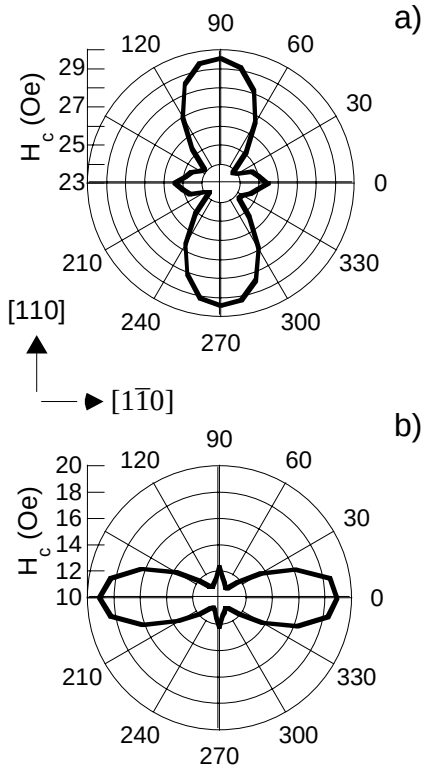

Fig. 8.11. Polar plots of room temperature H_c for two, stoichiometric films. The substrate is initially positioned between the coils so that the $[1\bar{1}0]$ direction is parallel to the direction of the applied field. a) Easy axis // [110], b) Easy axis // $[1\bar{1}0]$. Note that the $[1\bar{1}0]$ is designated by the manufacturer of the GaAs(001) wafer and in this case corresponds to the direction of the major flat.

For some of the films grown it was found that the easier of the two <110> directions is the [1$\bar{1}$0] direction, which is the case for the film in Fig. 8.11b). There is no obvious explanation for this, since all films were grown under similar conditions, and care was taken that the substrate was always mounted in the same orientation in both the growth chamber and the VSM. The corresponding hysteresis loops to the polar plot in Fig. 8.11b) are shown in Fig. 8.12. The easier of the two <110> directions has the squarer hysteresis loop (M_r/M_s = 0.98) and the largest H_c of 18.9 Oe. In the perpendicular orientation, M_r/M_s is 0.94 and H_c is 12.3 Oe. The hard axis was found to be at 60° to the easy axis (M_r/M_s = 0.75) and H_c is 10.9 Oe.

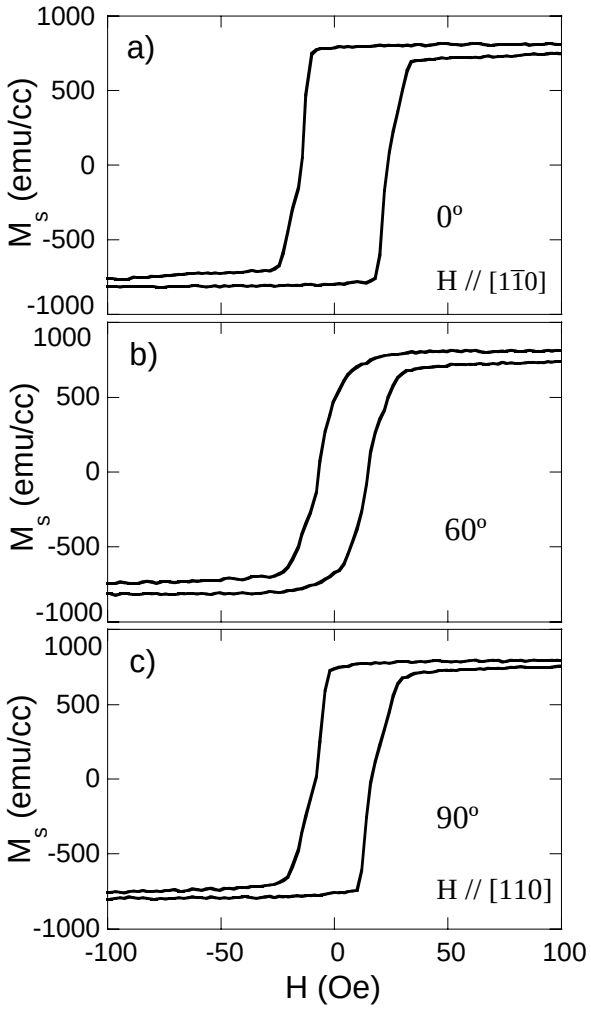

Fig. 8.12. Hysteresis loops measured at room temperature for the film shown in Fig. 8.11b), with the magnetic field applied in the plane of the film at a) 0° b) 60° c) 90° to [1$\bar{1}$0] . Angles correspond to the polar plot in Fig. 8.11b).

8.5 Transport measurements

8.5.1 Dependence of ρ on T_{sub}

Transport measurements were carried out from 4.2 to 295 K using a standard DC 4-point geometry. For a series of 300 nm, stoichiometric films, ρ decreased with increasing T_{sub} as shown in Fig. 8.13. The lowest $\rho_{4.2\ K}$ of 33 μΩcm was observed at 689 K, which is lower than that obtained on sapphire (47 μΩcm) at a higher T_{sub} of 715 K. The ρ vs T_{sub} data obtained for films grown on sapphire is shown for comparison (dotted line). At temperatures below 650 K, lower ρ films are obtained on sapphire.

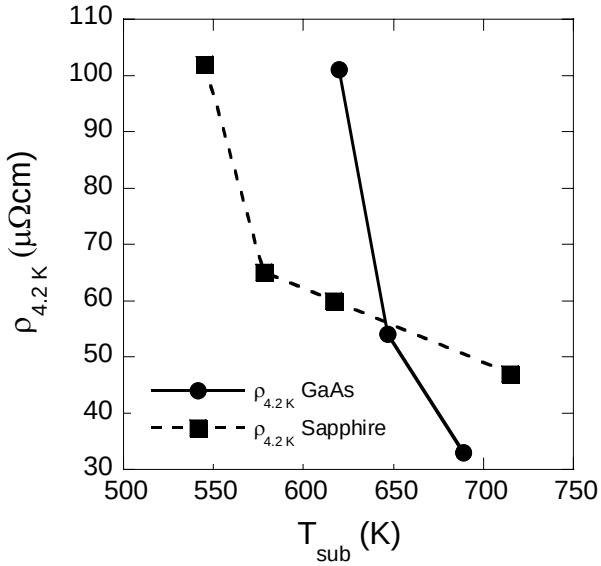

Fig. 8.13. $\rho_{4.2\ K}$ vs T_{sub} for 300 nm stoichiometric films on GaAs(001). The dotted line shows the data obtained on sapphire.

Fig. 8.14 shows that RR increases with increasing T_{sub}, reaching the maximum value of 1.46 at the highest growth temperature of 689 K. Once again these films show the same trend as films grown on sapphire (dotted line).

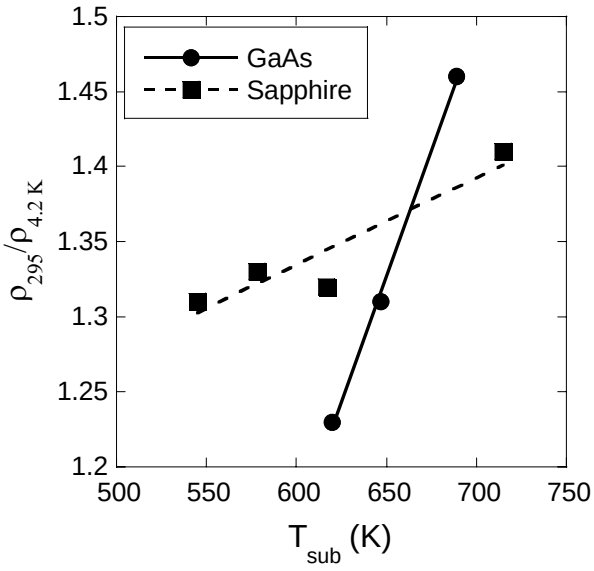

Fig. 8.14. $\rho_{295\ K}/\rho_{4.2\ K}$ vs. T_{sub} for 300 nm stoichiometric films on GaAs(001). The dotted line shows the data obtained on sapphire.

8.5.2 Surface Polarisation[2]

The spin polarisation of the transport current, P_t was measured by point contact Andreev reflection between Nb cut tips and the Heusler film at 4.2 K. In the limit Z=0, it was found that P_t~55 ± 5%, consistent with measurements on bulk single crystals of Co_2MnSi,[14, 15] and our earlier measurements on thin films of Co_2MnSi on sapphire (section 7.5.5). In the case of Co_2MnSi on sapphire, films grew with a strong (110) texture, whereas on GaAs(001) the films have a strong (001) texture. However, P_t is very similar in both cases, indicating that either P_t is independent of orientation or that the Heusler surface reconstructs in the same way.

8.6 Summary

Highly oriented (001) thin films of Co_2MnSi have been grown on GaAs (001) by dc magnetron co-sputtering, without a buffer layer. Interfacial reactions resulted in the formation of an epitaxial Mn-As region, and a thin interfacial layer that was Co-Ga rich. This prevented the lattice matching of the Co_2MnSi to the GaAs(001) hence hindering epitaxial growth of the Heusler. The reaction zone also meant that films exhibited a M_s slightly below the bulk value. In order to obtain epitaxial films with the bulk M_s either lower growth temperatures will be required (compromising the structural quality of the films) or a barrier layer such as Al_2O_3. The expected fourfold

[2] Carried out by Y. Miyoshi and Y. Bugoslavsky at the Blackett Laboratory, Imperial College

anisotropy was not obtained for this cubic material, which is most likely due to the anisotropy of the reconstructed GaAs surface. In spite of this anomalous behaviour, P_t was 55 %, which is in good agreement with the bulk, and films showed some improved structural, magnetic and transport properties to previous films grown on a-plane sapphire, indicating the potential of growing on this technologically important substrate.

References

[1] E. Kneedler, P. M. Thibado, B. T. Jonker, B. R. Bennett, B. V. Shanabrook, R. J. Wagner, and L. J. Whitman, J. Vac. Sci. Technol. B **14**, 3193 (1996).

[2] W. Van Roy, G. Borghs, and J. De Boeck, J. Cryst. Growth **227**, 862 (2001).

[3] Z. Yang, K. Zhang, S. Ke, and X. Xie, Phys. Rev. B **56**, 6727 (1997).

[4] D. Ristoiu, J. P. Nozieres, C. N. Borca, B. Borca, and P. A. Dowben, Appl. Phys. Lett. **76**, 2349 (2000).

[5] S. Hashemifar, P Kratzer, and M Scheffler, Phys. Rev. Lett. **94**, 096402 (2005).

[6] J. Lu, J. W. Dong, J. Q. Xie, S. McKernan, C. J. Palmstrom, and Y. Xin, Appl. Phys. Lett. **83**, 2393 (2003).

[7] J. L. Hilton, B. D. Schultz, S. McKernan, and C. J. Palmstrom, Appl. Phys. Lett. **84**, 3145 (2004).

[8] M. W. Ruckman, J. J. Joyce, and J. H. Weaver, Phys. Rev. B **33**, 7029 (1986).

[9] C. Vittoria, F. J. Rachford, J. J. Krebs, and G. A. Prinz, Phys. Rev. B **30**, 3903 (1984).

[10] Y. B. Xu, E. T. M. Kernohan, D. J. Freeland, A. Ercole, M. Tselepi, and J. A. C. Bland, Phys. Rev. B **58**, 890 (1998).

[11] T. Ambrose, J. J. Krebs, and G. A. Prinz, Appl. Phys. Lett. **76**, 3280 (2000).

[12] W. Van Roy, J. De Boeck, B. Brijs, and G. Borghs, Appl. Phys. Lett. **77**, 4190 (2000).

[13] J. J. Krebs, B. T. Jonker, and G. A. Prinz, J. Appl. Phys. **61**, 2596 (1987).

[14] S. F. Cheng, B. Nadgorny, K. Bussmann, E. E. Carpenter, B. N. Das, G. Trotter, M. P. Raphael, and V. G. Harris, IEEE Trans. Magn. **37**, 2176 (2001).

[15] L. Ritchie, G. Xiao, Y. Ji, T. Y. Chen, C. L. Chien, M. Zhang, J. L. Chen, Z. H. Liu, G. H. Wu, and X. X. Zhang, Phys. Rev. B **68**, 104430 (2003).

"One can never consent to creep when one feels an impulse to soar."
Helen Keller.

Chapter 9

Devices with Heusler alloy electrodes

In this chapter the growth of trilayer structures involving one layer of Co_2MnSi and the subsequent fabrication of these structures into pseudo spin valves and tunnel junctions will be discussed.

9.1 Introduction

Both TMR and GMR are very sensitive to the spin polarisation of the magnetic electrodes and so replacing one of the electrodes by a HMF should drastically increase the amplitude of the TMR- and GMR- effect of relevant devices. In the previous two chapters, *P* was determined by point contact Andreev reflection. As mentioned in section 2.4.2, *P* can also be obtained from MTJs but the MR depends not only on the electronic states in the Heusler alloy at the barrier/Heusler interface, but also on the tunnel barrier itself.[1] Hence the measured *P* of the Heusler alloy is not a purely intrinsic materials parameter. From the CPP-GMR one cannot directly extract *P*, one normally determines the spin asymmetry ratio and the spin diffusion length.[2]

Films of the Heusler alloy Co_2MnSi have previously been incorporated into tunnel junctions,[3] exhibiting a TMR of 86 % at 10 K. However, no MR has been observed in bulk single crystals of Co_2MnSi,[4,5] and to date no PSVs employing this Heusler alloy have been fabricated. PSVs utilizing the Heusler alloy $Co_2Cr_{1-x}Fe_xAl$ as the bottom electrode showed a maximum GMR of 4 % at 15 K in the current in plane (CIP) geometry.[6] PSVs with the half Heusler NiMnSb exhibited a current perpendicular to plane (CPP) GMR of 9 % at 4.2 K.[7] However other structures using half metals have shown less promising $R(\boldsymbol{H})$ characteristics with MR values around 1 % at 60 K for CIP NiMnSb spin valves[8] and <0.05 % at 300 K for CIP and CPP spin valve structures based on Fe_3O_4.[9, 10]

9.2 Magnetic tunnel junctions

9.2.1 Fabrication

The trilayer structures were fabricated in-situ by dc magnetron sputtering. The generic structure of the tunnel junctions was Co_2MnSi(80 nm)/AlO_x(1.3-2.5 nm)/Co(40 nm). The Heusler layer was deposited from three elemental targets onto GaAs(001) (10×5 mm^2) positioned directly below the targets on a Ta strip heater (geometry of set-up described in section 7.2). Before loading the Al target was cleaned with a wire brush, followed by 5 mins ultrasound in ~0.1 M aqueous NaOH solution to remove the oxide layer. The Ta heater was also cleaned in NaOH solution to remove any Al from the previous deposition, which would otherwise diffuse into the Heusler layer. The substrates were chemically cleaned prior to loading into the vacuum system, as described in section 8.2.

The base pressure of the growth chamber was 3×10^{-7} Pa. The substrates were annealed at 868 K for 10 min to remove the native oxide and to obtain the 4×2 surface reconstruction. The

temperature was then lowered to the growth temperature of 647 K and the system was pumped for 90 mins to ensure complete removal of As, since Mn_2As forms readily at the growth temperature. Co_2MnSi (80 nm) was grown in an argon pressure of 3.20 Pa and the deposition rate was 0.1 nm/s. The chamber was then cooled for 30 mins before depositing the Al layer to minimise the mobility of the Al and any interdiffusion. This chamber cooling was achieved by letting in a high pressure of Ar gas, which facilitated thermal contact with the nitrogen cooling jacket. Al (0.9-1.8 nm) was grown in an argon pressure of 0.51 Pa (deposition rate, 0.02 nm/s) and then oxidised in 1 kPa of pure oxygen for 1hr. The thickness of the Al layer requires careful calibration and this was achieved by profilometry of a lithographic step by AFM and then investigated by low angle reflectivity measurements. For later tunnel junctions the Al layer was plasma oxidised in pure oxygen at 10 Pa for 120-240 s (RF forward power 17 W). A loop (radius 22 mm) of high purity Al wire (3 mm thick) was used to form the glow discharge (see photo Fig. 3.5b) and this was situated near to the Al target. Pure Al wire was used to prevent contamination of the tunnel barrier by sputtered atoms during the oxidation process. After pumping out the oxygen, the Co electrode was deposited (40 nm), in an argon pressure of 3.07 Pa (deposition rate, 0.03 nm/s).

Patterning* was carried out using optical lithography followed by conventional Ar ion milling to form a series of 15 mesas ranging in size from 5×5 μm^2 to 19×19 μm^2, followed by the lift-off of a silica insulation layer and finally a top Cu wiring connection, to form a cross geometry.

9.2.2 Structural characterisation of the trilayers

In order to achieve a high TMR, the barrier layer needs to be as thin as possible whilst remaining continuous and free of pinholes. The thickness of the barrier layer increases by about 50 % upon oxidation[11] and so an Al layer in the range of 1-2 nm was investigated, aiming for a barrier thickness that did not exceed 3 nm. The deposition rate of the Al was calibrated using the AFM with an accuracy of ±1 %. X-ray reflectivity measurements should provide a more accurate method of determining the thickness of the Al layer. Unfortunately, the X-ray scattering cross-section of Al is very small and so it is difficult to characterise a pure Al film. X-ray reflectivity measurements of unpatterned multilayers has been found to be inconsistent with other methods of determining barrier thickness,[12] and TEM analysis appears to be the most direct, quantitative method.[11] Therefore, reflectivity measurements carried out on the trilayer structures (Fig. 9.1) were just used as a means to check the quality of the interfaces. Fig. 9.1b) shows more fringes compared to 9.1a) suggesting that the thinner barrier layer of 1.3 nm instead of 2.1 nm (assuming a thickness increase of 50 % after oxidation) results in smoother interfaces. The fringes observed and labelled in 9.2b) correspond to the 80 nm Co_2MnSi layer. The fringes corresponding to the 40

* Carried out by Dr J. L. Prieto, Device materials group, University of Cambridge

nm Co layer would be masked by these. The peaks labelled in 9.1a) correspond to a 4 nm layer of cobalt oxide because the trilayers were not capped. No peaks from the barrier layer can be seen but peaks corresponding to this layer would be separated by ~2.1° for the 2.1 nm barrier in Fig. 9.1a) and by ~3.4° for the 1.3 nm barrier in Fig. 9.1b). As one can see from both low angle scans, the intensity has dropped off considerably by $2\theta = 2.5°$ and so it would be difficult to distinguish these peaks (although the scan spans 5 log decades, indicating that the film is of reasonable quality). The cobalt oxide peak could also smear out the barrier peak.

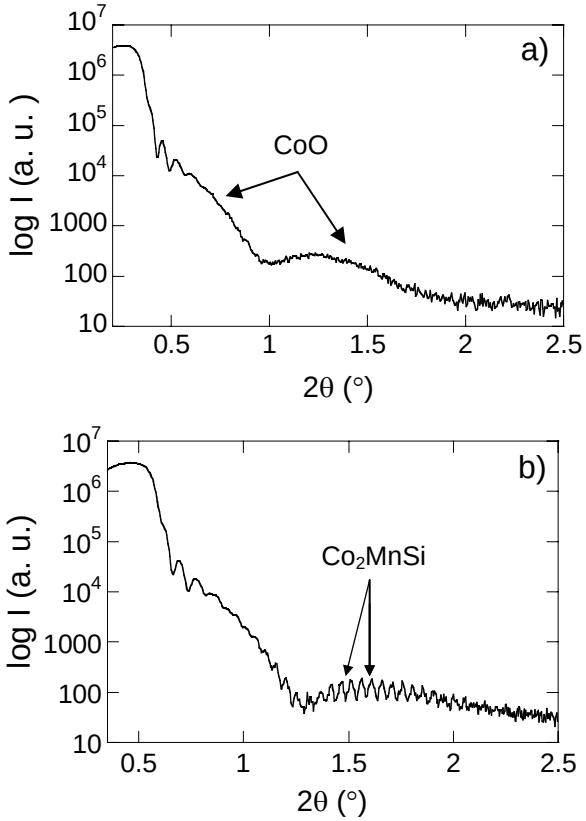

Fig. 9.1. Reflectivity measurements for a) Co_2MnSi (80 nm)/AlO_x (2.1 nm)/Co (40 nm) and b) Co_2MnSi (80 nm)/AlO_x (1.3 nm)/Co (40 nm). Thickness is given for the total barrier layer, assuming a thickness increase of 50 % after oxidation.

9.2.3 Magnetic characterisation of the trilayers

Hysteresis loops of unpatterned trilayer structures were taken to check that there is independent switching of the magnetisation of the two ferromagnetic layers. If the switching is not distinct this could be because the coercivities of the two ferromagnetic layers are too similar but this might not be the case at lower temperatures or once the structure is patterned. Also, due to interfacial roughness there could be magnetostatic coupling of the two layers or pinhole formation. Fig. 9.2 shows the hysteresis loops of a trilayer with a 2.1 nm barrier parallel to a) $[1\bar{1}0]$ and b) parallel to [110]. The loops are similar so there is no significant anisotropy and in both orientations one can

clearly see that there is independent switching of the magnetisation of the two ferromagnetic layers. Saturation is reached in a lower field in 9.2 b) so this is probably the easier of the two directions. In a magnetic field greater than 500 Oe the magnetisation of the Co and the Co_2MnSi layers are aligned parallel. On reversal of the magnetic field, the magnetisation of the Co_2MnSi layer switches first since it has the lower H_c of around 50 Oe, compared to 200 Oe for the Co layer and so the two layers are aligned antiparallel. At larger field the Co layer switches resulting in the

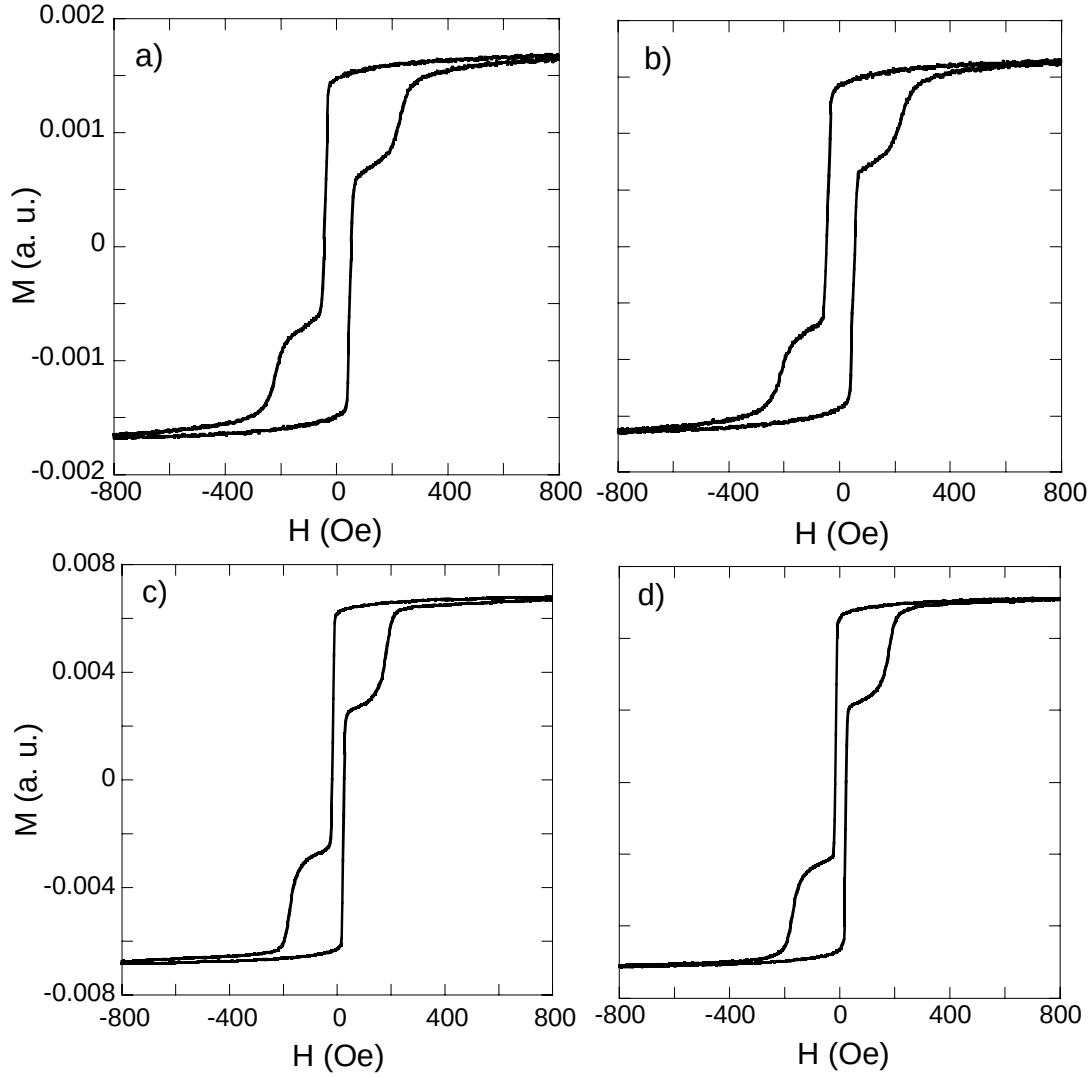

Fig. 9.2. Hysteresis loops of the unpatterned trilayers at RT for a) Co_2MnSi (80 nm)/AlO_x (2.1 nm)/Co (40 nm) // [1$\bar{1}$0] b) Co_2MnSi (80 nm)/AlO_x (2.1 nm)/Co (40 nm) // [110], c) Co_2MnSi (80 nm)/AlO_x (1.3 nm)/Co (40 nm) // [1$\bar{1}$0] d) Co_2MnSi (80 nm)/AlO_x (1.3 nm)/Co (40 nm) // [110].

parallel alignment. Growth of a thinner barrier (1.3 nm by plasma oxidation) still results in independent switching of the two layers (Fig. 9.2c and d).

9.2.4 Characterisation of MTJs

In spite of the promising magnetic data, the junction resistance of each of the devices was low and a similar value in each case (~60 Ω) irrespective of different barrier thickness and oxidation methods. Typical junction resistances in the literature tend to be >140 Ω in order to avoid geometrical enhancement of the TMR ratio.[13,14] This indicated that the problem arose during the processing of the trilayers and we tentatively attribute the low resistance to be due to resputtering onto the sidewalls of the junction.

9.3 Pseudo spin valves (PSVs)

9.3.1 Fabrication

The spin valve structures were fabricated in-situ by dc magnetron sputtering and the process is the same as outlined in section 9.2.1 up to the deposition of the Heusler layer. The substrates (10×5 mm^2 GaAs) were then cooled (below room temperature) before depositing the Cu layer to minimise interdiffusion. The Cu layer was deposited at 1.07 Pa (deposition rate, 0.09 nm/s) followed directly by the Co electrode at an argon pressure of 3.20 Pa (deposition rate, 0.03 nm/s). Each spin valve structure was capped with at least 4 nm Cu to prevent oxidation of the Co layer. Film thickness was determined using profilometry of a lithographic step by AFM. For the CIP devices the films were patterned to 20 μm×4 μm tracks (together with appropriate wiring and contact pads for electrical characterisation) with optical lithography followed by broad beam Ar ion milling (1 $mAcm^{-2}$, 500 V). The CPP devices were processed in two different ways: for the initial devices a FIB was used and for later devices conventional lithographic procedures were used. For the first CPP device,[†] the same method was used as for the CIP device, followed by processing with a Ga FIB to achieve vertical transport with a device area of 0.35 μm^2. This fabrication process with the Ga beam is described in detail elsewhere[15] and has been used previously in the fabrication of all metallic CPP spin valves.[16] This method of fabrication allowed the whole device heterostructure (including top Cu connection) to be deposited in-situ, giving high quality interfaces. For the second CPP device[‡], conventional Ar ion milling was used to form a 5×5 μm^2 mesa, followed by the lift-off of a silica insulation layer and finally a top Cu wiring connection, to form a cross geometry. The generic structure of the spin valves was therefore Co_2MnSi/Cu/Co/Cu. The thickness of the layers for the CIP film were 10/4/10/2 nm respectively, 300/10/16/300 nm for the FIB fabricated CPP structure and 80/5/40/4 nm for the conventionally

[†] Carried out by Dr C. Bell, Device materials group, University of Cambridge
[‡] Carried out by Dr J. L. Prieto, Device materials group, University of Cambridge

patterned mesa CPP device. For all cases, despite the changes in H_c of the Co_2MnSi layer with thickness, the Heusler layer is the free layer in the PSVs.

9.3.2 Structural characterisation of the trilayers

The XRD pattern of a Co_2MnSi(80 nm)/Cu(5 nm)/Co(40 nm)/Cu(4 nm) unpatterned spin valve structure is shown in Fig. 9.3. The stoichiometric Heusler layer is highly textured, following the [001] orientation of the lattice matched GaAs(001). The (002) and (004) peaks from the Heusler layer cannot be seen in this scan. Owing to the very low mismatch between the Heusler and the substrate these peaks are only visible as a shoulder to the right of the GaAs peaks (explained in section 8.3.1) and require high resolution XRD to be detected. The intense (002) and (004) peaks labelled with an 'i' originate from an epitaxial interfacial reaction zone between the substrate and the Co_2MnSi, as has been confirmed by high resolution TEM (see section 8.3.2). The broader peak (labelled with ′) is a combined peak of the Cu and the Co layers. The poor crystallinity of these layers is due to their low growth temperature in order to minimise interdiffusion. However the layers are still [001] oriented, indicating that they are influenced by the highly oriented Co_2MnSi underlayer.

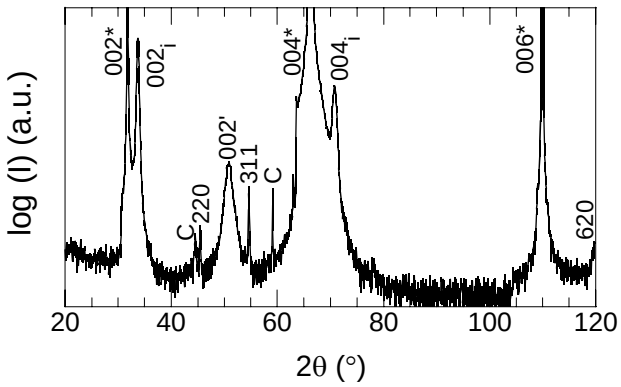

Fig. 9.3. XRD pattern of the unpatterned Co_2MnSi(80 nm)/Cu(5 nm)/Co(40 nm)/Cu(4 nm) spin valve structure. Diffraction peaks labelled with * denote substrate peaks, 'i' are interface peaks and ' indicates a combined Cu and Co peak and unlabelled peaks are the Co_2MnSi. The sharp lines indexed with a C, are W contamination lines from the X-ray tube.

9.3.3 Magnetic characterisation of the trilayers

As for the tunnel junction trilayers, hysteresis loops of unpatterned trilayer structures were taken to check that there is independent switching of the magnetisation of the two ferromagnetic layers. Hysteresis loops were taken in both the [1$\bar{1}$0] and the [110] directions as illustrated in Fig. 9.4 for the PSVs discussed in this chapter. It has been observed that single films of Co_2MnSi do not

exhibit the fourfold symmetry expected for a cubic material and the two <110> directions are inequivalent (section 8.4.3). We have generally found that the easy axis of magnetisation is in the $[1\bar{1}0]$ direction but occasionally, for unknown reasons the easy axis is in the [110] direction, which is the case in 9.4e). The hysteresis loop in Fig. 9.4e) is not as square as in Fig. 9.4f), so for this particular film, the long axis of the chip (// to $[1\bar{1}0]$) is actually a semi-easy axis. The tracks have to be patterned along the long axis of the chip, so the devices have not been fabricated in the optimum orientation. However, in both orientations one can clearly see that there is independent

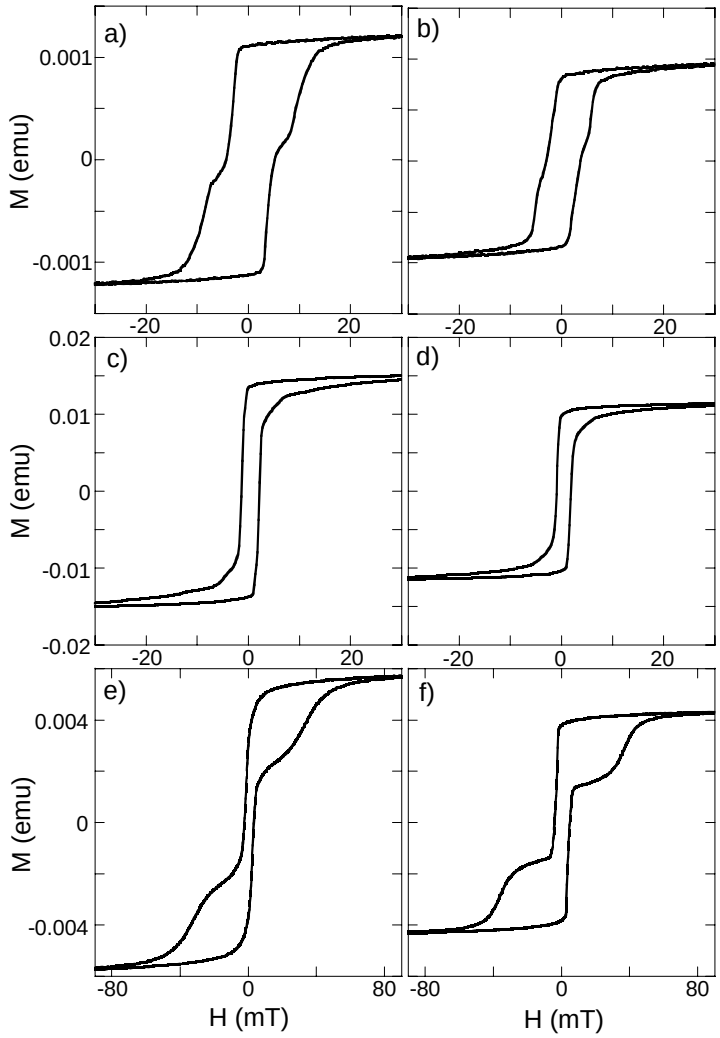

Fig. 9.4. Hysteresis loops of the unpatterned trilayers at RT in the $[1\bar{1}0]$ and [110] directions for a),b) Co_2MnSi(10 nm)/Cu(4 nm)/Co(10 nm)/Cu(2 nm), c),d) Co_2MnSi(300 nm)/Cu(10 nm)/Co(16 nm)/Cu(300 nm) and e),f) Co_2MnSi(80 nm)/Cu(5 nm)/Co(40 nm)/Cu(4 nm).

switching of the magnetization of the two ferromagnetic layers. In all cases M_s is larger for films measured in the $[1\bar{1}0]$ orientation because of the difference in the flux distribution passing through the pick-up coils when the long edge of the film is parallel and perpendicular to $\boldsymbol{H}$ (as discussed in 3.3.4). In a magnetic field greater than 60 mT the magnetisation of the Co and the Co_2MnSi layers

are aligned parallel. On reversal of the magnetic field, the magnetisation of the Co_2MnSi layer switches first since it has the lower $\mu_0 H_c$ of 2.8 mT, compared to 40 mT for the Co layer and so the two layers are aligned antiparallel. At larger field the Co layer switches resulting in the parallel alignment. The hysteresis loop of the trilayer in Fig. 9.4c does not show independent switching but after patterning the device does show a clear low-field MR response. Therefore, one should not necessarily view the absence of independent switching in the hysteresis loops as a direct indication that the device will not function.

9.3.4 Characterisation of the PSVs[§]

Prior to determining the *R* vs ***H*** behaviour of the devices, a single Co_2MnSi film was measured in order to determine if there is any AMR contribution from the Heusler layer, which would need to be taken into account in the measurements of the PSVs. Figure 9.5 shows the resistance of a single, 225 nm Co_2MnSi film as a function of applied magnetic field at 15 K. In both the longitudinal and transverse configurations the MR is very low (<0.03 %) in agreement with bulk single crystals,[4,5] but does not appear to arise from anisotropic magnetoresistance (AMR). In the

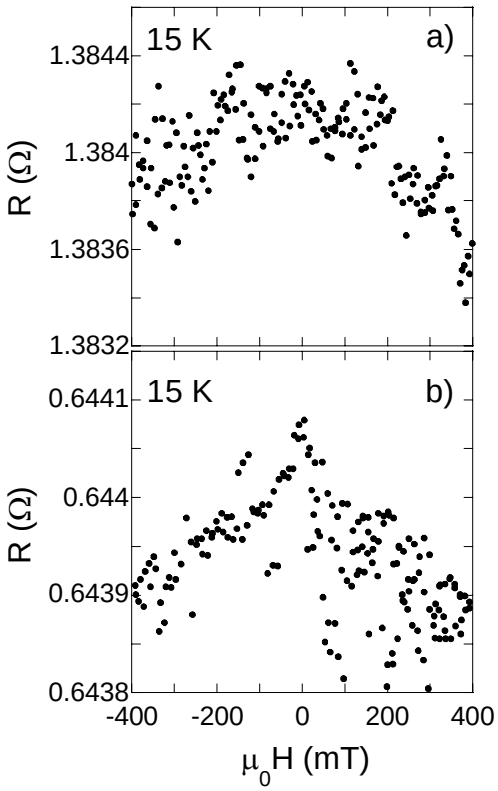

Fig. 9.5. Magnetoresistance of a 225 nm Co_2MnSi single film at 15 K in a) longitudinal configuration and b) transverse configuration.

[§] Carried out with Dr C. W. Leung, Device materials group, University of Cambridge.

case of AMR, one would expect a sign change in the *R* vs. ***H*** behaviour when the orientation of the current and applied field switches from the parallel to perpendicular configuration. The absence of a sign change in Fig. 9.5a) and b) indicates no AMR contribution. Similar results have been observed by Hordequin *et al*.[8] in thin films of NiMnSb (300 nm) but not in bulk crystals.

In contrast the CIP spin valve film shows clear peaks in the *R*(***H***) curve, associated with the GMR response of the spin valve (Fig. 9.6). As expected, the MR at 15 K (~0.45 %) was higher than at 77 K (~0.35 %), and the *R*(***H***) measurements with the field parallel and perpendicular to the current flow direction showed a negative MR. In the low field region (i.e. ± 100 mT) there is a difference in the MR behaviour in the longitudinal (Fig. 9.6a and b) and the transverse (Fig. 9.6c) configurations, probably due to the AMR of the Co layer. In addition, there was a 'background' MR of about 0.1 % that persisted even beyond the saturation field. This is similar to what was observed in Fig. 9.5, although the magnitude is larger here and the difference in the thickness of the Heusler films could account for this.

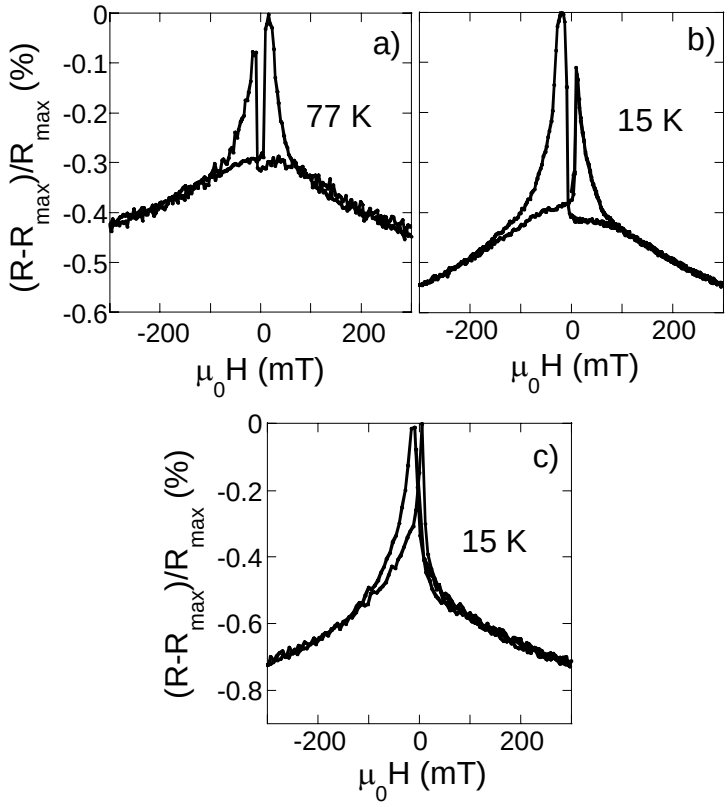

Fig. 9.6. CIP-MR for Co_2MnSi(10 nm)/Cu(4 nm)/Co(10 nm)/Cu(2 nm) on GaAs(001) spin valve structure. Longitudinal measurements carried out at a) 77 K, b) 15 K and transverse measurements carried out at c) 15 K. MR has been normalised to the largest MR at zero field.

For the CPP devices, $R(\boldsymbol{H})$ measurements were also made at 15 K for both the FIB processed device (Fig. 9.7) and the mesa structure (Fig. 9.8). The MR is ~ 0.15 % for the FIB device, and ~0.35 % for the conventionally patterned mesa CPP device, with an areal resistance change $A\Delta R$ (which is the product of device cross-sectional area and the measured MR change) of 2.4 and 5.6 × 10^{-15} Ωm^2, respectively. Since the $A\Delta R$ values are of similar magnitude compared with CPP GMR measurements with 3d transition ferromagnets,[17,18] the low MR must arise from the high base

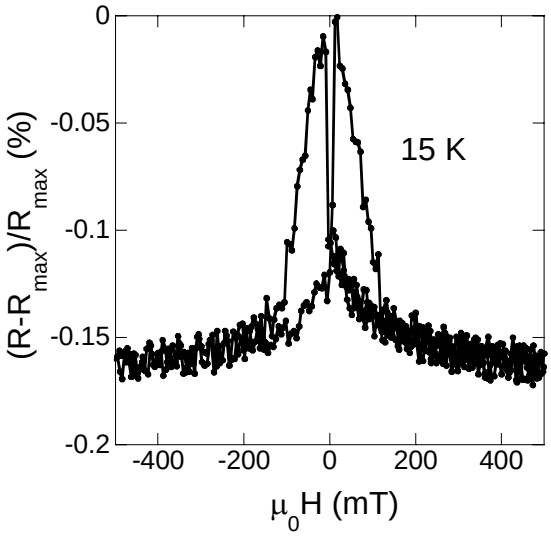

Fig. 9.7. CPP-MR at 15 K for Co_2MnSi(300 nm)/Cu(10 nm)/Co(16 nm)/Cu(300 nm) on GaAs(001) spin valve structure fabricated using the FIB.

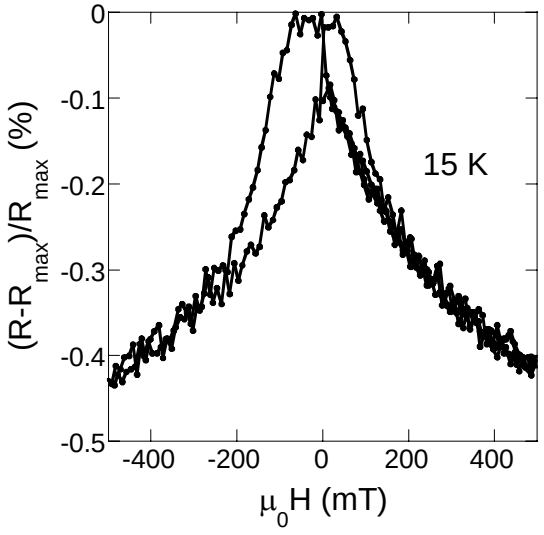

Fig. 9.8. CPP-MR at 15 K for Co_2MnSi(80 nm)/Cu(5 nm)/Co(40 nm)/Cu(4 nm) on GaAs (001) spin valve structure.

resistance in the devices. A rough calculation was made, using in-house resistivity values measured at 15 K (15, 1 and 40 $\times 10^{-8}$ Ωm for Co, Cu and Co_2MnSi, respectively). For the FIB device, a reasonable base resistance of ~ 2 Ω was obtained, with a large contribution from the Heusler electrode connecting to the device. On the other hand, the calculated base resistance of the lithography patterned device (~ 1.5 mΩ) was far too low to account for the small MR ratio obtained. The extra resistance could possibly come from the interfacial resistance during the patterning process. With suitable optimisation of the fabrication process, therefore, we would expect a much higher MR ratio than that obtained here.

We note that the sub-micron FIB device shows a much clearer saturation of the resistance at large field, whereas the CIP and mesa structure have a background that is comparable in magnitude with the GMR effect. This kind of background MR has been observed in some reports on GMR superlattices grown by various methods.[19,20] The basic argument for such observations is the formation of alloyed interfaces that are (super)paramagnetic, leading to an enhanced scattering of electrons. Alignment of the magnetisation in such regions by a large magnetic field can therefore suppress the scattering effect. This is entirely possible at both the GaAs/Co_2MnSi,[21] or at Co_2MnSi/Cu interfaces. The differences between Figs. 9.7 and 9.8 may originate from the different thickness of the Heusler layer used, current flow geometry, or a combination of these.

9.4 Summary

Magnetic tunnel junctions of Co_2MnSi(80 nm)/AlO_x(1.3-2.5 nm)/Co(40 nm) were prepared by dc magnetron sputtering and patterned using standard optical lithographic techniques. Although, hysteresis loops of unpatterned trilayers showed independent switching of the magnetisation of the two ferromagnetic layers, the MTJs showed no TMR. The junction resistance of each of the devices was low and this was attributed to problems during processing, mainly resputtering onto the sidewalls of the junction.

PSVs of Co_2MnSi/Cu/Co were grown and fabricated in both the CIP and CPP configurations. Clear low-field spin-valve contributions were observed at 15 K for the CIP PSV, conventionally patterned mesa CPP device and FIB device. The MR values are much lower than that expected from a PSV with a predicted 100 % spin polarised electrode. Further optimisation of the growth and interfacial conditions, layer thickness and fabrication process should increase the measured MR.

References

[1] J. M. De Teresa, A. Barthelemy, A. Fert, J. P. Contour, R. Lyonnet, F. Montaigne, P. Seneor, and A. Vaures, Phys. Rev. Lett. **82**, 4288 (1999).

[2] T. Valet and A. Fert, Phys. Rev. B **48**, 7099 (1993).

[3] S. Kammerer, A. Thomas, A. Hutten, and G. Reiss, Appl. Phys. Lett. **85**, 79 (2004).

[4] L. Ritchie, G. Xiao, Y. Ji, T. Y. Chen, C. L. Chien, M. Zhang, J. L. Chen, Z. H. Liu, G. H. Wu, and X. X. Zhang, Phys. Rev. B **68**, 104430 (2003).

[5] T. Endo, H. Kubota, and T. Miyazaki, J. Magn. Soc. Japan **23**, 1129 (1999).

[6] R. Kelekar and B. M. Clemens, J. Appl. Phys. **96**, 540 (2004).

[7] J. A. Caballero, A. C. Reilly, Y. Hao, J. Bass, W. P. Pratt, F. Petroff, and J. R. Childress, J. Magn. Magn. Mater. **199**, 55 (1999).

[8] C. Hordequin, J. P. Nozieres, and J. Pierre, J. Magn. Magn. Mater. **183**, 225 (1998).

[9] H. Takahashi, S. Soeya, J. Hayakawa, K. Ito, A. Kida, C. Yamamoto, H. Asano, and M. Matsui, J. Appl. Phys. **93**, 8029 (2003).

[10] S. van Dijken, X. Fain, S. M. Watts, and J. M. D. Coey, Phys. Rev. B **70**, 052409 (2004).

[11] A. E. T. Kuiper, M. F. Gillies, V. Kottler, G. W. t Hooft, J. G. M. van Berkum, C. van der Marel, Y. Tamminga, and J. H. M. Snijders, J. Appl. Phys. **89**, 1965 (2001).

[12] J. D. R. Buchanan, T. P. A. Hase, B. K. Tanner, N. D. Hughes, and R. J. Hicken, Appl. Phys. Lett. **81**, 751 (2002).

[13] K. Inomata, S. Okamura, R. Goto, and N. Tezuka, Jpn. J. Appl. Phys. **42**, L419 (2003).

[14] A. Conca, S. Falk, G. Jakob, M. Jourdan, and H. Adrian, cond-mat/0407034 (2004).

[15] C. Bell, G. Burnell, D. J. Kang, R. H. Hadfield, M. J. Kappers, and M. G. Blamire, Nanotechnology **14**, 630 (2003).

[16] C. W. Leung, C. Bell, G. Burnell, and M. G. Blamire, Nanotechnology **15**, 786 (2004).

[17] J. Bass and W. P. Pratt, J. Magn. Magn. Mater. **200**, 274 (1999).

[18] R. D. Slater, J. A. Caballero, R. Loloee, and W. P. Pratt, J. Appl. Phys. **90**, 5242 (2001).

[19] D. Barlett, F. Tsui, D. Glick, L. Lauhon, T. Mandrekar, C. Uher, and R. Clarke, Phys. Rev. B **49**, 1521 (1994).

[20] I. Bakonyi, J. Toth, L. F. Kiss, E. Toth-Kadar, L. Peter, and A. Dinia, J. Magn. Magn. Mater. **269**, 156 (2004).

[21] L. J. Singh, Z. H. Barber, A. Kohn, A. K. Petford-Long, Y. Miyoshi, Y. Bugoslavsky, and L. F. Cohen, (submitted 2005).

"Learn from yesterday, live for today, hope for tomorrow. The important thing is to not stop questioning."
Albert Einstein.

Chapter 10

Conclusions and further work

10.1 Summary

This thesis reports the growth of intermetallic compounds by co-sputtering from single elemental targets. The preliminary work involved constructing a sputtering set-up to grow a binary alloy (Sm-Co) and investigating how to control the composition spread that was obtained. Having achieved this, a larger sputtering flange was built up to grow the ternary Heusler alloy, Co_2MnSi.

10.1.1 Sm-Co thin films

Thin films of Sm-Co were grown by co-sputtering from two elemental targets, enabling good control of the film composition and more flexibility compared to using an alloy target. Many films of different composition could be fabricated in one deposition by placing a large number of substrates on a tray located directly below the targets. The composition spread could be reduced by increasing the target-substrate distance. It was quickly determined that the maximum H_c in the composition range investigated (1-11 at. % Sm) occurred at a Sm content of 5.3 at. %. This is an off-stoichiometric compound, illustrating the importance of investigating a composition range. This study showed that there was a second maximum in the H_c at low Sm content that was not previously known about. There was a critical composition around 8 at. % in which the easy axis of magnetisation switched from being out of the film plane (<8 at. %) to in-plane (>8 at. %). This was supported by XRD measurements, which showed that the c-axis (easy axis of magnetisation) of the crystallites was oriented out of the film plane for compositions <8 at. % but in-plane for compositions >8 at. %. It was found that for a fixed composition, the easy axis could be changed from being out of plane to in-plane by not cooling with the liquid nitrogen jacket during film growth and that H_c could be increased by decreasing the film thickness.

10.1.2 Co_2MnSi thin films

Thin films of Co_2MnSi were grown from three elemental targets on a-plane sapphire substrates by dc magnetron co-sputtering. Stoichiometric films were single phase and highly (110) textured, without the use of a seed layer. They exhibited the bulk value of M_s and films grown at the highest T_{sub} (715 K) showed the lowest resistivity (47 μΩcm at 4.2 K) and the lowest H_c (18 Oe). P_t of a 400 nm film grown at this deposition temperature was 54 %, consistent with measurements on bulk single crystals.[1,2] Changes in T_{sub} and stoichiometry were found to affect crystallographic alignment, bulk magnetic properties and electrical transport behaviour of these films, but not P_t. M_s decreased with decreasing film thickness and the different transport behaviour of thinner films indicated a graded disorder, which is significant even at a thickness of 110 nm. By growing on GaAs (001), which has a similar lattice parameter to Co_2MnSi it was expected that this disordered

region would be confined to the first few atomic layers. However, this was not the case because for films grown at T_{sub} of 647 K, interfacial reactions resulted in the formation of an epitaxial Mn-As region, and a thin interfacial layer that was Co-Ga rich. This prevented the lattice matching of the Co_2MnSi to the GaAs(001) hence hindering epitaxial growth of the Heusler. The reaction zone also meant that films exhibited a M_s slightly below the bulk value. In order to obtain epitaxial films with the bulk M_s either lower growth temperatures will be required (compromising the structural quality of the films) or a barrier layer. The expected fourfold anisotropy was not obtained for this cubic material, which is most likely due to the anisotropy of the reconstructed GaAs surface. In spite of this anomalous behaviour, P_t was 55 %, similar to the result obtained on sapphire, indicating that either P_t is independent of orientation or that the Heusler surface reconstructs in the same way. Films showed some improved structural, magnetic and transport properties to films grown on a-plane sapphire, indicating the potential of growing on this technologically important substrate. With this in mind, devices involving Co_2MnSi as one of the ferromagnetic electrodes were investigated. MTJs were prepared by dc magnetron sputtering and patterned using standard optical lithographic techniques. Although, hysteresis loops of unpatterned trilayers showed independent switching of the magnetisation of the two ferromagnetic layers, the MTJs showed no TMR. The junction resistance of each of the devices was low and this was attributed to problems during processing, mainly resputtering onto the sidewalls of the junction. PSVs of Co_2MnSi/Cu/Co were grown and fabricated in both the CIP and CPP configurations. Clear low-field spin-valve contributions were observed at 15 K but the MR values are much lower than that expected from a PSV with a predicted 100 % spin polarised electrode. Further optimisation of the growth and interfacial conditions, layer thicknesses and fabrication process should increase the measured MR.

10.2 Further work

It is essential that the interfacial reactions between Co_2MnSi and GaAs are minimised. As mentioned above, the growth temperature could be reduced although the crystallographic quality would be sacrificed. It has been found that interfacial reactions between Co and GaAs(001) begin at ~598 K, resulting in the formation of a highly (001) oriented ternary phase, most probably Co_2GaAs.[3] Co was determined as the dominant diffusion species and it was found that the ternary phase co-exists with randomly oriented CoGa and CoAs in the temperature range 598-773 K, while at higher temperatures only the binary compounds prevail. A recent letter by Hilton *et al.*[4] shows that Mn diffuses at 573 K into GaAs forming an epitaxial two phase region of Mn_2As and MnGa. From these findings it should be aimed to keep the growth temperature below 573 K, although it is hoped that interfacial reactions will start at a higher temperature for an alloy.

Another possibility is to use a tunnel barrier such as AlO_x, which also has the added advantage of providing a high resistance layer between the Co_2MnSi and the semiconductor, overcoming the conductivity mismatch problem[5] and increasing the spin injection and detection efficiency.[6,7] It has also been found that there is an enhancement in the spin selectivity when a 5 nm barrier of AlO_x is used between Fe and GaAs(100).[8]

A very recent work predicted that the half-metallicity of Co_2MnSi can be retained by appropriate termination at the (001) surface.[9] By analysing the surface band structure it was found that pure Mn termination, due to its strong surface-subsurface coupling will preserve the half-metallicity. It would be interesting to test this experimentally by means of spin-polarised STM.

Finally, it would be interesting to work on spin-LED structures and we have already carried out some preliminary work on this in collaboration with Imperial College. A spin-LED is a light emitting diode which incorporates a magnetic material as the injecting contact. As a result, spin polarised carriers are electrically injected from the magnetic contact into the semiconductor part of the device. If these carriers retain their spin polarisation the emitted electroluminescence is circularly polarised. The selection rules that govern the radiative recombination in the semiconductor can then provide a direct link between the circular polarisation of the emitted light along the surface normal and the spin polarisation of the injected carriers. GaAs quantum well (QW)-based spin-LEDs have been successfully used to demonstrate high spin injection efficiencies at low temperatures: in general though, the efficiency is dramatically dropped at higher temperatures due to the reduction of the spin lifetimes in these structures. InAs/GaAs self-assembled dots have been shown to exhibit long spin lifetimes due to the suppression of spin-relaxation mechanisms and are expected to have a much better temperature behaviour when employed as the active layer in a spin-LED structure.

The quantum dot (QD)-based spin-LEDs grown (Fig. 10.1) consist of a SI GaAs substrate, followed by a p-GaAs buffer layer and a p-AlGaAs cladding layer. An undoped GaAs layer is deposited followed by the deposition of a couple of monolayers of InAs. The dots are formed according to the Stranski-Krastanov growth mode. Due to the lattice mismatch between GaAs and InAs, strain is induced that leads under the right conditions to the formation of 3D islands. The dots are capped by a GaAs layer and an n-type AlGaAs layer is then deposited to complete the n-i-p structure. The doping profile of the top n-AlGaAs layer is chosen so that the resulting Schottky contact has a narrow depletion width; this enables spin-polarised carriers from the magnetic contact, Co_2MnSi to tunnel through to the semiconductor under reverse bias of the Schottky contact.

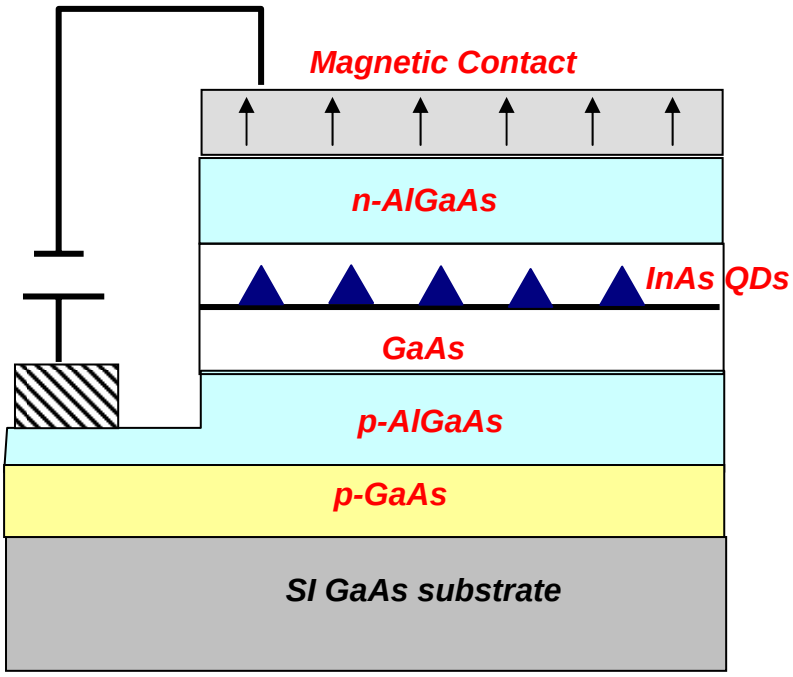

Fig. 10.1. Schematic of the structure of the QD-based spin-LED (courtesy of Dr G. Itskos, Blackett laboratory, Imperial College).

References

[1] S. F. Cheng, B. Nadgorny, K. Bussmann, E. E. Carpenter, B. N. Das, G. Trotter, M. P. Raphael, and V. G. Harris, IEEE Trans. Magn. **37**, 2176 (2001).

[2] L. Ritchie, G. Xiao, Y. Ji, T. Y. Chen, C. L. Chien, M. Zhang, J. L. Chen, Z. H. Liu, G. H. Wu, and X. X. Zhang, Phys. Rev. B **68**, 104430 (2003).

[3] M. Genut and M. Eizenberg, Appl. Phys. Lett. **50**, 1358 (1987).

[4] J. L. Hilton, B. D. Schultz, S. McKernan, and C. J. Palmstrøm, Appl. Phys. Lett. **84**, 3145 (2004).

[5] G. Schmidt, D. Ferrand, L. W. Molenkamp, A. T. Filip, and B. J. van Wees, Phys. Rev. B **62**, R4790 (2000).

[6] E. I. Rashba, Phys. Rev. B **62**, R16267 (2000).

[7] J. A. C. Bland, T. Taniyama, W. S. Cho, and S. J. Steinmueller, Curr. Appl. Phys. **3**, 429 (2003).

[8] T. Taniyama, G. Wastlbauer, A. Ionescu, M. Tselepi, and J. A. C. Bland, Phys. Rev. B **68**, 134430 (2003).

[9] S. Hashemifar, P Kratzer, and M Scheffler, Phys. Rev. Lett. **94**, 096402 (2005).